6-2-2017 12:00 AM

A Method for Hemispherical Ground Based Remote Sensing of Urban Surface Temperatures

Michael A. Allen
The University of Western Ontario

Supervisor
Dr. James A Voogt
The University of Western Ontario

Graduate Program in Geography
A thesis submitted in partial fulfillment of the requirements for the degree in Master of Science

Abstract

This thesis presents a method for deriving time-continuous urban surface temperature and heat island assessments from hemispherical ground-based measurements of upwelling thermal radiation. The method, developed to overcome geometric and temporal biases inherent in traditional thermal remote sensing of urban surface climates, uses a sensor view model in conjunction with a radiative transfer code to derive atmospherically corrected, hemispherical radiometric urban surface temperatures. These are used to derive two long-term climatologies of surface urban heat island (sUHI) magnitudes for Basel, Switzerland and Vancouver, Canada. sUHI development shows significant variation based on time-of-day, season, and ambient and synoptic conditions. Results also show large differences in remote sensed sUHI from hemispherical, nadir and complete representations of the urban surface, with a nadir view overestimating seasonal $sUHI_{max}$ from a complete view by nearly a factor of two. In contrast, a hemispherical view provides significantly more representative, time-continuous urban surface temperature and sUHI analysis.

Keywords: urban, climate, surface, temperature, thermal, remote sensing, micrometerology, urban heat island

Acknowledgments

Thank you to my research advisor, Dr. James Voogt for his constant encouragement and trust in me through this project, for putting up with my odd work schedules and round the clock emails, and for refocusing and reining me in at times. I am tremendously grateful for his support and for giving me the opportunity to talk about my graduate work all over the world. Thank you for a great two years.

Thank you to A. Christen who provided a good portion of the foundational work that made this thesis possible.

Thank you to C. Smart, who served on both my committee and examination board, for his excitement and insight about this work. Thanks are also due to the other members of my examination board, J. Wang and G. Osinski, for their prompt and thoughtful comments.

Thank you to my family for their love and support and for reminding me that my audience isn't always climatologists.

Thank you to my work study student M. Bourke, who spent quite a few weekends in the lab running data for me - without which, this thesis would not have been completed on time.

Thank you to my lab-mates D. Kuruklaarachchi, T. Wiechers, and R. Hilland, and quasi-lab-mates J. Howett, L. Middleton, C. Irwin, and N. Pearce for their wonderful Canadian hospitality and for at times keeping me sane. Thanks also to S. Cappuccitti, S. Pearce, K. West, V. Staples, J. Williams, R. Davis, B. Holmes, and T. Eckmann.

In truth, this space is too small to thank everyone I would like to. To those who contributed to this work in any capacity - directly or indirectly - thank you. You know who you are.

Statement on Co-authorship

The body of this thesis (Chapters 2 and 3) is made up of two academic papers with the following authorship:

1. An atmospheric correction method to derive hemispherical time-continuous urban surface temperature

    - Michael A. Allen: 60%, Developed the method, its parameterization, and evaluations for both. Contributions to method theorization. Produced text and figures (unless otherwise referenced).
    - James A. Voogt: 30%, Project conceptualization. Contributions to methodology and development. Edited text and figure design.
    - Andreas Christen 10%, Project conceptualization. Provided data.

2. A climatology of sUHI derived from hemispherical radiometric surface temperatures

    - Michael A. Allen: 70% Conducted exploratory data analysis and determined the analysis to present. Produced results, text, and figures (unless otherwise referenced).
    - James A. Voogt: 20% Contributions to interpretation of results. Edited text and figure design.
    - Andreas Christen 10% Contributions to interpretation of results and figure design. Provided data.

Chapters 1 and 4 were written by the candidate and edited by James A. Voogt.

Table of Contents

List of Tables

List of Figures

List of Symbols

Roman

Symbol	Unit	Property
C	$\mathrm{J\,m^{-3}\,s^{-1}}$	heat capacity
FOV	deg	sensor field of view
H	m	building height
H	$\mathrm{g\,m^{-3}}$	water vapor mass density
$\mathrm{K_{up}}$	$\mathrm{W\,m^{-2}}$	upwelling shortwave radiation
$\mathrm{K_{down}}$	$\mathrm{W\,m^{-2}}$	downwelling shortwave radiation
L_0	$\mathrm{W\,m^{-2}}$	irradiance at the surface
L_z	$\mathrm{W\,m^{-2}}$	irradiance at height z
$L^{\downarrow}_{sky}$	$\mathrm{W\,m^{-2}}$	upwelling longwave flux density emitted from the atmosphere
$L^{\uparrow}_{z}$	$\mathrm{W\,m^{-2}}$	upwelling longwave flux density at height z
$L^{at-sensor}_{atm}$	$\mathrm{W\,m^{-2}}$	the component of at-sensor irradiance from the atmosphere
$L^{at-sensor}_{surf}$	$\mathrm{W\,m^{-2}}$	the component of at-sensor irradiance from the surface
$L^{at-sensor}_{total}$	$\mathrm{W\,m^{-2}}$	total at-sensor irradiance
$\mathrm{L_{down}}$	$\mathrm{W\,m^{-2}}$	downwelling longwave flux density
$\mathrm{L_{up}}$	$\mathrm{W\,m^{-2}}$	upwelling longwave flux density
L'_z	$\mathrm{W\,m^{-2}\,sr^{-1}}$	directional radiance through path length z
P	hPa	atmospheric pressure

Symbol	Unit	Property
$Q*$	$\mathrm{W\,m^{-2}}$	net radiation flux density
ΔQ_A	$\mathrm{W\,m^{-2}}$	net advective heat flux density
ΔQ_G	$\mathrm{W\,m^{-2}}$	net heat storage flux density
Q_E	$\mathrm{W\,m^{-2}}$	latent heat flux density
Q_F	$\mathrm{W\,m^{-2}}$	anthropogenic heat flux density
Q_H	$\mathrm{W\,m^{-2}}$	sensible heat flux density
r	-	spectral sensor response
$\overline{r}$	-	Planck weighted mean broadband sensor response
R	$\mathrm{W\,m^{-2}\,sr^{-1}\,\mu m^{-1}}$	spectral directional radiance
$R_0^{\uparrow}$	$\mathrm{W\,m^{-2}\,sr^{-1}\,\mu m^{-1}}$	upwelling spectral directional radiance at height zero
$R_{atm}^{\uparrow}$	$\mathrm{W\,m^{-2}\,sr^{-1}\,\mu m^{-1}}$	upwelling spectral directional radiance emitted from the atmosphere
$R_{sky}^{\downarrow}$	$\mathrm{W\,m^{-2}\,sr^{-1}\,\mu m^{-1}}$	downwelling spectral directional radiance emitted from the sky/atmosphere
$R_z^{\uparrow}$	$\mathrm{W\,m^{-2}\,sr^{-1}\,\mu m^{-1}}$	upwelling spectral directional radiance at height z
t	min	time
T	K	temperature
$\mathrm{T_{adj}}$	K	dome adjusted $\mathrm{T_{hem,\,r}}$
$\mathrm{T_{air}}$	K	air temperature
$\mathrm{T_{bias}}$	K	bias in $\mathrm{T_{hem,\,r}}$ in terms of temperature
$\mathrm{T_{bright}}$	K	surface brightness temperature
$\mathrm{T_{calib}}$	K	instrument calibration temperature
$\mathrm{T_{comp}}$	K	complete urban surface temperature
$\mathrm{T_{emiss}}$	K	emission temperature
$\mathrm{T_{hem}}$	K	urban surface temperature viewed from a hemispherical remote sensor
$\mathrm{T_{hem,\,b}}$	K	urban surface brightness temperature viewed from a hemispherical remote sensor
$\mathrm{T_{hem,\,r}}$	K	urban surface radiometric temperature viewed from a hemispherical remote sensor

Symbol	Unit	Property
T_{plan}	K	urban surface temperature viewed from a sensor in the nadir
T_{rad}	K	radiometric surface temperature
T_{road}	K	road surface temperature
T_{roof}	K	roof surface temperature
T_{surf}	K	surface temperature
T_{wall}	K	wall surface temperature
aUHI	K	air temperature urban heat island magnitude
clUHI	K	canopy layer air temperature urban heat island magnitude
sUHI	K	surface temperature urban heat island magnitude
$sUHI_{comp}$	K	surface urban heat island magnitude calculated from T_{comp}
$sUHI_{hem}$	K	surface urban heat island magnitude calculated from $T_{hem,\,r}$
$sUHI_{plan}$	K	surface urban heat island magnitude calculated from T_{plan}
V_B	-	effects from background climate on observation of a given meteorological variable
V_H	-	effects from the urban environment on observation of a given meteorological variable
V_L	-	effects from local topography on observation of a given meteorological variable
V_M	-	observed meteorological variable
$V_{M,U}$	-	observed meteorological variable (urban)
V_{MR}	-	observed meteorological variable (rural)
W	m	building width
WD	deg	wind direction
WV	$\mathrm{m\,s^{-1}}$	wind velocity
z	m	height or path length
z_H	m	mean building height
z_t	m	layer thickness

Greek

Symbol	Unit	Property
α	-	albedo
ϵ	-	emissivity
ϵ_λ	-	spectral emissivity
θ	deg	zenith angle
λ	$\mu\mathrm{m}$	wavelength
λ_B	-	plan area of buildings
λ_C	-	complete aspect ratio
λ_I	-	plan area of impervious ground
λ_P	-	plan aspect ratio
λ_T	-	plan area of trees
λ_V	-	plan area of ground vegetation
ν	cm^{-1}	wavenumber
σ	$\mathrm{Wm}^{-2}\mathrm{K}^{-4}$	Stefan Boltzmann constant
σ_H	m	standard deviation of building height
τ	-	atmospheric transmittance
τ_d	-	atmospheric transmittance
τ_λ	-	spectral atmospheric transmittance
τ_Φ	-	hemispherical atmospheric transmittance
ϕ	deg	azimuth angle
Φ	-	view factor

Chapter 1

Introduction

Urban development drastically changes the character of the surface. Replacement of natural terrain with roads, buildings, parks, and other urban features modifies the geometry of the surface as well as its thermal, radiative, moisture, and aerodynamic properties. These modifications, combined with anthropogenic emissions of heat, result in a distinct urban climate; one which is often warmer, a phenomenon termed the urban heat island effect (UHI). As both the Earth's population and the urbanized fraction of that population increase (United Nations, 2014), cities grow and more people are exposed to urban-modified atmospheres. Thus, understanding how cities interact with the climate across spatiotemporal scales has important implications for human health, energy efficiency, and for informing future urban development. This, in part, has prompted significant expansion in study of the urban effect on climates, with particular focus on characterization of the urban effect on surface (T_{surf}) and air (T_{air}) temperatures.

The temperature of a surface (urban or otherwise) at its interface with the atmosphere is defined as the net result of the surface energy balance (Oke et al., 2017), wherein change in temperature at time t for a surface with thickness z_t and heat capacity C can be solved as,

$$C \frac{\partial \mathrm{T}_{\mathrm{surf}}}{\partial t} z_t = Q^* + Q_F - Q_H - Q_E - \Delta Q_A - \Delta Q_G \tag{1.1}$$

where Q^* is net radiation at the surface, Q_F, Q_H, and Q_E are fluxes of anthropogenic, sensible, and latent heat respectively, ΔQ_A is net advection of surface heat to or from the volume of air above the surface, and ΔQ_G is net storage of heat by the substrate below. A change in $\mathrm{T}_{\mathrm{surf}}$ is translated to change in $\mathrm{T}_{\mathrm{air}}$ as the surface exchanges energy with the atmosphere above it, primarily via convection and radiation. As such, $\mathrm{T}_{\mathrm{surf}}$ and $\mathrm{T}_{\mathrm{air}}$ are inextricably linked, particularly near to the ground, and a city's altered surface characteristics and energy balance manifest in modifications to both surface and air temperature regimes.

The notion that urban modifications to the environment produce elevated $\mathrm{T}_{\mathrm{air}}$ and $\mathrm{T}_{\mathrm{surf}}$ is not new, with the first formal studies of the urban effect on $\mathrm{T}_{\mathrm{air}}$ dating back to Howard (1833)'s identification of "artificial warming" and "urban contamination" in his characterization of spatial patterns of $\mathrm{T}_{\mathrm{air}}$ in early 19$^{\mathrm{th}}$ century London, England. Conceptually, contemporary studies of urban climate do not stray far from Howard (1833), by seeking to isolate and quantify the urban signal in measured or modeled assessment of a given meteorological variable. However, as Howard (1833) identified nearly two centuries ago, the sheer number of factors influencing direct measurement of climates makes experimental control nearly impossible in observational study. In any given observation of climate, myriad urban and non urban signals make it difficult to reliably differentiate urban influenced measures from those free of urban influence, confounding interstudy comparison. Development of physically based numerical models to represent physical processes affected by urbanization and which permit experimental

control have shown promise (Krayenhoff et al., 2014; Gastellu-Etchegorry et al., 1996; Masson, 2000; Martilli et al., 2002) yet the inherent complexity in simulating flows of energy, momentum, and mass at the scales necessary to represent the full range of physical processes over realistic environments remains an on-going challenge. Thus, accurate assessment of how a city affects the climate is a deceptively challenging task. To address this, Lowry (1977) presents a framework to isolate the urban effect in observation of a given meteorological variable. In his framework - termed the "Lowry method" - measurement of a meteorological variable (V_M) is the sum of forcings from the background climate and synoptic conditions (V_B), local topography (V_L), and the urban landscape (V_H)

$$V_M = V_B + V_L + V_H \tag{1.2}$$

Thus, isolation of the urban effect on observed V_M simply requires the removal of V_B and V_L. This can be achieved by subtracting some urban affected observation ($V_{M,\,U}$) from a non-urban observation ($V_{M,\,R}$) where $V_{H,\,R}$ = 0,

$$V_{M,U} - V_{M,R} = (V_B + V_L + V_H) - (V_B + V_L) = V_H \tag{1.3}$$

simplified as,

$$V_H = V_{M,\,U} - V_{M,\,R} \tag{1.4}$$

Study of the UHI with respect to T_{surf} (sUHI) and T_{air} (aUHI) - typically referring to T_{air} measured from approximately 2 m above ground level, yielding a "canopy layer" UHI (clUHI) - tacitly falls into such a framework, by replacing $V_{M,\,U} - V_{M,\,R}$ with $\Delta T_{U\,-\,R}$. However, in spite of its conceptual simplicity through the lens of the Lowry method, meta-analysis of

observational aUHI studies suggests that that simplicity may not translate well to real world analysis. In a points based assessment of 190 aUHI studies published between 1950 and 2007, Stewart (2011) found that nearly 50% of studies are ”scientifically indefensible”. In the analysis, each study was given a ”passing” or ”failing” grade and ranked based on methodological quality in the following criteria: conceptual model, operational definitions, instrument specification, site metadata, site representativeness, number of replicates, weather control, surface control, and synchronisity. Of the 190 surveyed studies, only 13% were derived from field sites that were sufficiently representative of the local-scale environment or lacked the meta-data to make such a determination. 89% lacked meta-data altogether. These findings suggest a significant gap between conceptual simplicity and practical realities in UHI analysis.

Conceptual problems in the aUHI literature are particularly discouraging as they are not the result of an evolution in measurement techniques or improved instrumentation. Techniques to observe and analyze aUHI did not see significant evolution or improvement in the period between 1950 and 2007 - in fact, Stewart (2011) suggests the opposite: a disproportionately large number of studies deemed scientifically sound were published early in the study purview. In the five years since its publication, aUHI study has seen further expansion and, as such, it is difficult to assess whether its critical analysis has prompted a shift towards more thoughtful, careful, and methodical study of aUHI, notwithstanding its relevance in study of the urban effect on other meteorological variables. Thus, in study of the urban effect on variables for which significant methodological shifts have or will occur, the warnings implicit in Stewart (2011) are particularly salient, as difficulties found in translating ”Lowry”-esque conceptual models to real world observations may be compounded by significant changes in methodology. What is clear in light of these findings, however, is that assessment of the urban effect on climate is *fundamentally difficult* in spite of its conceptual simplicity.

In contrast to urban T_{air} and aUHI assessment, where measurement techniques have not

undergone significant recent evolution and methodological problems arise in large part from conceptual shortcomings and simple carelessness, study of the urban effect on land T_{surf} is relatively new and significantly more complex. As such, methodological problems in sUHI study can arise from both conceptual flaws *and* instrument biases. In spite of these difficulties, the introduction of new methods, instruments, and analytical techniques in remote sensing of upwelling thermal infrared (TIR) radiation has lead to a rapid proliferation of study of urban T_{surf} and the sUHI - much of which is focused on remote sensing of TIR radiation. In the decades preceding this thesis, a combination of factors has lead to an increased focus on remote sensed study of urban T_{surf}:

- The proliferation of satellite and aerial TIR radiation remote sensors and ”openness” in data access policies.
- Improvements in sensor spatial, spectral, and radiometric resolutions.
- An increased focus on the importance of the surface in both determining and understanding key near-ground micro-meteorological phenomena.
- Interest in urban T_{surf} for human thermal comfort, energy conservation, and sUHI mitigation applications.

Remote sensed study of the urban effect on land T_{surf} has been critical in characterizing large-scale spatial and temporal patterns of sUHI (Peng et al., 2012; Streutker, 2003; Imhoff et al., 2010). However, the methodological and conceptual concerns raised in Stewart (2011) in combination with the wide (and broadening) range of methodologies for remote sensed urban T_{surf} retrieval should prompt critical assessment of the remote sensed sUHI literature. At the time of writing, no systematic or critical reviews of the remote sensed sUHI literature are

available, and questions raised in critical assessments of remote sensed urban T_{surf} in Roth et al. (1989) and Voogt and Oke (2003) have gone largely unaddressed. An increasingly dogmatic focus on improving spatial and radiometric resolutions has left other biases in remote sensing of urban environments largely ignored in sUHI literature. This suggests that similar conclusions to those found of aUHI literature in Stewart (2011) are possible (if not likely) for study of sUHI. Assessment of these biases is, therefore, paramount to ensure assessments of the urban effect on T_{surf} are robust, methodologically valid, and comparable across techniques, space, and time.

1.1 Biases and shortcomings in thermal remote sensing of urban T_{surf}

Traditional methods for urban T_{surf} measurement are subject to a suite of geometric and temporal biases. Geometric biases are the result of urban modification of surface structure and thermal and radiative properties combined with the narrow field-of-view (FOV) viewing geometry of conventional remote sensors:

Undersampling of surface 3-dimensionality by narrow-FOV remote sensors

Relative to typical non-urban and rural terrain, urban development adds significant 3-dimensionality to the surface. This added complexity results in undersampling of the complete urban surface by narrow-FOV remote sensors. A narrow-FOV sensor ”sees” a different assemblage of urban surfaces depending on its viewing direction, resulting in a geometric bias towards some arrangement of facets; i.e. viewing from the nadir, a narrow-FOV sensor sees the urban surface as an array of rooftops and roads, the same sensor viewing the

surface from an oblique angle sees some array of walls, rooftops, and roads depending on its orientation. For a sensor in the nadir, increasing FOV introduces sampling of vertical features. To illustrate how sensor-surface geometry influences sampling of the urban surface by narrow- and wide-FOV sensors, Figure 1.1 shows FOVs for the three sensor orientation/type combinations.The vast majority of urban thermal remote sensing is done via a narrow-FOV sensor viewing from the nadir.

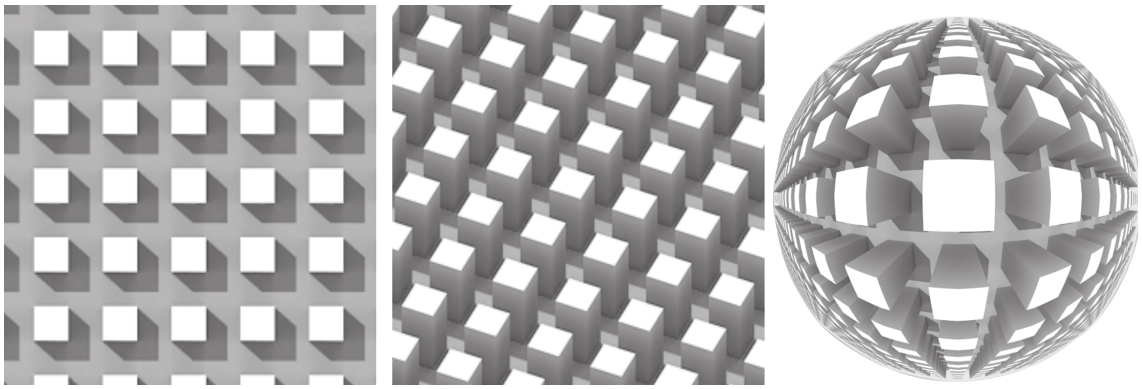

Figure 1.1: Projected FOVs for a narrow-FOV sensor at nadir and oblique angles, and a wide-FOV hemispherical sensor viewing an idealized urban array with building width W, height $2W$, and inter element spacing W. Figure from Adderley et al. (2015) under a Creative Commons Attribution 4.0 License.

Directional dependence in remote sensed urban T_{surf}

In addition to modifying how a remote sensor samples the surface, the convoluted 3-dimensional structure of the urban surface modifies the surface radiation budget, resulting in strong micro-scale spatiotemporal contrasts in urban T_{surf}, which depend on surface-sun geometry. These microscale variations in urban T_{surf} are often amplified by significant geometric and spatial contrasts in the thermal admittance of common urban materials, which determines the diurnal amplitude of T_{surf} for a given facet. Thus, when viewed from a narrow-FOV remote

sensor with some inherent geometric bias, urban T_{surf} is directionally dependent - constituting an "effective anisotropy" of urban T_{surf}, shown in Figure 1.2. The qualifier "effective" is used to differentiate directional contrasts in urban T_{surf} that arise from a city's 3-dimensional surface structure from those resulting from the non-Lambertian nature of individual urban facets (e.g. walls, rooftops, or roads). The magnitude of urban effective anisotropy can reach up to 10 to 12 K and is highly dependent on surface-sensor-sun geometry, surface structure, and urban materials (Krayenhoff and Voogt, 2016; Voogt and Oke, 1997; Lagouarde et al., 2012).

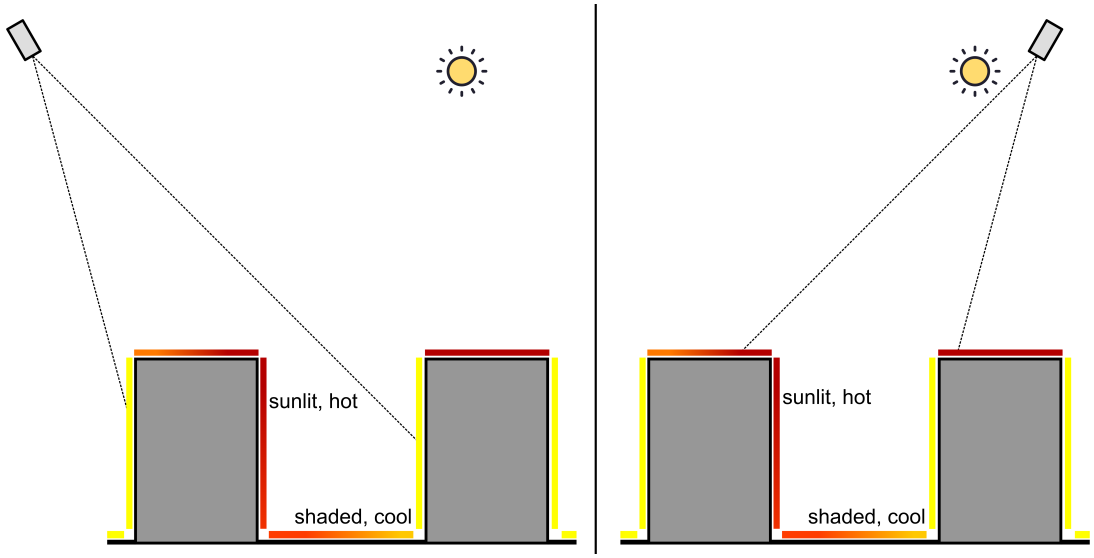

Figure 1.2: A narrow-FOV sensor viewing an idealized urban surface from two angles. Left: viewing the surface approximately perpendicular to the sun's angle. Right: viewing the surface approximately parallel to the sun's angle. The two viewing angles yield different remote sensed T_{surf} by sampling different arrangements of sunlit and shaded features. Both will deviate from an area weighted "complete" urban T_{surf}.

Geometric undersampling by narrow-FOV remote sensors results in differences in remote sensed urban T_{surf} based on a sensor's viewing direction and the assemblage of facets included within the sensor FOV. A sensor viewing the surface perpendicular (parallel) to the sun's angle will tend to underestimate (overestimate) the "true" complete urban surface

temperature - often calculated as an area weighted average of wall, rooftop, and road T_{surf} - by differentially biasing sunlit or shaded facets. Similarly, a sensor in the nadir will tend to overestimate daytime urban T_{surf} and underestimate nighttime T_{surf}, from a bias towards rooftop facets that are differentially hot by day and cool by night and a neglect of wall facets which are differentially cooler by day and warmer by night. As the effect of geometric biases is highly dependent on surface-sensor-sun geometry and requires significant instrumentation for observation, its influence in the remote sensed sUHI record is presently unknown.

Temporal biases in thermal remote sensing of urban areas occur across multiple time scales including the following:

Contamination by turbulence forced, high frequency fluctuations in urban T_{surf}

Using time-sequential thermography Christen et al. (2012) found that many common urban fabric types (e.g. rooftops, walls, roads, and vegetation) display large micro-scale (second to minute) fluctuations in T_{surf}. The magnitude of these is inversely related to surface thermal admittance and is currently, poorly understood. Most thermal remote sensors provide instantaneous, rather than temporally averaged, T_{surf} and thus are subject to contamination by high-frequency fluctuations. These biases are difficult to estimate in urban environments, where a large variety of fabric materials can produce significant geometric and spatial contrasts in thermal admittance — and thus directional and spatial variations in the magnitude of microscale fluctuations depending on the facet material types viewed by the sensor.

Discontinuity in satellite overpass cycles.

Overpass cycles for polar orbiting sensors are discontinuous. These sensors provide data for the vast majority of urban T_{surf} study. Assessment of land T_{surf} either sacrifices spatial

resolution for a daily repeat cycle - as is the case with MODIS - or sacrifices temporal resolution for a higher spatial resolution - ASTER or Landsat. These satellites cannot be used to assess the temporal development of sUHI without significant interpolation. Work in Freitas et al. (2013), Zakšek and Oštir (2012), and Weng and Fu (2014) used thermal images from geostationary satellite remote sensors to overcome this limitation, but a coarse spatial resolution limits the applicability of these methods in complex heterogeneous urban areas, especially at mid to high latitudes. Similar work in Huang et al. (2016) and Zhou et al. (2013) used an annual temperature cycle and diurnal temperature cycle genetic algorithm respectively to interpolate climatologies of urban T_{surf} and sUHI from discontinuous data. However, the diurnal and seasonal urban T_{surf} cycles presented in these studies are only applicable under "ideal" cloudless conditions and are specific to test cities. In general, studies that address temporal discontinuities in the urban T_{surf} record are not the norm and the vast majority of sUHI study remains temporally sparse.

Clear-sky bias

Clouds absorb TIR radiation. Thus, satellite remote sensing of TIR radiation emitted by the surface requires clear sky conditions. Although the urban effect on T_{surf} is most evident under "satellite friendly" clear sky conditions (manifesting as large sUHI magnitudes), a clear sky bias likely entails overestimation of "all-sky" sUHI and further adds to discontinuities in the remote sensed urban T_{surf} record.

As is the case with geometric biases, the magnitude of these temporal biases in remote sensed urban T_{surf} is difficult to quantify without long-term ground truthing campaigns or significant interpolation. As such, the true temporal and geometric nature of urban effect on T_{surf} and thus sUHI is presently unknown.

1.2 Research questions and objectives

Prompted by these shortcomings in the remote sensed urban T_{surf} record, and in an effort to better understand the temporal and geometric aspects of sUHI, this thesis introduces a method to provide hemispherical, temporally continuous urban T_{surf} for sUHI analysis to address the following questions:

1. What is the nature of urban surface temperature when viewed from a hemispherical downward-facing radiometer? And how does it relate to urban temperatures derived from other methods for urban surface temperature retrieval?
2. What is the diurnal and seasonal nature of the surface urban heat island effect?

In an attempt to answer these questions, this thesis

- Develops and evaluates a method to retrieve atmospherically corrected hemispherical radiometric urban surface temperatures from time-continuous measurements of upwelling longwave radiation.
- Compares urban surface temperatures and surface urban heat island magnitudes retrieved using the method to common remote sensed representations of the urban surface.
- Derives two long term climatologies of hemispherical urban surface temperatures to observe seasonal and diurnal patterns of the surface urban heat island effect in Basel, Switzerland and Vancouver, Canada.

The following two chapters address questions one and two respectively. Chapter 2 details and evaluates a method to retrieve atmospherically corrected, hemispherical urban T_{surf} from

time-continuous measurements of upwelling longwave radiation. Chapter 3 explores the temporal and geometric nature of sUHI through long-term climatological analysis of hemispherical sUHI and compares sUHI magnitudes from several common remote sensed representations of the urban surface.

References

Christen, A., Meier, F., and Scherer, D. (2012). High-frequency fluctuations of surface temperatures in an urban environment. *Theoretical and Applied Climatology*, 108(1-2):301–324.

Freitas, S. C., Trigo, I. F., Macedo, J., Barroso, C., Silva, R., and Perdigão, R. (2013). Land surface temperature from multiple geostationary satellites. *International Journal of Remote Sensing*, 34(9-10):3051–3068.

Gastellu-Etchegorry, J. P., Demarez, V., Pinel, V., and Zagolski, F. (1996). Modeling radiative transfer in heterogeneous 3-D vegetation canopies. *Remote Sensing of Environment*, 58(November 1995):131–156.

Howard, L. (1833). *The climate of London*, volume 1 - 3. Harvey and Dorton, London.

Huang, F., Zhan, W., Voogt, J., Hu, L., Wang, Z., Quan, J., Ju, W., and Guo, Z. (2016). Temporal upscaling of surface urban heat island by incorporating an annual temperature cycle model: A tale of two cities. *Remote Sensing of Environment*, 186:1–12.

Imhoff, M. L., Zhang, P., Wolfe, R. E., and Bounoua, L. (2010). Remote sensing of the urban heat island effect across biomes in the continental USA. *Remote Sensing of Environment*, 114(3):504–513.

Krayenhoff, E. S., Christen, A., Martilli, A., and Oke, T. R. (2014). A Multi-layer Radiation Model for Urban Neighbourhoods with Trees. *Boundary-Layer Meteorology*, 151(1):139–178.

Krayenhoff, E. S. and Voogt, J. A. (2016). Daytime thermal anisotropy of urban neighbourhoods: Morphological causation. *Remote Sensing*, 8(2):1–22.

Lagouarde, J. P., Hénon, A., Irvine, M., Voogt, J., Pigeon, G., Moreau, P., Masson, V., and Mestayer, P. (2012). Experimental characterization and modelling of the nighttime directional anisotropy of thermal infrared measurements over an urban area: Case study of Toulouse (France). *Remote Sensing of Environment*, 117:19–33.

Lowry, W. P. (1977). Empirical estimation of urban effects on climate: a problem analysis. *Journal of Applied Meteorology*, 16:129–135.

Martilli, A., Clappier, A., and Rotach, M. W. (2002). An urban surface exchange parameterization for mesoscale models. *Boundary-Layer Meteorology*, 104:261–304.

Masson, V. (2000). A physically-based scheme for the urban energy budget in atmospheric models. *Boundary-Layer Meteorology*, 94(3):357–397.

Oke, T. R., Mills, G., Christen, A., and Voogt, J. A. (2017). *Urban Climates*. Cambridge University Press.

Peng, S., Piao, S., Ciais, P., Friedlingstein, P., Ottle, C., Bréon, F. M., Nan, H., Zhou, L., and Myneni, R. B. (2012). Surface urban heat island across 419 global big cities. *Environmental Science and Technology*, 46(2):696–703.

Roth, M., Oke, T. R., and Emery, W. (1989). Satellite-derived urban heat islands from three

coastal cities and the utilization of such data in urban climatology. *International Journal of Remote Sensing*, 10(11):1699–1720.

Stewart, I. D. (2011). A systematic review and scientific critique of methodology in modern urban heat island literature. *International Journal of Climatology*, 31(2):200–217.

Streutker, D. (2003). Satellite-measured growth of the urban heat island of Houston, Texas. *Remote Sensing of Environment*, 85(3):282–289.

United Nations (2014). World Urbanization Prospects: The 2014 Revision. Technical report, Department of Economic and Social Affairs.

Voogt, J. A. and Oke, T. R. (1997). Complete urban surface temperatures. *Journal of Applied Meteorology*, 36(9):1117–1132.

Voogt, J. A. and Oke, T. R. (2003). Thermal remote sensing of urban climates. *Remote Sensing of Environment*, 86(3):370–384.

Weng, Q. and Fu, P. (2014). Modeling diurnal land temperature cycles over Los Angeles using downscaled GOES imagery. *ISPRS Journal of Photogrammetry and Remote Sensing*, 97:78–88.

Zakšek, K. and Oštir, K. (2012). Downscaling land surface temperature for urban heat island diurnal cycle analysis. *Remote Sensing of Environment*, 117:114–124.

Zhou, J., Chen, Y., Zhang, X., and Zhan, W. (2013). Modelling the diurnal variations of urban heat islands with multi-source satellite data. *International Journal of Remote Sensing*, 34(21):7568–7588.

Chapter 2

An atmospheric correction method to derive hemispherical time-continuous urban surface temperature

2.1 Introduction

TIR remote sensing of land surface temperature has emerged as a primary research focus in climatology, as researchers seek to better describe spatiotemporal patterns of T_{surf} globally and better understand how anthropogenic modification of the Earth's surface influences land T_{surf} and impacts climate at various scales. Over the last two decades, application of thermal remote sensing to study surface climates has expanded significantly. Thermal remote sensing of the Earth's surface has applications over a wide range of disciplines: from informing micro-, urban-, and global-scale climate models, to aiding decision making and mitigation praxis with respect to climate change and the urban heat island effect.

Within urban climatology, a combination of satellite, aerial, and ground-based thermal remote sensors have been integral in elucidating the spatial (Roth et al., 1989), temporal (Peng et al., 2012), and geometric (Voogt and Oke, 1997) effects of the built environment on land T_{surf}; in evaluating and partitioning urban surface energy balances (Bastiaanssen W. G. M. et al., 1998; Yamaguchi and Kato, 2005; Frey et al., 2007) and; in characterizations of the relationship between surface and boundary-layer air temperatures (T_{air}) (Stoll and Brazel, 1992). These advances have been aided by substantial improvements in sensor spatial, spectral, and radiometric resolutions, and by the proliferation of both large-scale public satellite remote sensing campaigns and low-cost aerial and near-ground thermography. However, in spite of its widespread usage, several questions concerning the use and validity of urban remote thermal remote sensing, first posed in Roth et al. (1989), have yet to be sufficiently answered, viz,

1. What is the nature of the surface 'seen' by a thermal remote sensor?
2. How does T_{surf} observed by a remote sensor relate to the 'true' temperature governing the surface-atmosphere interface?

In this paper, we seek to examine question two by introducing and evaluating a method for atmospheric correction of near-ground hemispherical TIR radiation - measured via pyrgeometer - for hemispherical radiometric temperature ($T_{hem,\,r}$) retrieval. These measures are common to most urban energy balance assessments because they are made as a part of the net radiation measurement and thus constitute a hitherto untapped method for urban T_{surf} analysis. A companion paper responds to question one through an analysis of two long term climatologies of $T_{hem,\,r}$ and derived surface UHI magnitudes (sUHI), to quantify geometric and temporal biases across multiple methods for remote sensing of urban T_{surf}.

2.2 Atmospheric effects on TIR radiation

Although most thermal remote sensors operate within one of the atmospheric windows - where atmospheric effects are minimal - virtually any remote sensed TIR signal is subject to radiative effects from the layer of atmosphere between the surface and the sensor. Over much of the thermal infrared waveband the atmosphere emits radiation and absorbs a fraction of radiation emitted by the surface. Thus, a remote sensed TIR signal is almost certainly not equal to the ground emitted signal. Spectral radiance received by a sensor at height (z) can be described by a function deviating from a Planck curve at T_{surf} based on the spectral transmittance of the intervening atmosphere, with the magnitude of that deviation determined by the difference between Planck curves calculated from T_{surf} and ambient T_{air}. A radiative transfer code, such as MODTRAN (Berk et al., 1987), can be used to model the effect of the atmosphere on a remote sensed TIR signal. Radiative transfer simulations run in MODTRAN version 4.1 for two path lengths are shown in Figure 2.1, for spectral radiance emitted from a planar surface at 300 K through an isothermal atmosphere at 290 K, water vapor content of 12 $\mathrm{g\,m^{-3}}$, and aerosol and trace gas profiles from the mid-latitude summer standard atmosphere (Kantor and Cole, 1962). At both short and long path lengths, radiance in each band shows some deviation from the ground emitted signal. Larger deviations are observed at longer path lengths, where a significant portion of the resulting signal is emitted from the atmosphere, even in bands with high spectral transmittance. Long path lengths and a less transmissive atmosphere increase the potential for deviation in a remote sensed TIR signal from the ground emitted signal, while the difference between T_{air} and T_{surf} determines the resulting magnitude of atmospheric influence.

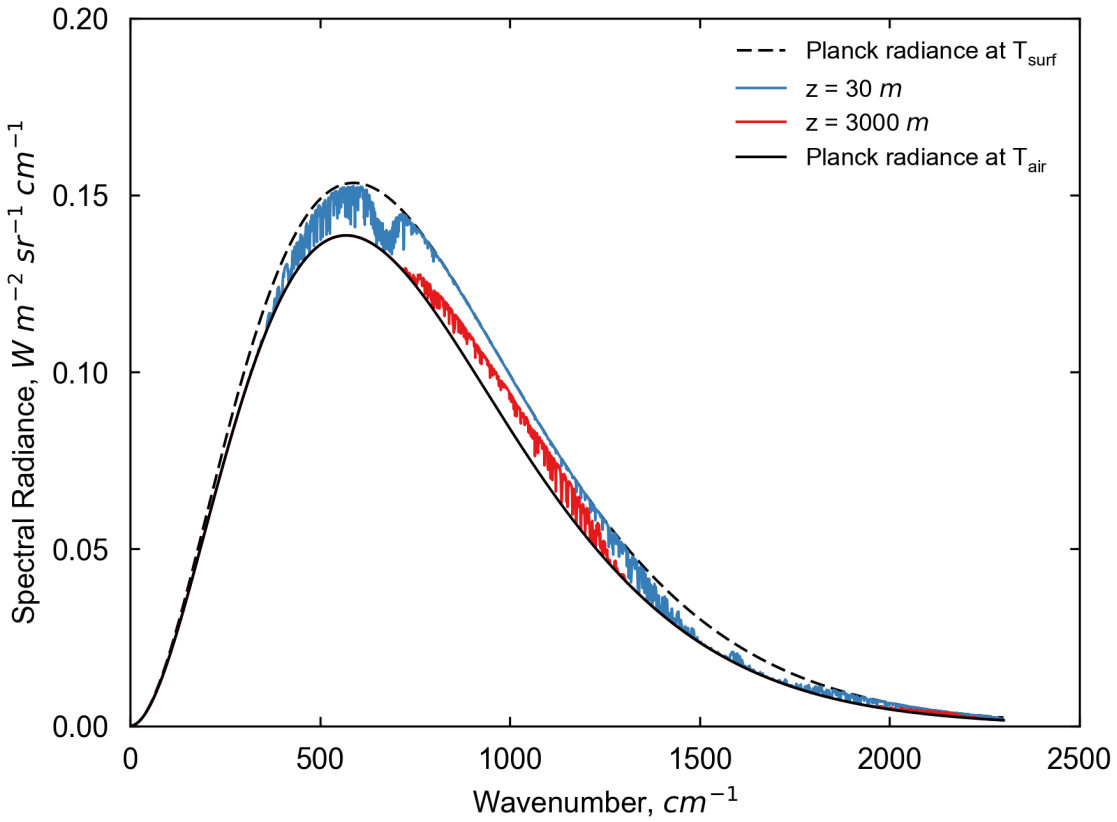

Figure 2.1: At-sensor spectral directional radiances computed in MODTRAN 4.1 (Berk et al., 1987) for short (30 m) and long (3000 m) path lengths (z) with Planck curves indicating spectral radiances at T_{surf} = 300 K and T_{air} = 290 K.

Atmospheric effects can lead to differences between the 'true' radiometric T_{surf} and the remote sensed T_{surf} of over 10 K for satellite platforms (Cooper and Asrar, 1989) and over 6 K for near-ground sensors (Meier et al., 2011). Moreover, because atmospheric effects are a function of non-uniform and spatiotemporally variant surface and atmospheric properties, their associated errors change depending on instrument type, surface-sensor geometry, study location, and ambient conditions. As intersite and time-continuous analysis is a significant goal

of most thermal remote sensed studies (urban or otherwise) these effects cannot be ignored.

Spectral transmission of longwave radiation through a given layer of atmosphere is dependent on total column absorber content (the principal broadband TIR absorbers are H_2O, CO_2, and to a lesser extent O_3, N_2O, CO, CH_4, and O_2 (Miskolczi and Guzzi, 1993)). Holding vertical absorber content constant through a layer of atmosphere, variation in band-by-band transmittance of TIR radiation with path length is greatest at the scale of an urban canyon (approximately 1 to 50 m), where transparent spectral bands can quickly become opaque with small changes in path length or absorber content - illustrated in Figure 2.2. Indeed, atmospheric influence on TIR radiation may be most complex when measured near the surface. The addition of complex, 3-dimensional urban surface structure may further complicate quantification and removal of atmospheric effects on near-ground remote sensed TIR radiation.

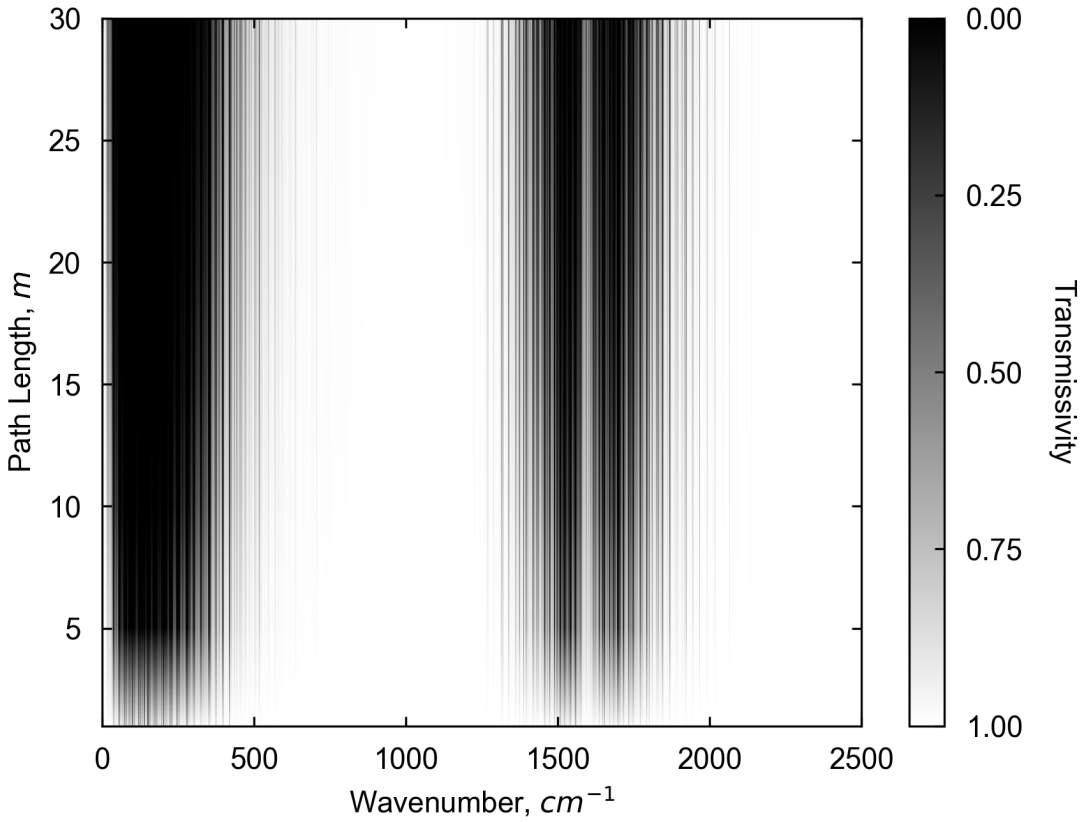

Figure 2.2: Spectral transmission of water vapor as a function of height. Model results from MODTRAN 4.1 for radiance emitted from a planar surface at 300 K through an atmosphere with water vapor content of 8 $\mathrm{g\,m^{-3}}$. Sampled at heights of 1, 5, 10, 15, 20, 25, and 30 m.

2.2.1 Describing radiation as received by a remote sensor

Radiation passing through a layer of atmosphere from an emitting surface towards a sensor can be described in a number of ways: *Spectral directional radiance* $R_z^{\uparrow}(\lambda, \theta, \phi)$, at height z, wavelength λ and from a direction defined by viewing zenith angle θ, and azimuth angle ϕ is commonly written as

$$R_z^{\uparrow}(\lambda,\theta,\phi) = \tau_\lambda \epsilon_\lambda R_0^{\uparrow}(\lambda) + (1-\epsilon_\lambda) R_{sky}^{\downarrow}(\lambda) + (1-\tau_\lambda) R_{atm}^{\uparrow}(\lambda) \tag{2.1}$$

where ϵ_λ is spectral surface emissivity, τ_λ is spectral "slab" transmittance through the layer between the emitting surface ($z = 0$) and z. Directional radiances upwelling from the atmosphere $R_{atm}^{\uparrow}$, and the surface $R_0^{\uparrow}$, and downwelling from the sky $R_{sky}^{\downarrow}$, can be described spectrally or integrated over a waveband bounded by λ_1 and λ_2 as Planck's law

$$R(\theta,\phi) = \int_{\lambda_1}^{\lambda_2} R(\lambda,\theta,\phi)\, d\lambda = \frac{\epsilon_\lambda C_1}{\pi\lambda^5 \left(\exp\left(\frac{C_2}{\lambda T} \right) \right)} \tag{2.2}$$

where $C_1 = 3.7404 \cdot 10^8\ W\mu^4 m^{-2}$, $C_2 = 14387 \mu K$, and T is emitter temperature.

Measured by a narrow-FOV sensor mounted at height z, $R_z^{\uparrow}(\lambda,\theta,\phi)$ passes through an instrument filter (or dome) with spectral transmittance τ_d, and is integrated over the sensor waveband to yield a *directional radiance* L'_z as 'seen' by the sensor

$$L'_z(\theta,\phi) = \int_{\lambda_1}^{\lambda_2} \tau_d(\lambda) R_z^{\uparrow}(\lambda)\, d\lambda \tag{2.3}$$

which, integrated over the hemisphere with respect to zenith θ angle and azimuth ϕ angle, yields an *irradiance* L at height z,

$$L_z = \int_0^{2\pi} \int_0^{\pi/2} L'_z(\theta,\phi)\ \cos\theta \sin\theta\, d\theta d\phi \tag{2.4}$$

2.2.2 Relating TIR and surface temperature

TIR radiation received by a remote sensor can be related to a surface temperature in a number of ways — each producing different conceptions of T_{surf} from different instrument and sensor types. As such, the term ”surface temperature” with respect to a remote sensed TIR radiation is vague and can refer to several definitions of ”surface” and ”temperature”. Thus, proper terminology must be attached to land T_{surf} inferred from TIR radiation. Definitions and nomenclature conventions for multiple methods for T_{surf} retrieval are discussed at length in Norman and Becker (1995).

Irradiance L_z received by a broadband hemispherical sensor (such as a pyrgeometer), can be used to infer a *hemispherical brightness temperature* $T_{hem,\,b}$ through an inversion of the Stefan-Boltzmann law,

$$T_{hem,\,b} = \sqrt[4]{\frac{L_z}{\sigma}} \tag{2.5}$$

where σ is the Stefan-Boltzmann constant.

A *directional brightness temperature* $T_{bright}\,(\theta, \phi)$ from some viewing angle described by θ and ϕ can be inferred from directional radiance via equation 2.5 by replacing L_z with L'_z multiplied by a coefficient. This method is commonly used to infer $T_{bright}\,(\theta, \phi)$ from infrared thermometers (IRT) operating over the atmospheric window - where atmospheric effects are minimal and T_{bright} is a reasonably accurate approximation of T_{surf}. However, constants must be calibrated for the range of expected T_{surf} as the relationship between L_z and L'_z is not perfectly linear with respect to emitter temperature.

Inversions of uncorrected L_z or L'_z yield a temperature equal to that of a blackbody emitting the same amount of radiation as detected by the sensor. Since L_z is unlikely to be equal

to L_0 and, by extension, L'_z is unlikely to be equal to L'_0, $T_{hem,\,b}$ at $z = 0$ and $T_{hem,\,b}$ at z often show significant deviation. Hence, T_{bright} and $T_{hem,\,b}$ are generally considered only a rough approximation representation of radiometric T_{surf}.

To retrieve a more accurate estimation of the 'true' T_{surf}, the same inversions can be applied to TIR measurements after correction for atmospheric effects (e.g. modification of the remote sensed TIR signal to represent the same signal at $z = 0$ emitted from a homogeneous, isothermal, blackbody emitter) to yield a *directional radiometric surface temperature* T_{rad} from atmospheric corrected directional radiances and a *hemispherical radiometric surface temperature* $T_{hem,\,r}$ from atmospherically corrected irradiances. T_{rad} and $T_{hem,\,r}$ provide a better approximation of the true T_{surf} by representing the temperature at which emitting surfaces are radiating, integrated over the sensor FOV.

2.2.3 Atmospheric correction of near-ground TIR radiation

A large number of correction routines have been developed to remove atmospheric and emissivity effects from aerial and satellite TIR signals and derive accurate T_{rad}. Methods range from simple mono-window (Qin et al., 2001) and split-window (Wan and Dozier, 1996) routines for single-channel and multi-channel remote sensors, to schemes that integrate a radiative transfer code to isolate the surface emitted signal from interfering signals. Boundary conditions are standard across most correction methods: generally requiring vertical profiles of T_{air}, humidity, pressure, and aerosol content to remove atmospheric effects, and surface radiative properties to correct for emissivity effects. However, correction methods are often instrument (or, at the very least, platform) specific and difficult to generalize across sensor and platform types. Few methods exist for correction of ground based remote sensed TIR radiation — none of these are robust enough to correct irradiances measured from a near-ground

wide-field-of-view (FOV) radiometer mounted to view rough terrain.

Atmospheric correction of near-ground remote sensed TIR radiation is subject to a unique set of challenges compared to traditional satellite and aerial platforms. Wide-FOV remote sensors have complex, multiple line-of-sight (LOS) path length geometries - illustrated in Figure 2.3 for a downward facing pyrgeometer. Surface-sensor geometry varies significantly over the sensor FOV as some path lengths intersect with raised vertical, sloped, and horizontal features. This creates the potential for non-uniform atmospheric effects over the sensor FOV and necessitates a multi-LOS correction to retrieve accurate $T_{hem,\,r}$. In effect, with near-ground wide-FOV sensors, surface geometry is non-trivial and must be represented in atmospheric correction routines. In contrast, over a scene retrieved via satellite, spatial viability in surface geometry and LOS angle have a negligible effect on path length. Atmospheric correction routines for satellite retrieved TIR radiation, therefore, assume uniform or single-LOS geometry because the TIR signal passes through a relatively constant volume of atmosphere over the projected sensor FOV, regardless of surface geometry.

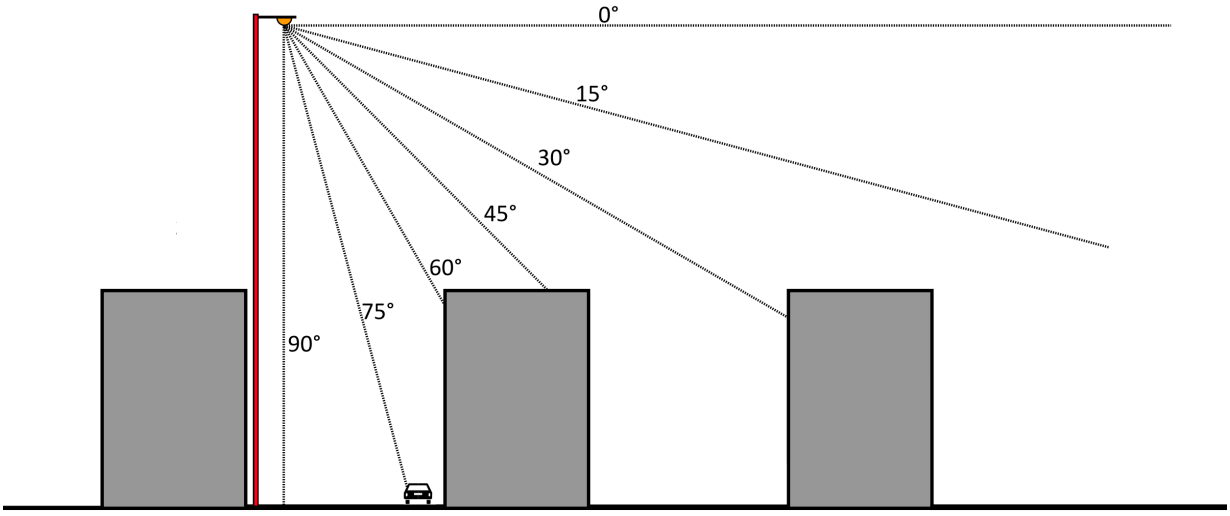

Figure 2.3: Variable path geometry inherent with wide-FOV near-ground sensor visualized over an idealized 2-dimensional urban area.

Several multi-LOS correction routines have been developed to remove atmospheric effects on near-ground remote sensed TIR radiation: Meier et al. (2011) describes a correction method for oblique angled thermal imagery of urban terrain. In the method, spatially distributed LOS geometries were calculated by linking each image pixel to the corresponding 3-d coordinates of its viewpoint on a digital building model (DBM). Path lengths were then calculated as the distance between each pixel's corresponding location on the DBM and the sensor represented as the vanishing point of a 3-dimensional pyramidic projection from the sensor's location in the DBM. A pixel-by-pixel correction was then applied to remove atmospheric effects and retrieve T_{rad} for each pixel at 30 minute intervals, resulting in a brief, time-continuous climatology of urban T_{rad}. However, the method uses thermal images in conjunction with a DBM to calculate path length geometries for each pixel's LOS - a technique not possible with a pyrgeometer, which returns a single integrated value over the sensor FOV. Moreover, the target instrument operates over a narrow waveband with relatively uniform spectral sensor response, reducing the magnitude and variance in atmospheric transmission over the sensor response curve. Thus, the method is not directly generalizable to correct TIR radiation measured via pyrgeometer.

Kotani and Sugita (2009) describes a method for correction of wide-FOV (pyrgeometer) TIR irradiances over a homogeneous planar surface. In this method, path lengths were calculated for six sensor heights. Radiances were then modeled using the LOWTRAN (Kneizys et al., 1988) radiative transfer code initialized at 5° intervals and integrated over the hemisphere to retrieve irradiances for a suite of T_{surf}, and ambient T_{air} and humidities. The resulting lookup table (LUT) of values is then used to correct L_z and quantify atmospheric effects on remote sensed L_z measured from several sensor heights.

The two existing methods are limited to narrow-FOV thermal imagers and planar terrain respectively. Thus, for atmospheric correction of TIR radiation upwelling from urban terrain

measured via downward facing pyrgeometer a method which combines Meier et al. (2011)'s representation of complex surface geometry and Kotani and Sugita (2009)'s broadband hemispherical integration is needed.

2.3 A "rolling lookup table" method for hemispherical atmospheric correction

The "rolling lookup-table" method described in this study uses a sensor view model in conjunction with a radiative transfer code to model hemispherical irradiances upwelling from a simplified isothermal 3-dimensional representation of the urban surface. In summary, the method (depicted in Figure 2.4) uses vertical profiles of measured T_{air} and humidity to model at-sensor spectral radiances at 5° increments over the sensor FOV for a predetermined range of possible $T_{hem,\,r}$ at each time-step. Spectral directional radiances are convolved by a dome transmittance curve, integrated over the sensor waveband, and weighted for their respective angular view factor. Weighted directional radiances are then integrated over the hemisphere and aggregated into a LUT of modeled irradiance - $T_{hem,\,r}$ pairings for each time step, unique to the vertical profile of measured T_{air} and humidity. Finally, for each time step, measured irradiances are matched with the closest modeled irradiances in the LUT to return an atmospherically corrected radiometric hemispherical surface temperature. This process is repeated at 30 minute intervals to yield a continuous climatology of urban $T_{hem,\,r}$. The following sections introduce the study area for which the method was developed and describe the sensor view model, radiative transfer, and post-processing steps of the correction method.

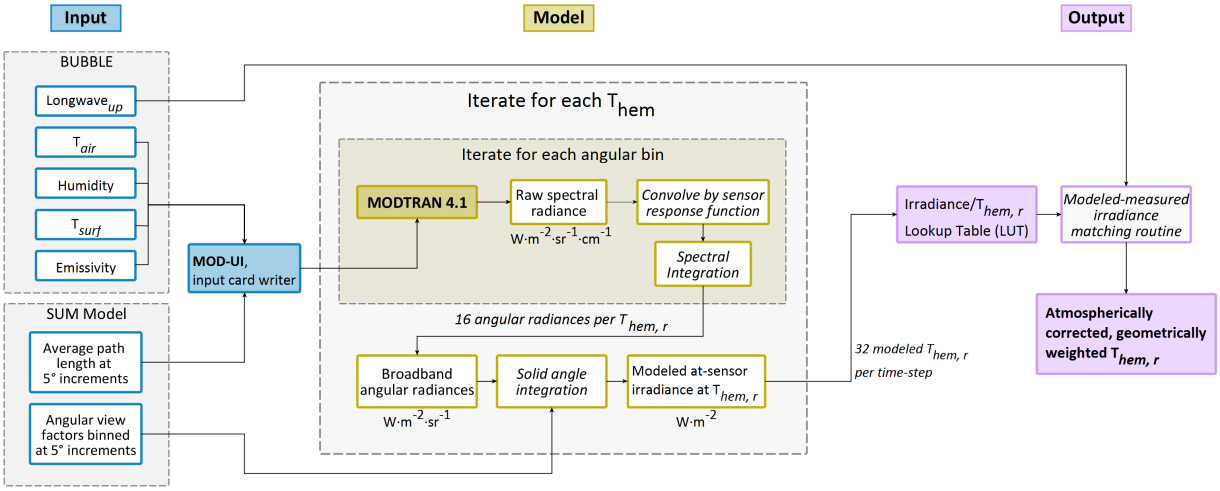

Figure 2.4: A workflow schematic depicting the input, model, and output-processing steps of a ”rolling lookup table method” for hemispherical radiometric surface temperature retrial.

2.3.1 Study area

As discussed in section 2.2.3, atmospheric correction of longwave irradiances measured from downward-facing, near-ground, wide-FOV sensors must account for complex surface geometry. Thus, routines to retrieve atmospherically corrected urban $T_{hem, r}$ from upwelling longwave irradiances are inherently site specific. However, it is important to note that although correction *magnitudes* described in this paper are not necessarily generalizable, the correction *method* described in this paper can readily be adapted to different study sites, sensor types, and unique surface geometries.

With methodological generalizability in mind, a ”rolling lookup table” atmospheric correction method was developed to retrieve radiometric $T_{hem, r}$ for a climatology of upwelling longwave irradiances measured from above the Sperrstrasse street canyon in Basel, Switzerland. The site, instrumented as a part of the Basel Urban Boundary Layer Experiment (BUBBLE) Rotach et al. (2005), has an approximately northeast-southwest orientation and site morphology

representative of local climate zone (LCZ) 2[1] Stewart and Oke (2012). LCZ classification was based on an assessment of surface characteristics in a 250 m circular area extending from the Sperrstrasse tower using a 1 m raster digital building model (DBM). Thus, the morphological parameters identified in Rotach et al. (2005) are representative of a majority of the pyrgeometer footprint. Vegetation was not included in the DBM, and is not represented in morphological assessment or the sensor view model, however, the street canyon and surrounding area has little vegetation. The location of the Sperrstrasse urban site and the two rural reference sites used in sUHI analysis are included in Figure 2.5.

[1] Site surroundings can be described by the following morphological parameters: mean building height: 14.6m, plan aspect ratio: 0.54, complete aspect ratio: 1.92, local canyon aspect ratio: 1.0, and average shortwave albedo: 0.11 (Rotach et al., 2005).

Figure 2.5: The BUBBLE study site in Basel, Switzerland with urban and rural site locations indicated.

For the eight month period between December 2001 and July 2002 of the BUBBLE campaign, a triangular lattice tower was installed within the Sperrstrasse street canyon. Its location was offset towards the southeast facing wall near the along-canyon center of the canyon. Instruments to observe a full suite of meteorological variables and fluxes of heat, mass, and momentum were mounted at various levels on the tower. Profiles of T_{air} and humidity were measured at seven heights extending from 2.5 m to 31.5 m above the canyon floor (with the highest observation level at approximately 2.17 times mean roof level). Upwelling and downwelling short/longwave fluxes were obtained from radiometers mounted at the lowest and highest measurement levels, with an additional downward facing pyrgeometer mounted at roof level near the center of the street canyon. In addition, during a month-long summertime intensive observation period (IOP) an array of narrow-FOV IRTs was installed to sample representative individual facet surface temperatures (T_{facet}). A schematic of the locations of IRTs and pyrgeometers within the Sperrstrasse canyon is included in Figure 2.6. A subset of the BUBBLE dataset is available at http://ibis.geog.ubc.ca/~achristn/research/BUBBLE/data.html. The full dataset was supplied courtesy of Dr. Roland Vogt at the University of Basel and Dr. Andreas Christen at the University of British Columbia.

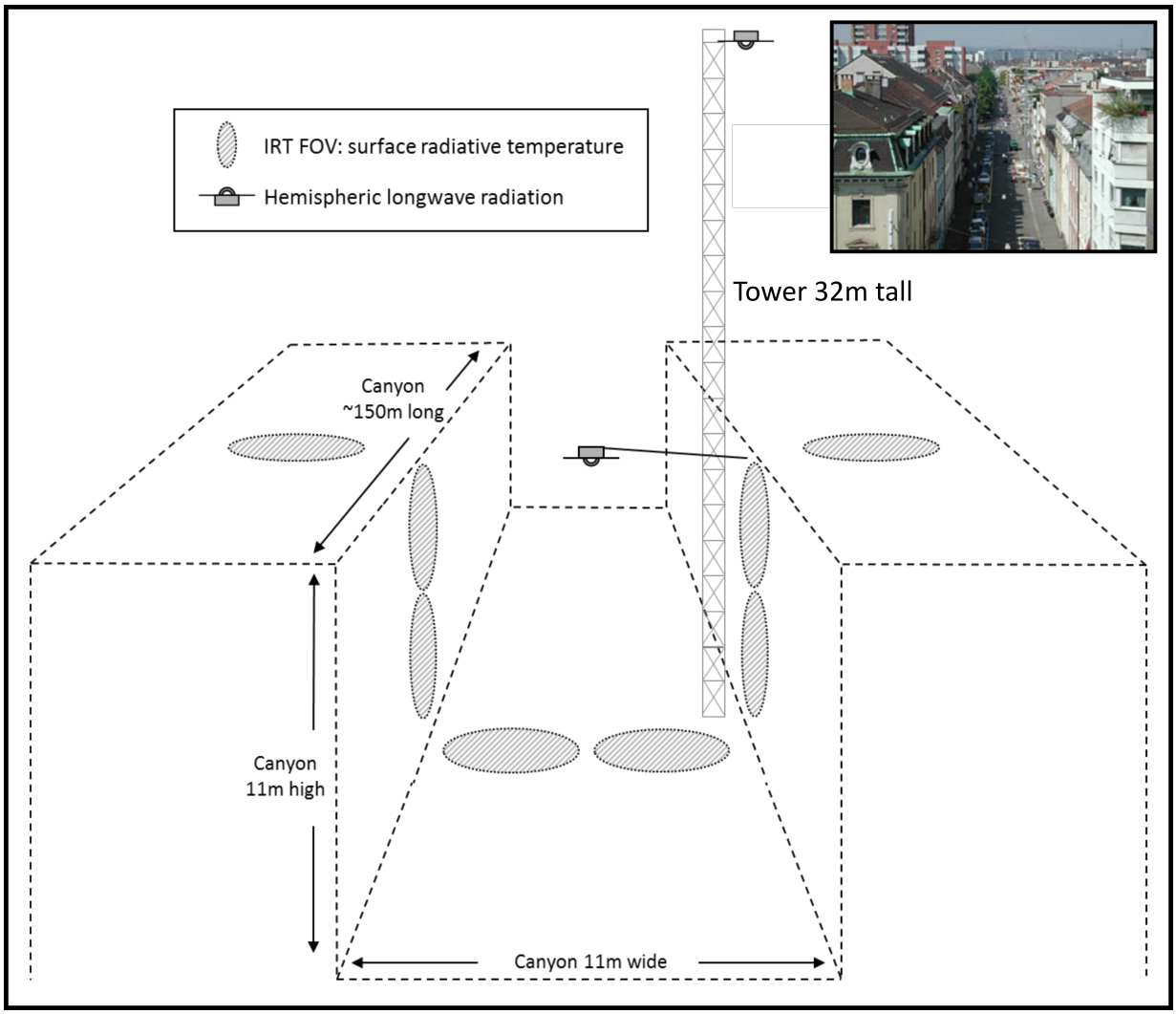

Figure 2.6: A schematic showing the TIR radiation instrument setup at the Sperrstrasse urban canyon. Pyrgeometer locations and IRT FOVs for roof, wall, and road facets are indicated. Only instruments relevant to this work are included in the schematic. The along canyon axis is approximately ENE - WSW (i.e. the north-south line is approximately perpendicular to the canyon axis).

The BUBBLE Sperrstrasse site was chosen here for two primary reasons: 1. The site provided a long-term climatology of radiation and meteorological variables for a representative mid-latitude city. This allowed for examination of urban T_{surf}, sUHI, and atmospheric correction magnitudes over a wide range of representative mid-latitude conditions. 2. Inclusion of T_{facet} over the IOP allows for investigation of the effect of sensor FOV and viewing direction on remote sensed urban T_{surf} for common methods for urban T_{surf} retrieval. This directional dependence of urban T_{surf} - termed "effective anisotropy" - refers to the notion that a remote sensed TIR signal can vary based on the combined effects of surface-sensor-sun geometry and the convoluted, 3-dimensional structure of the urban surface Voogt and Oke (1998).

Facet surface temperatures measured during the summertime IOP allow for direct climatological comparison of $T_{hem,\,r}$ to common remote sensed representations of the urban surface calculated from weighted averages of wall (T_{wall}), road (T_{road}), and roof (T_{roof}) temperatures. Plan and complete aspect ratios are used to derive weightings for nadir remote sensed (T_{plan}) and complete (T_{comp}) representations of urban surface temperature - described in Table 2.1. T_{comp} represents a complete urban T_{surf}, where facet temperatures are averaged based on their proportion of the complete urban surface area, while T_{plan} represents the Sperrstrasse site as viewed by a narrow-FOV remote sensor in the nadir. To facilitate comparison over the IOP, $T_{hem,\,r}$ and T_{plan} were divided by T_{comp} and averaged at each time step over the IOP to yield normalized mean $T_{hem,\,r}$ and T_{plan} at 30-minute intervals. Through comparison of $T_{hem,\,r}$ to T_{plan} and T_{comp} we investigate the effect of sensor-surface geometry on remote sensed urban T_{surf} and quantify directional biases in common urban T_{surf} measurements.

Table 2.1: Weights applied to individual facet temperature components in to calculate complete and nadir temperatures for the Basel Sperrstrasse street canyon.

	Road	Northwest Roof	Southeast Roof	Northwest Wall	Southeast Wall
Complete (T_{comp})	0.33	0.16	0.16	0.16	0.16
Nadir (T_{plan})	0.46	0.27	0.27	0.00	0.00

2.3.2 Modeling path lengths of 3-dimensional terrain

The sheer number of unique path length geometries inherent with wide-FOV radiometry of urban areas makes full 3-dimensional radiative transfer simulation difficult and computationally intensive - particularly when correcting a long-term climatology of irradiances or $T_{hem,\,r}$. In this method, to improve efficiency, radiances are calculated for azimuthally averaged path lengths that represent average surface-sensor geometry for each solid angle "slice" of the sensor FOV. Thus, hemispherical radiative transfer is reduced to a 2-dimensional problem similar to that shown in Figure 2.7. This greatly reduces the computational time required to model each irradiance - $T_{hem,\,r}$ pairing, as angular radiances can be computed as a function of zenith angle alone and subsequently weighted and integrated 3-dimensionally over the hemisphere.

To calculate surface-sensor geometries, the Surface-Sensor-Sun Urban Model (SUM) (Soux et al., 2004) is initialized with a simplified, orthogonal 3-dimensional DBM that represents surface geometry of the surrounding area. SUM uses a four-dimensional array to represent surface morphology with three spatial dimensions (x, y, and z), with z representing height above the x, y plane. An additional fourth dimension is used to store information describing each cell (in this case, distance from the point to the sensor). After specifying sensor position and FOV, the model determines which patches have an unobstructed line of sight to the

sensor and calculates distance from ”seen” patches to the sensor. Path lengths are binned at 5° increments of zenith angle and averaged to return an azimuthally-independent mean path length for each bin. In addition, while retrieving path length geometries, SUM calculates view factors for each solid angle ”slice”, which are later used to weight angular radiances in the hemispherical integration post-processing steps.

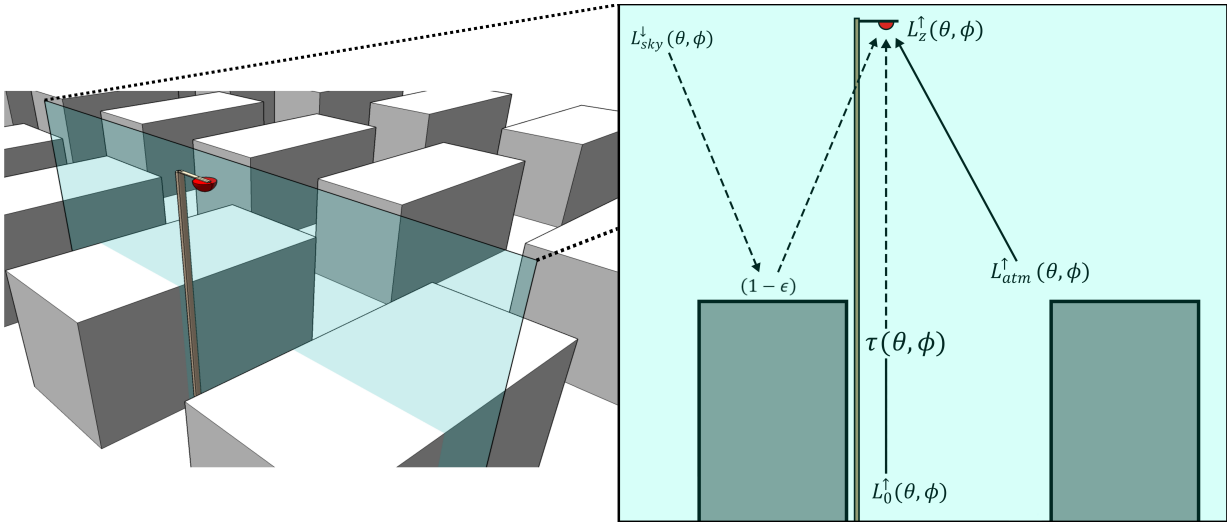

Figure 2.7: Path lengths over an urban surface. Left: a downward radiometer mounted above a simplified three-dimensional urban surface (Left) and the component radiances and path lengths from a vertical slice (Right). Dotted lines indicate radiation streams subject to absorption by the intervening atmospheric layer.

2.3.3 Modeling hemispherical irradiances

With path length geometries calculated in SUM, irradiances are modeled for each time step using version 4.1 of the MODerate resolution atmospheric TRANsmission radiative transfer code (MODTRAN) (Berk et al., 1987). At each time-step, a range of possible temperatures is specified (T_{spec}) based on $T_{hem,\,b}$ calculated from the measured irradiance with

$$T_{spec,\ min} = T_{hem,\ b} - 6\ K \tag{2.6}$$

defining a minimum T_{spec} before iterating over

$$T_{spec,\ i} = T_{spec,\ min} + \sum_{i=1}^{n} 0.5n,\ 1 \leq n \leq 32 \tag{2.7}$$

to retrieve a lookup table (LUT) of T_{spec}. This restricts

After the LUT is defined, at-sensor spectral radiances for each path length/zenith angle are modeled at an average urban emissivity of 0.95 (Oke, 1987) over a waveband of 0 - 2300 cm^{-1} for each T_{spec}. Profiles of T_{air} and humidity are retrieved from 30 min averages of conditions observed at the Sperrstrasse site. 30 min averages are used over raw 5 min values in order to smooth the input T_{air} and humidities and to cut down on the number of model runs needed to retrieve a long term climatology. The method can be adapted to any time interval. Aerosol, trace gas absorber, and above-sensor T_{air} and humidity conditions are defined by the mid-latitude summer standard atmosphere when daytime $T_{air,\ max}$ >10 °C (the mid-latitude winter profile is substituted on days where $T_{air,\ max}$ <10 °C) (Kantor and Cole, 1962).

In this method, a "typical" longwave bandpass - approximately 250 - 2300 cm^{-1} (4 - 42 $\mu\mathrm{m}$) - was extended to include much smaller wavenumber (longer wavelengths). This was done for two reasons: 1) To accurately represent broadband spectral longwave emission curves, which show significant emittance in wavenumber smaller than 250 cm^{-1} (wavelengths longer than 42 $\mu\mathrm{m}$). 2) To replicate the spectral signal "seen" by a silicone-domed pyrgeometer, which continues to transmit radiation at wavenumber <250 cm^{-1} (wavelengths >42 $\mu\mathrm{m}$). A "typical" longwave bandpass underestimates a pyrgeometer signal by approximately 7 - 10 $\mathrm{W\,m}^{-2}$, depending on emitter temperature. A comparison of typical and extended longwave bandpasses

is shown in Figure 2.8.

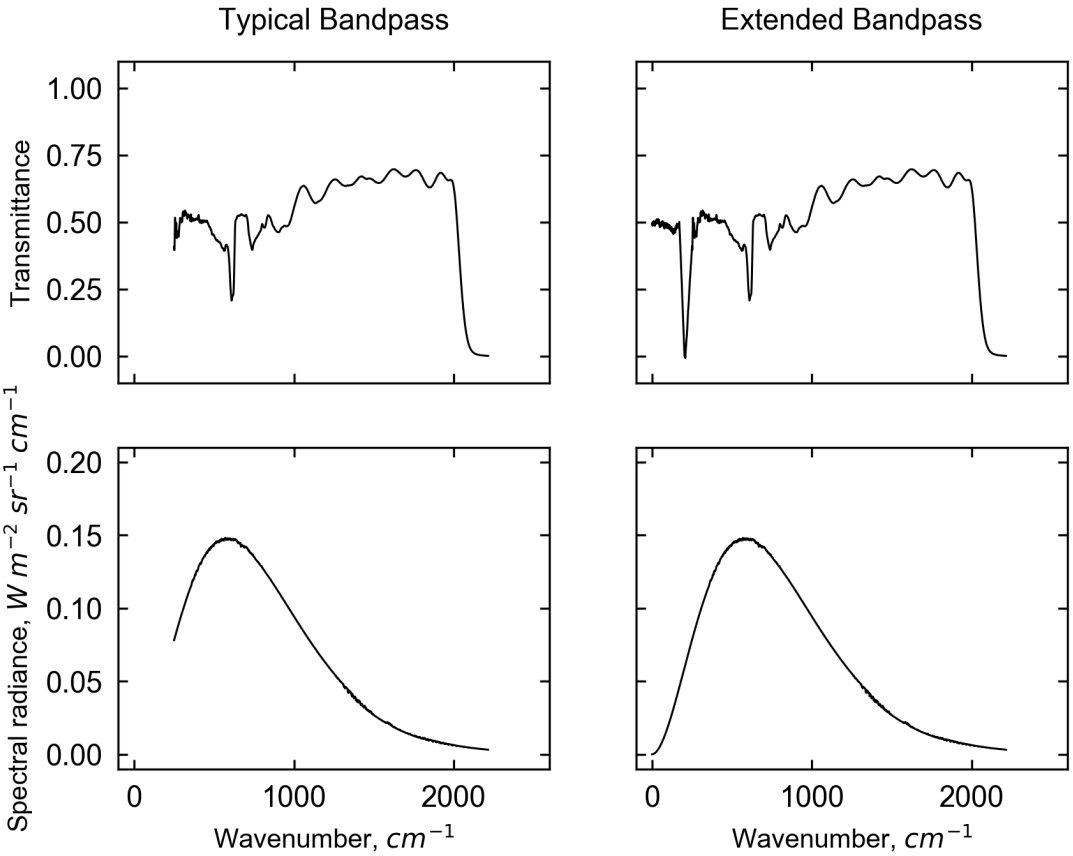

Figure 2.8: A comparison of dome transmittance for a Kipp & Zonen silicone domed pyrgeometer (data supplied by Kipp & Zonen, *pers. comm.*) and at-sensor radiance (T_{surf} = 300 K, T_{air} = 300 K, z = 30 m) for "typical" and extended bandpasses.

To replicate the signal received by the sensor, at-sensor spectral radiances computed by MODTRAN are convolved by a dome transmittance curve and integrated over the bandpass via

$$L'_z(\theta,\phi) = \frac{\int_{\nu_1}^{\nu_2} R(\theta,\phi,\nu)\, r(\nu)\, d\nu}{\overline{r}} \tag{2.8}$$

to yield a directional radiance L'_z with units $\mathrm{W\,m^{-2}\,sr^{-1}}$ for each θ over a waveband of ν_1= 0 $\mathrm{cm^{-1}}$ to ν_2 = 2300 $\mathrm{cm^{-1}}$. $\overline{r}$ is Planck weighted mean broadband sensor response computed as,

$$\overline{r} = \frac{\int R(\nu)\, r(\nu)\, d\nu}{\int R(\nu)\, d\nu} \tag{2.9}$$

where $R(\nu)$ is spectral radiance computed from a Planck function at an approximated emitter temperature and $r(\nu)$ is spectral sensor response.

$L'_z(\theta)$ are then multiplied by their associated angular view factor weighting (Φ) and integrated over the hemisphere to yield an irradiance L_z with units $\mathrm{W\,m^{-2}}$ with for the target $T_{\text{hem, r}}$

$$L_z(T_{\text{spec}}) = \int_0^{2\pi} \int_0^{\pi/2} L'_z(\phi, \theta)\ \Phi(\phi)\ d\theta d\phi \tag{2.10}$$

$L_z(T_{\text{spec}})$ is representative of at-sensor irradiance upwelling from the urban surface described in SUM at the target specified temperature $T_{\text{hem, r}}$ for the measured T_{air}, humidity, aerosol, and trace gas profile. The process is repeated to retrieve L_z for the range of potential $T_{\text{hem, r}}$ at the given time-step. Irradiance - $T_{\text{hem, r}}$ pairings are then aggregated into a LUT. Finally, the measured irradiance is matched with its closest modeled irradiance to yield an atmospherically corrected, radiometric hemispherical surface temperature for the given time step. The workflow is repeated at 30 min intervals to yield a time series of $T_{\text{hem, r}}$. Atmospheric correction magnitudes can then be calculated as the difference between $T_{\text{hem, r}}$ and $T_{\text{hem, b}}$, with $T_{\text{hem, b}}$ calculated via equation 2.5.

2.4 Evaluation of the method using profiles of upwelling longwave radiation over a homogeneous flat surface

MODTRAN has been shown to effectively model near-ground radiative transfer at urban canyon scale path lengths in 2-dimensions (Hoch, 2005; Hoch et al., 2007). However, the method described here accounts for complex 3-dimensional surface geometry, which can exert significant influence on atmospheric transmittance. In addition, the method includes significant post-processing to weight and integrate point-to-point spectral directional radiances to derive 3-dimensional, hemispherical irradiances. Thus, prior to deriving a climatology of urban $T_{hem,\,r}$, the method was evaluated using profiles of upwelling longwave irradiances measured over a simple flat surface. By testing the method using profiles of upwelling longwave radiation measured over a flat, relatively homogeneous, simple surface, we can assume that although each sensor "sees" a different patch on the ground, each sensor should see a patch with approximately the same surface temperature. Therefore, any differences in the signal between sensor heights is solely a product of atmospheric influence - which should be represented by MODTRAN given concurrent profiles of T_{air} and humidity. Thus, it follows that provided urban geometry and path lengths are accurately represented, the method should have similar accuracy over rough urban terrain.

For a continuous 14-day period, profiles of up/downwelling short/longwave radiation, T_{air}, and humidity measured from 2 m, 10 m, and 30 m were obtained from an instrumented tower in Payerne, Switzerland. Data were retrieved courtesy of Laurent Vuilleumier from the PANGEA data publishing portal. The tower, installed over a cultivated field as a part of the Baseline Surface Radiation Network (BSRN), is located approximately 100 km southwest of the BUBBLE Sperrstrasse tower and is subject to similar summertime conditions as the study site. The study period was chosen to include a comprehensive range of T_{surf}, T_{air}, humidities,

and cloud coverages to represent typical summertime conditions over which atmospheric effects on TIR radiation can vary significantly. To evaluate the method, we used a modified version of the workflow described in Figure 2.4. First, azimuthally averaged path lengths over a flat surface were calculated in SUM at 5° increments of zenith angle over the sensor FOV for the 10 m and 30 m sensors. For each time step, $T_{hem,\,b}$ calculated from the lowest L_z measurement was used to model irradiances at 10 m and 30 m at 30 min intervals using concurrent profiles of T_{air} and humidity. Daytime T_{air} observed at the highest measurement level was anomalously high compared to typical summertime lapse rates above flat vegetated terrain (Oke, 1987). This warm bias in T_{air} measured at 30 m is observed even under high wind velocities, where one would expect little vertical difference in temperature and certainly not a strong temperature inversion. The fact that the observed warming bias remains relatively constant over the 14-day study period prompted a slight modification to ensure the T_{air} profile between 10 m and 30 m was representative of the neutral or weakly unstable daytime conditions. It is likely that these modifications better represent the actual T_{air} profile in the layer between 10 m and 30 m than a simple interpolation between the 10 m T_{air} measurement and the anomalously warm 30 m T_{air} measurement.

Contrary to the findings in Kotani and Sugita (2009), an isothermal atmospheric profile was not sufficient to accurately model upwelling fluxes over flat terrain. Although thermal stratification is relatively small by day in an urban canyon (Nakamura and Oke, 1988) — where strong microscale contrasts in T_{surf} foster strong canyon mixing and neutral stability — the large daytime T_{surf} - T_{air} differential and the path length/transmittance gradient can create large differences in upwelling longwave forced by inter-canyon thermal contrasts - a phenomenon termed radiative divergence. By underestimating near-surface T_{air} and overestimating roughness-layer T_{air}, daytime divergences are underestimated by an isothermal profile. As such, a full canyon T_{air} and humidity profile is preferred to most accurately model near ground fluxes.

Modeled and measured upwelling longwave at 10 m and 30 m fluxes and divergences - calculated as the difference between 30 m and 10 m fluxes - are compared in Figure 2.9. Both fluxes and divergences show strong correlation, thus we conclude: First, irradiances measured near screen level (approximately 2 m above ground level) are not subject to significant atmospheric influence - as $T_{hem,\,b}$ inferred from $L_{z=2\ \mathrm{m}}$ was sufficient for modeling irradiances at 10 m and 30 m. As such, $T_{hem,\,b}$ and $T_{hem,\,r}$ are reasonably equal when z = 2 m. However, it should be noted that in urban areas a 2 m sensor is not sufficiently representative of canyon geometry and should not be used to derive urban $T_{hem,\,r}$. Second, MODTRAN can accurately model longwave fluxes and divergences above a flat, homogeneous surface over a wide range of temperatures, humidities, and cloud coverages and large contrasts in near-ground stability. At 30 m under typical summertime profiles of humidity, CO_2, and O_3, view factor weighted hemispherical transmittance over a flat surface is approximately 55% - meaning 45% of a broadband hemispherical TIR signal at 30 m is emitted by the atmosphere, rather than the target surface. As such, it is imperative that T_{air} profiles are well represented in MODTRAN to accurately model the atmospheric component of remote sensed TIR signal. As profiles of T_{air} in the layer between the surface and the sensor at the Sperrstrasse site are generally subject to neutral or weakly unstable conditions, with only rare stable stratifications, urban longwave divergences are likely to be smaller than those observed in this evaluation - and well approximated by MODTRAN. Thus, provided path length geometries are accurately replicated in by the sensor view model, we can reasonably assume that the method has similar effectiveness at the urban site.

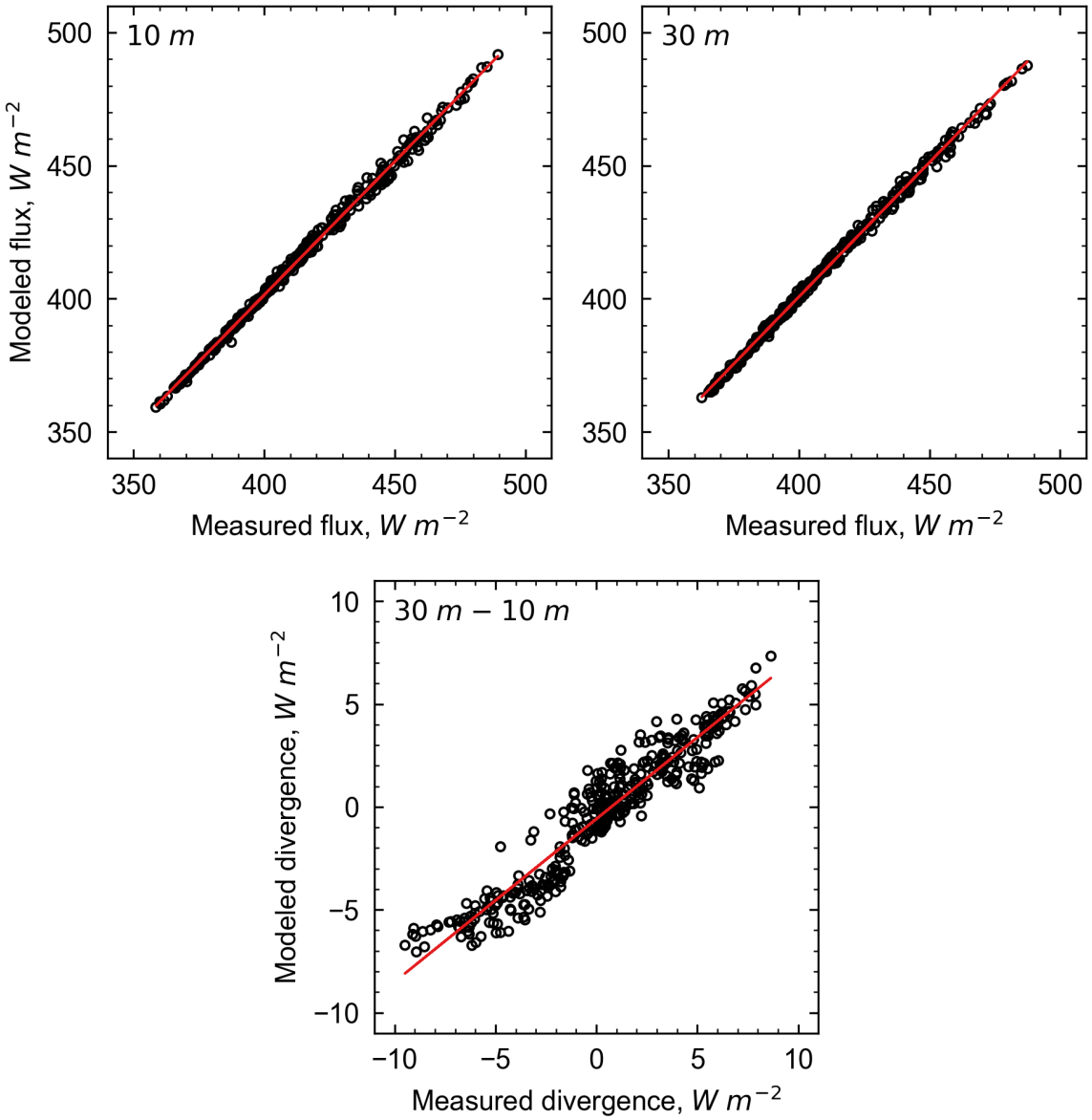

Figure 2.9: A comparison of 10 m and 30 m measured and modeled longwave fluxes and divergences - calculated as the difference between 30 m and 10 m fluxes - over the 14 day evaluation period at Payerne, Switzerland.

Table 2.2: Statistical performance of the Payerne evaluation. $RMSE_s$ and $RMSE_u$ represent the systemic and unsystematic RMSE respectively. The arrangement of statistical tests were selected from Willmott et al. (1985) and Willmott et al. (2012). n = 378

Statistic	10 m flux	30 m flux	Divergence
Slope	1.002	1.011	0.792
Intercept, ($\mathrm{W\,m^{-2}}$)	0.422	−3.560	−0.583
R^2	0.995	0.996	0.863
MAE, ($\mathrm{W\,m^{-2}}$)	1.781	1.325	1.191
RMSE, ($\mathrm{W\,m^{-2}}$)	2.204	1.690	1.423
$RMSE_s$, ($\mathrm{W\,m^{-2}}$)	1.444	0.851	1.028
$RMSE_u$, ($\mathrm{W\,m^{-2}}$)	1.666	1.460	0.985
d, agreement index	0.999	0.999	0.959

2.5 Results

2.5.1 Atmospheric correction magnitudes

Atmospheric correction magnitudes binned for season and time of day are shown in Figure 2.10. Summertime correction magnitudes show large day-to-day and diurnal variations. Variation is largest in summer near solar noon, where different synoptic conditions can force correction magnitudes of up to $8\ \mathrm{K}$ in clear-sky hot conditions and below $0\ \mathrm{K}$ under cooler overcast conditions. In winter, correction magnitudes display less variance and are smaller - approximately $2\ \mathrm{K}$ over a range of representative wintertime synoptic conditions.

Over both summer and winter seasons, correction magnitudes are strongly correlated with $\Delta T_{\mathrm{hem,\,r\,-\,air}}$. Figures 2.11 and 2.12 show the effect of seasonality and cloud cover on the relationship between correction magnitudes and $\Delta T_{\mathrm{hem,\,r\,-\,air}}$. The relationship is strongest and most evident in summer when variations in cloud cover can lead to large day-to-day contrasts in

solar input and $\Delta T_{surf\ -\ air}$, which translates into a wide range of correction magnitudes.

Figures 2.13 and 2.14 illustrate the relationship between correction magnitude and meteorological variables commonly measured as a part of climatological assessments of urban environments. A strong positive relationship is observed between correction magnitudes and incoming solar radiation. $T_{hem,\ r}$ and T_{air} display more complex relationships with correction magnitude, with a large cluster of observed correction magnitudes situated at a local minimum between 10 and $20\ ^{\circ}\mathrm{C}$, weakly negative correlation at temperatures lower than $10\ ^{\circ}\mathrm{C}$, and weakly positive correlation at temperatures greater than $20\ ^{\circ}\mathrm{C}$. Atmospheric water vapor content did not appear to exert significant control over correction magnitudes.

Figure 2.15 shows hemispherical atmospheric transmittance as a function of vapor pressure for pyrgeometers at $10\ \mathrm{m}$ and $30\ \mathrm{m}$ above a flat surface. Transmittances are modeled in MODTRAN 4.1 as the fraction of surface emission reaching the sensor for the path length and view factor geometries calculated in the method evaluation in Section 2.4. Hemispherical transmittance falls sharply with increasing vapor pressure between 0 and $5\ \mathrm{hPa}$, but is relatively constant with vapor pressure $>5\ \mathrm{hPa}$. This results in the weak correlation observed in Figure 2.14 between humidity and correction magnitude.

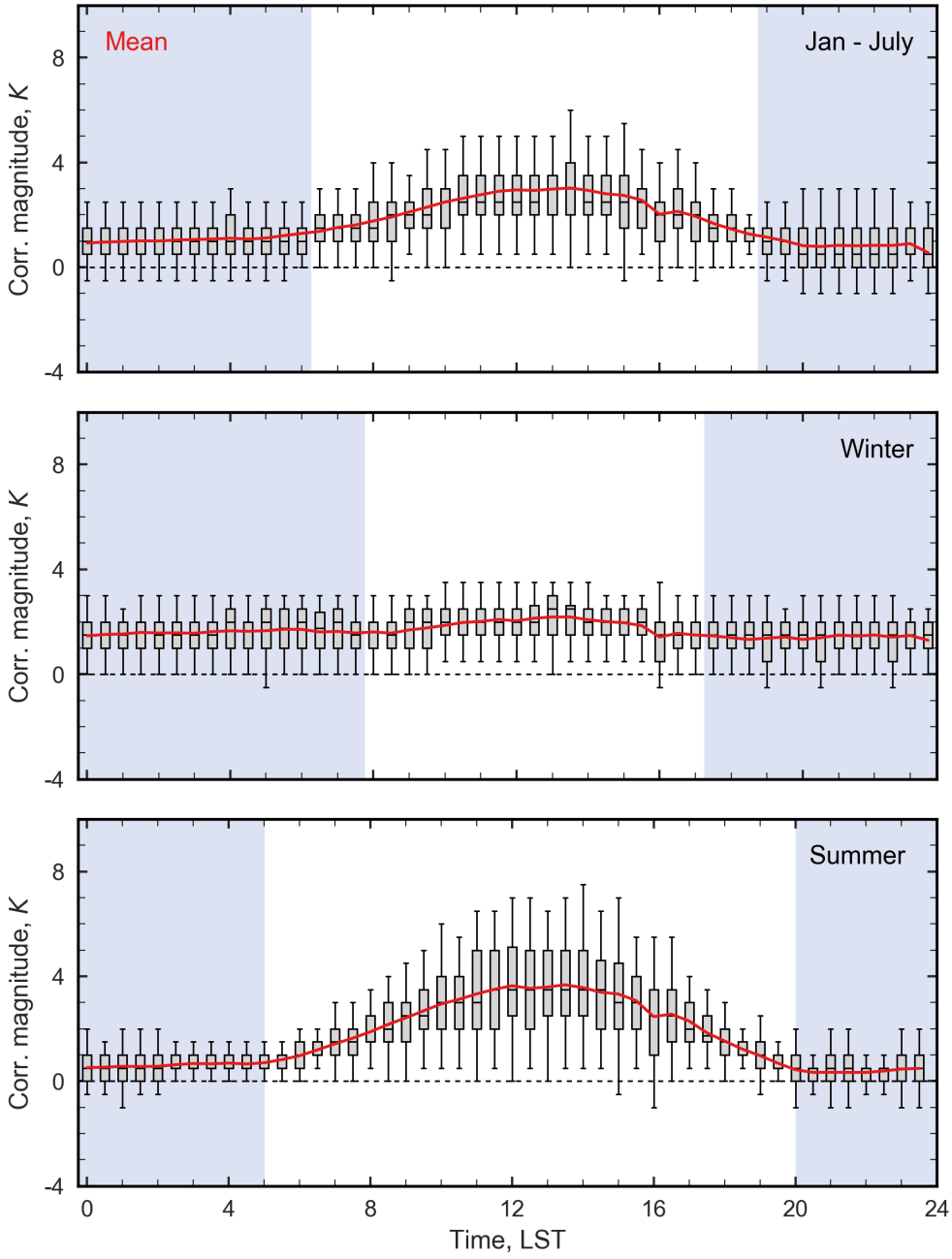

Figure 2.10: Atmospheric correction magnitudes calculated as the difference between $T_{hem,\,r}$ and $T_{hem,\,b}$ for the duration of the study period. Grey shading indicates nighttime. The red line indicates mean correction magnitude at each time step. Box edges represent the 25th and 75th percentiles with whiskers representing one standard deviation.

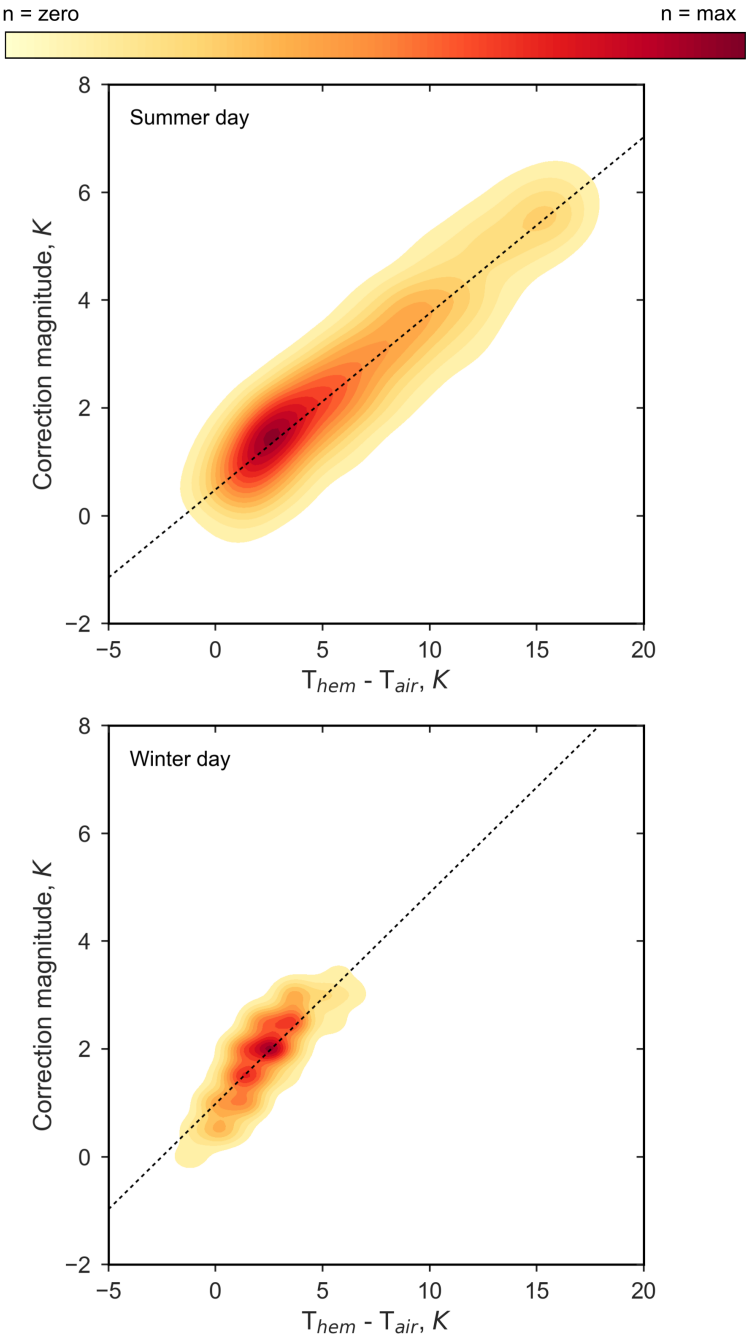

Figure 2.11: Correction magnitude versus $\Delta T_{hem,\, r\, -\, air}$ binned for season.

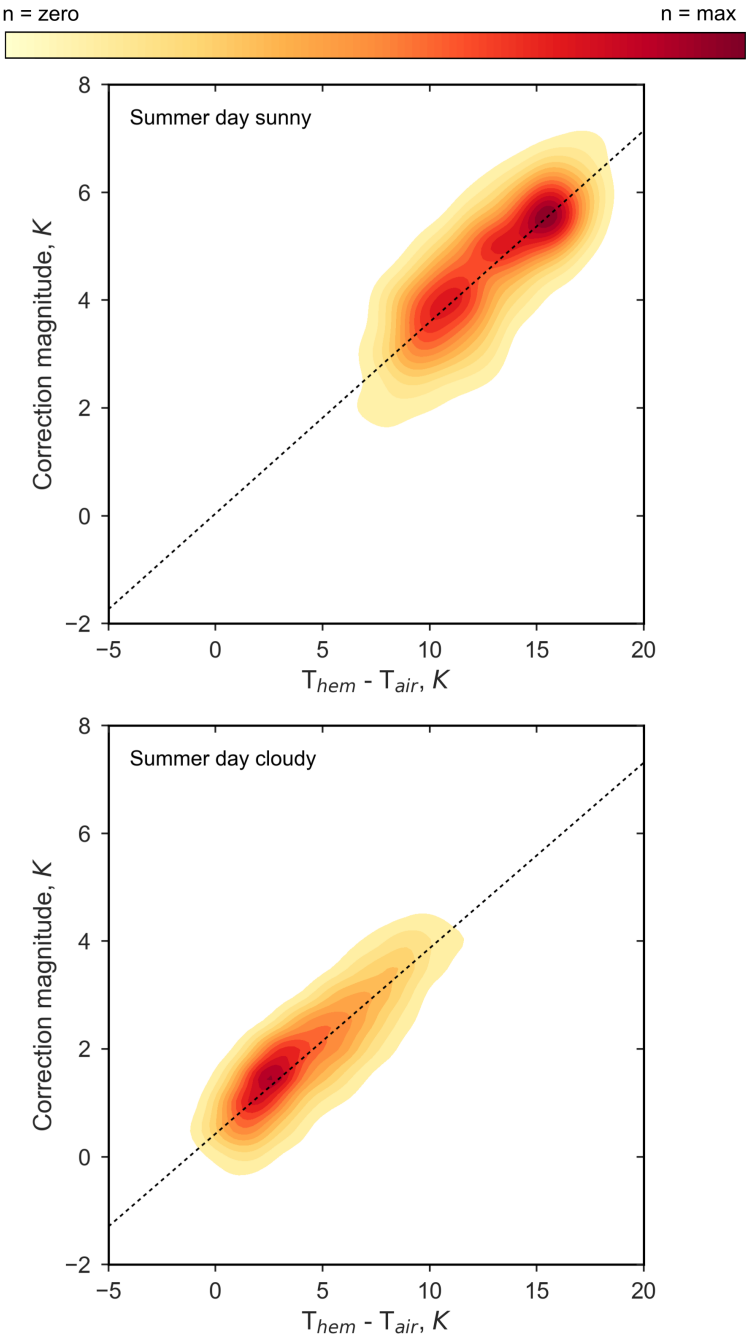

Figure 2.12: Correction magnitude versus $\Delta T_{hem,\, r\, -\, air}$ binned for clear and clouded days over the summer months.

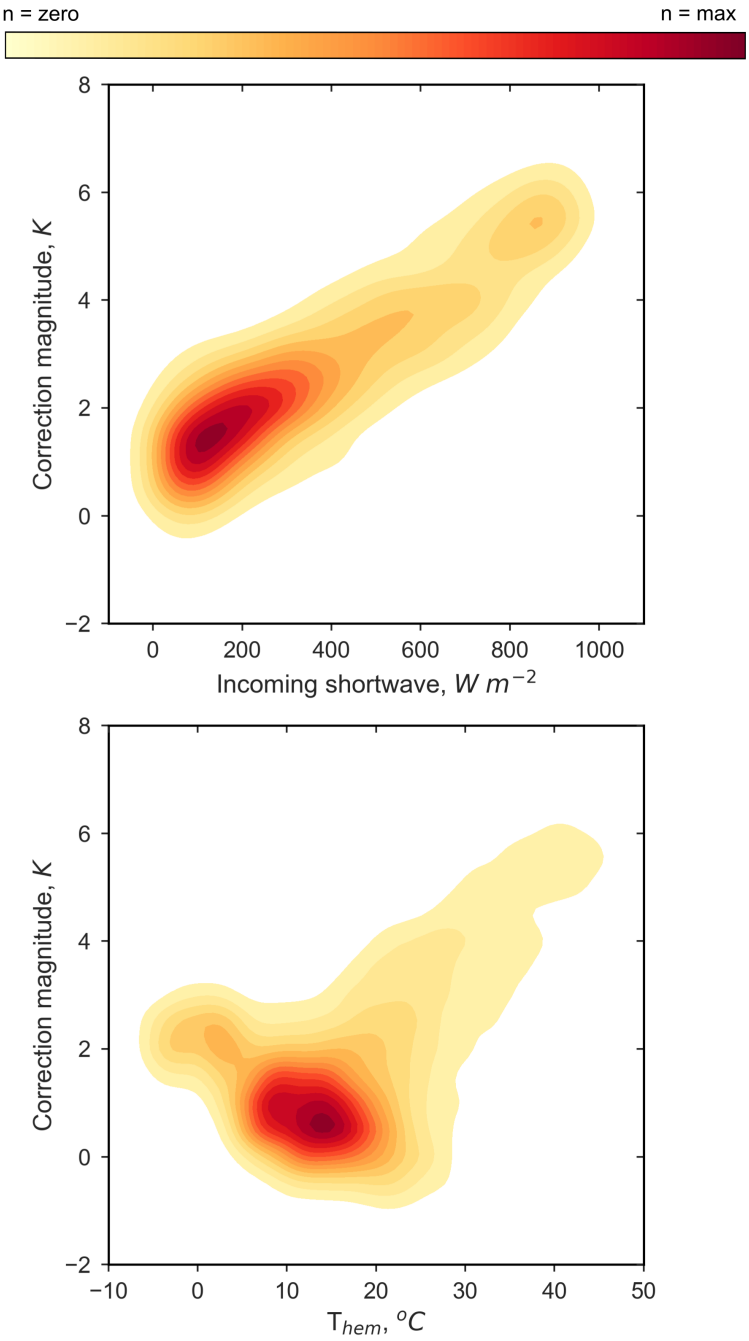

Figure 2.13: Correction magnitude versus incoming shortwave and $T_{hem, r}$ for the daytime hours of the study period.

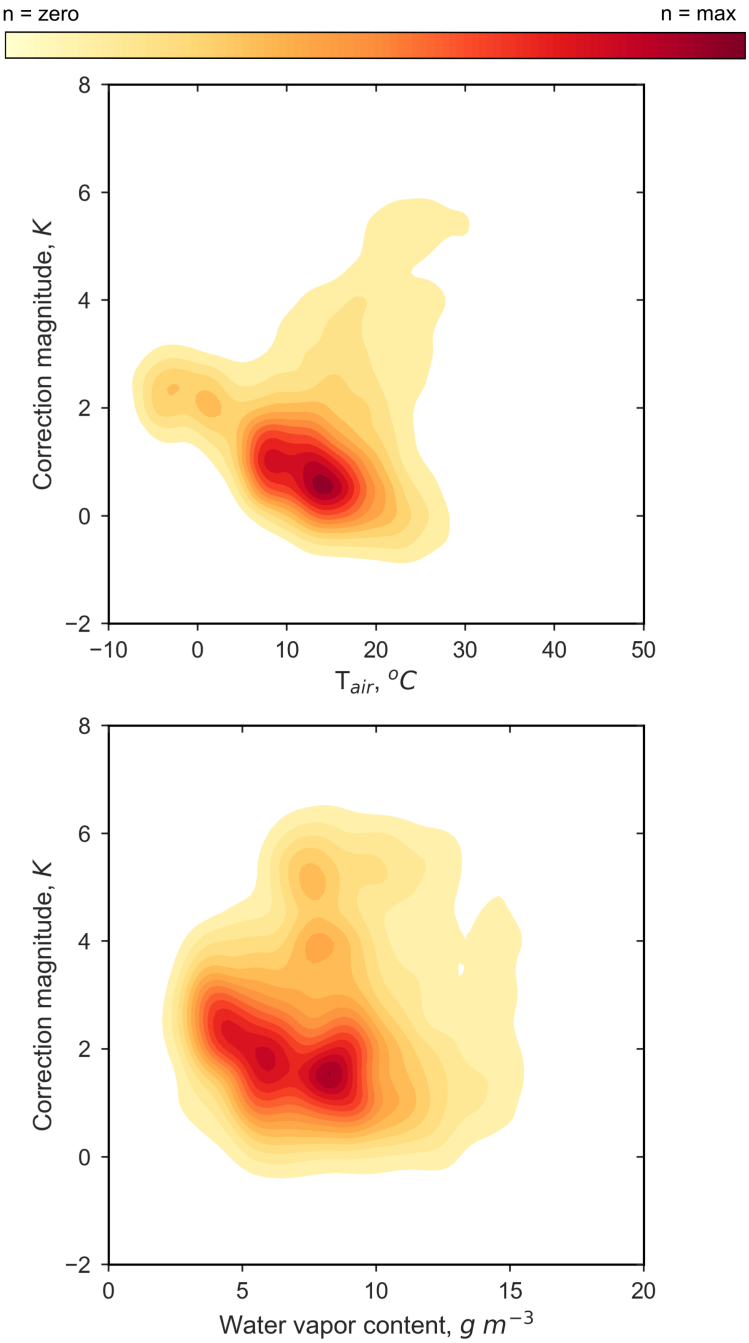

Figure 2.14: Correction magnitude versus T_{air} and water vapor content for the daytime hours of the study period.

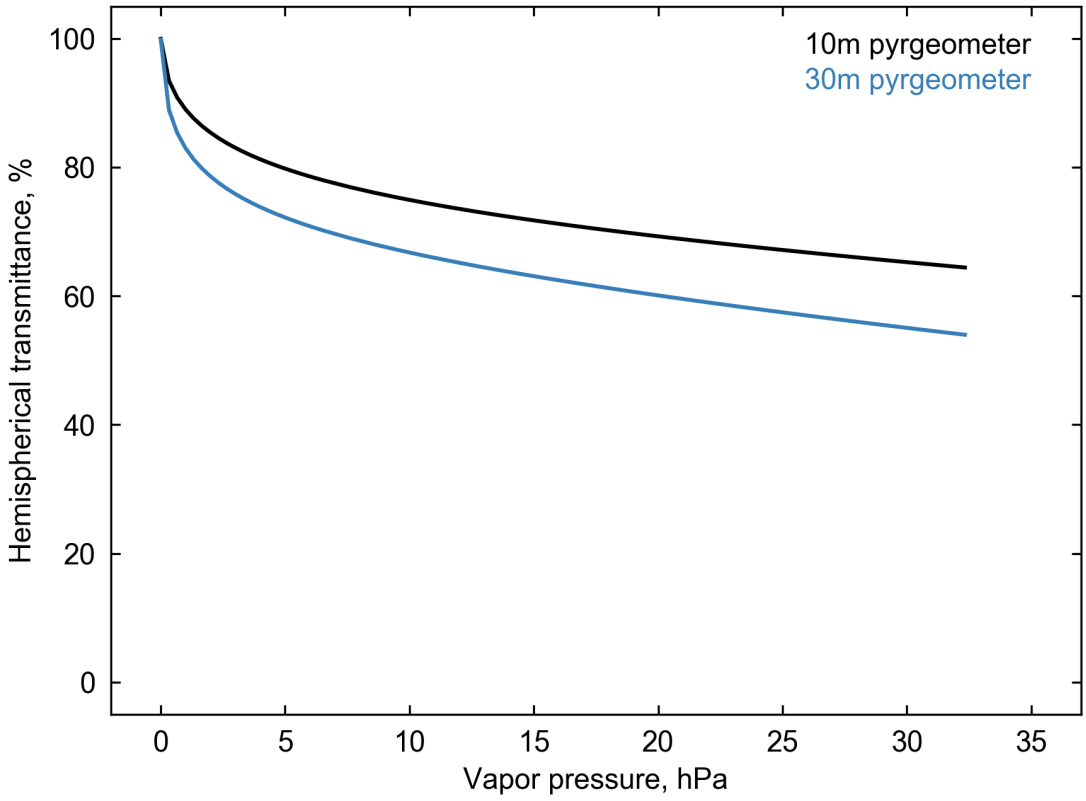

Figure 2.15: Hemispherical at-sensor atmospheric transmittance as a function of vapor pressure for two pyrgeometer heights (10 m and 30 m) over a flat surface. Calculated as the fraction of surface emission reaching the sensor height using MODTRAN 4.1 with $T_{surf} = T_{air} = 300$ K with water vapor as the sole atmospheric absorber.

2.6 Comparing T_{surf} from different sensor geometries

To illustrate the effect of sensor-surface geometry on remote sensed T_{surf}, Figure 2.16 shows a comparison of mean normalized $T_{hem,\,r}$ and T_{plan} calculated as T_x divided by T_{comp}, where T_x is $T_{hem,\,r}$ or T_{plan}, and averaged over the IOP. In the figure, overestimation of T_{comp} is observed at values above one and underestimation by values below one. Both $T_{hem,\,r}$ and T_{plan}

overestimate T_{comp} by day and underestimate T_{comp} by night. Mean daytime overestimation of T_{comp} by $T_{hem,\,r}$ is smaller and less variable than that by T_{plan}.

Mean normalized $T_{hem,\,r}$, T_{plan}, and $\Delta T_{plan\,-\,hem,\,r}$ are shown in Figure 2.17 along with clear sky and overcast sky case days. While mean $T_{hem,\,r}$ and T_{plan} display similar overestimations of T_{comp}, under clear sky conditions, overestimation by T_{plan} is much larger than that by $T_{hem,\,r}$.

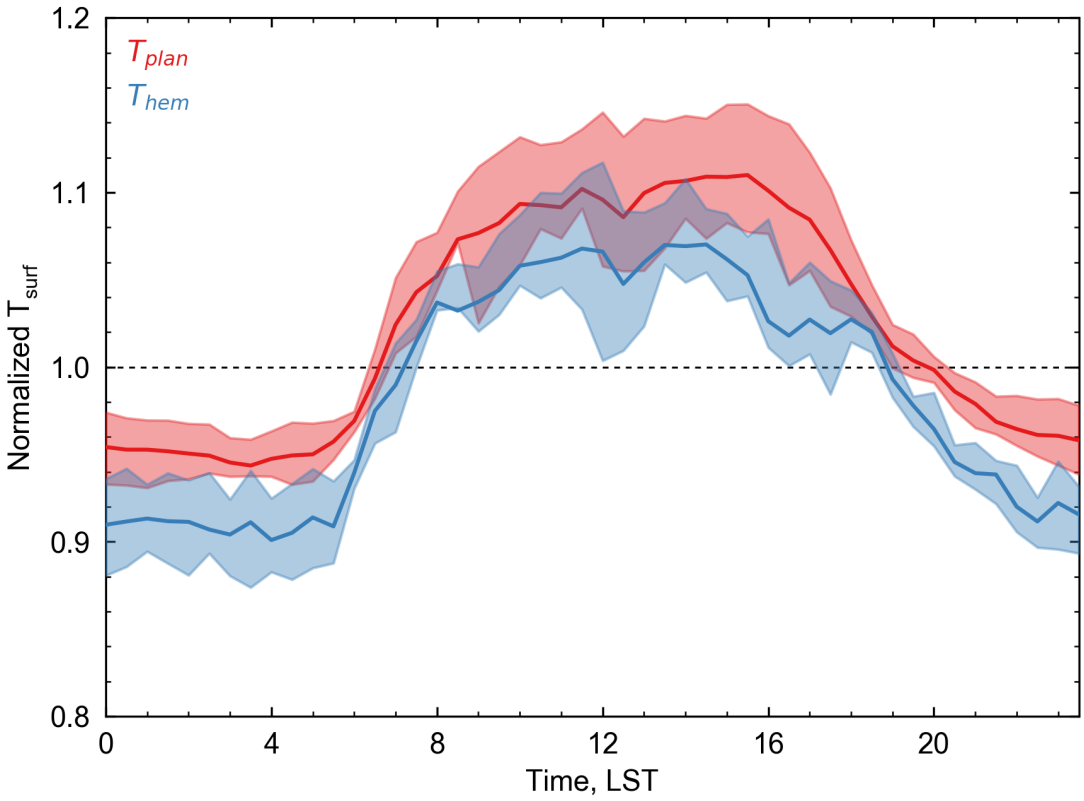

Figure 2.16: A comparison of mean normalized $T_{hem,\,r}$ and T_{plan} at 30 min intervals over the IOP. Shading indicates the area bounded by the first and third quartiles. n = 14

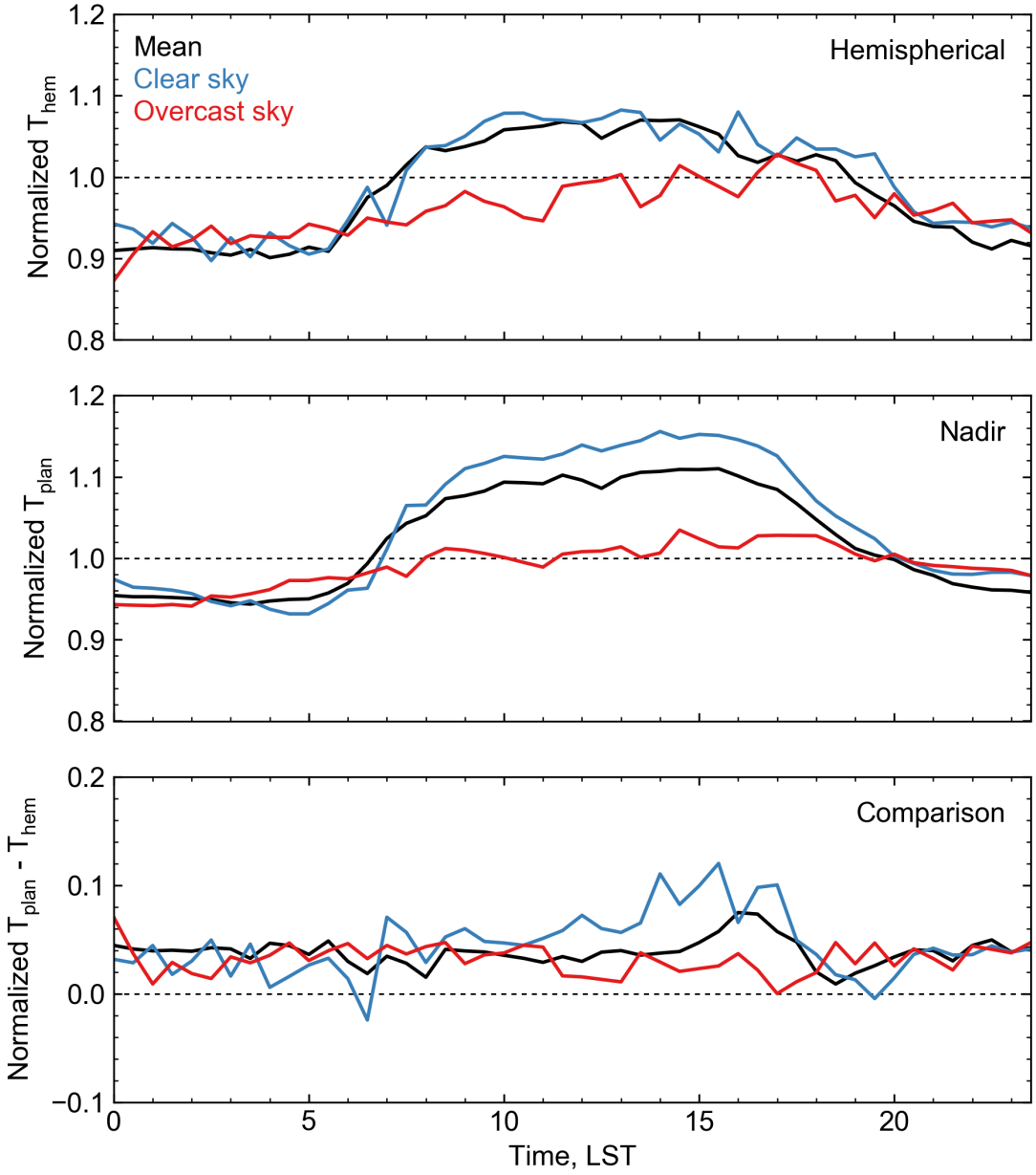

Figure 2.17: Normalized $T_{hem,\,r}$, T_{plan}, and $\Delta T_{plan\,-\,hem,\,r}$ averaged over the IOP and for clear sky and overcast case days. n = 14

2.7 Discussion

2.7.1 Controls on atmospheric correction magnitude

Atmospheric correction magnitudes are highly dependent on factors that control $\Delta T_{surf\ -\ air}$. With a non-zero $\Delta T_{surf\ -\ air}$, TIR radiation emitted from the surface and absorbed by the atmosphere is re-emitted at a different temperature, modifying the at-sensor TIR signal. Thus, the strength of the T_{surf} to T_{air} differential is directly related to the magnitude of atmospheric effects on a remote sensed TIR signal. This results in a strong positive relationship between atmospheric correction magnitude and $\Delta T_{hem,\ r\ -\ air}$. Results in Figures 2.12 - 2.14 show that conditions that maximize microscale surface to atmosphere thermal contrasts result in large correction magnitudes and conditions that suppress differences between T_{surf} and T_{air} show much smaller or negative correction magnitudes.

Of the meteorological variables tested, correction magnitudes are most strongly dependent on solar input. Solar radiation incident on the surface forces microscale thermal contrasts between the surface and the air, directly controlling the T_{surf} - T_{air} differential. The relationships between correction magnitude and $T_{hem,\ r}$ and T_{air} individually are weaker and more complex. Correction magnitudes are smallest when $T_{hem,\ r}$ and T_{air} are between approximately 10 and 20 °C - largely made up of morning and cloudy observations during the summer months where thermal contrasts between T_{surf} and T_{air} are small or weakly negative, forcing small correction magnitudes. During the winter months, a negative relationship between $T_{hem,\ r}$ and T_{air} and correction magnitudes is observed, likely a result of the effect of shifting spectral emittance curves combined with non-uniform sensor response - discussed in section 2.7.2. On clear sky summer days, positive relationships between correction magnitudes and $T_{hem,\ r}$ and T_{air} are observed as an increased solar input foster higher overall temperatures and

large contrasts between T_{surf} and T_{air}.

Results in Figure 2.10 show significant seasonal and diurnal variation in correction magnitudes. The range of observed correction magnitudes is largest in summer, when a wide range of mid latitude synoptic conditions result in significant contrasts in daytime solar input and consequently large variations in the T_{surf} - T_{air} difference. Maximum correction magnitudes over the study period (often approaching 7 to 8 K) occur frequently near solar noon on clear, hot, humid days, during which intense solar heating of the surface produces a large T_{surf} - T_{air} differential. Minimum correction magnitudes near -1 K occur consistently on clear, calm nights following hot days, when T_{surf} can dip below T_{air}, even in urban areas where canyon trapping of radiation reduces cooling rates for both T_{surf} and T_{air}. In winter, decreased variability in overall solar input results in less intense solar heating of the surface and smaller T_{surf} - T_{air} contrasts. Thus, winter correction magnitudes are smaller and more consistent with a mean of approximately 2 K.

2.7.2 The effect of non-uniform pyrgeometer spectral dome transmittance on correction magnitudes

A pyrgeometer's dome transmittance is spectrally non-uniform. Thus, the "dome effect" a pyrgeometer exerts on a given incoming TIR signal changes as a function of emission temperature (T_{emiss}) because the shape of a given spectral radiance curve (R_ν) is temperature dependent. This is illustrated in Figure 2.18 by comparing the relative peaks and shape of a pyrgeometer dome transmittance curve for several R_ν (T_{emiss}) for a range of typical urban T_{emiss} (T_{emiss} = 260 - 320 K, at 5 K increments). As each curve interacts with a different portion of the spectral dome transmittance curve (r_ν), and r_ν is spectrally non-uniform, the distinct spectral shapes of R_ν results in differential dome effects for each T_{emiss}.

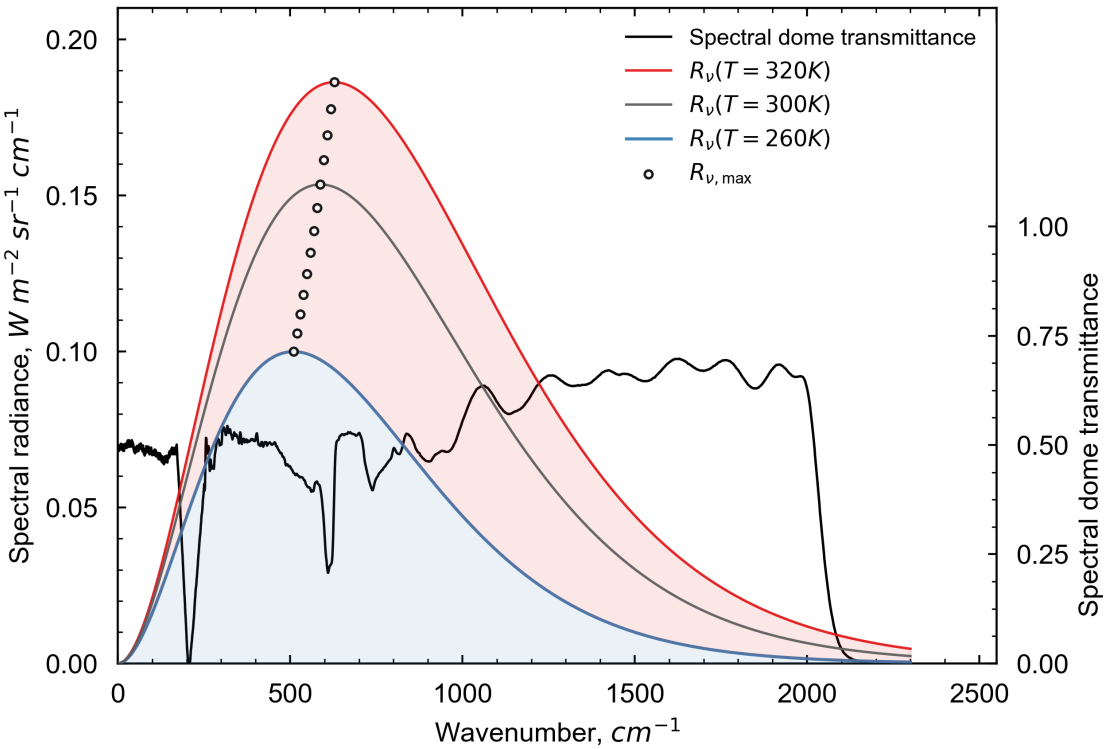

Figure 2.18: Spectral dome transmittance for a Kipp & Zonen pyrgeometer overlaid with a Planckian spectral radiance curve at T = 300 K and the same curve shifted to represent the shape and peak of a spectral radiance curve at T = 270 K.

Spectrally non-uniform pyrgeometer dome transmittance results in differential dome effects on the R_ν for different T_{emiss}. Thus, temperature specific calibration routines designed to remove dome effects and retrieve accurate irradiance values are subject to errors based on the difference between T_{emiss} and the temperature at which the instrument was calibrated (T_{calib}). The magnitude of this error can be expressed as differentials in Planck weighted mean sensor response ($\overline{r}$) calculated via equation 2.9 for different T_{emiss} — where lower $\overline{r}$ indicates a larger dome effect on the signal received by the sensor. In addition, this error can be expressed as a

dome adjusted temperature bias (T_{bias}) computed as the difference between a reference T_{calib} and a dome adjusted temperature (T_{adj}). With R_ν (T_{adj}) representing a spectral curve with the same integrated radiance as R_ν (T_{calib}) shifted to represent the dome effect incurred at the target T_{emiss}. For example, to calculate T_{bias} for T_{emiss} = 270 K at T_{calib} = 300 K, a spectral shift is applied to R_ν (300 K) so that its peak spectral radiance matches the wavenumber of peak spectral emission for R_ν (270 K). When integrated, the two curves have the same radiance, but interact with r over different wavebands. Following the spectral shift, spectral radiances are convolved by the dome transmittance function, integrated over the waveband and hemisphere, and used to derive T_{adj} via equation 2.5 with $\overline{r}$ at T_{calib}.[2] Table 2.3 shows $\overline{r}$ and T_{bias} and for a range of T_{emiss}.

Table 2.3: Planck weighted mean sensor response and T_{bias} for a suite of common urban emission temperatures.

T_{emiss}, K	$\overline{r}$, %	T_{bias}, K computed for T_{calib} = 300 K
260	48.3	-1.67
265	48.5	-1.49
270	48.7	-1.32
275	48.9	-1.13
280	49.1	-0.95
285	49.3	-0.75
290	49.4	-0.56
295	49.6	-0.36
300	49.7	-0.15
305	50.0	0.05
310	50.1	0.26
315	50.3	0.47
320	50.4	0.69

[2] In this sensitivity test, the waveband was truncated from 1 - 2500 cm^{-1} to 80 - 2500 cm^{-1} to accommodate shorter wavenumber when shifting R_ν (T_{calib}) to lower temperatures where peak spectral emission occurs at smaller wavenumber. This results in a slight underestimation of the total radiance at a given T_{emiss}, and thus, slightly negative T_{bias} at T_{calib}, where no spectral shift has been applied. When computed from total in band radiance, T_{bias} at the reference T_{calib} is zero.

The magnitude of T_{bias} increases as the difference between the reference T_{calib} and T_{emiss} increases, with approximately equal rates of change with increasing and decreasing T_{emiss}. Dome effects have a significant effect on the pyrgeometer received signal when comparing irradiances or T_{hem} over a wide range of temperatures, or when T_{emiss} is significantly different from T_{calib}. Pyrgeometers used in the BUBBLE campaign were calibrated outdoors under clear-sky, mid-latitude springtime conditions (Christen and Vogt, 2005). Thus, dome effects inherent in uncorrected L_z measurements in this study are likely smaller in summer than in winter (as T_{emiss} is likely closer to T_{calib} in summer than it is in winter), and are well represented by Table 2.3.

By convolving modeled spectral radiances by a dome transmittance curve, the correction method presented in this study accounts for dome effects. Thus, correction magnitudes include both atmospheric effects and effects from spectrally non-uniform dome transmittance (and, crudely, emissivity effects, as modeled radiances are calculated with $\epsilon = 0.95$ and include a reflected L_{sky} component). While the individual effects are difficult to separate, temperature dependent differential dome effects are visible in correction magnitudes as a persistent minor positive correction in winter. Relative to T_{calib}, lower T_{emiss} in winter results in a larger dome effects. This manifests in artificially low $T_{hem,\,b}$ and increased wintertime correction magnitudes.

Additionally, modeled irradiances include a reflected downwelling component, which, although small, is sensitive to T_{air} and humidity profiles above the sensor height. Because these data were not consistently measured, mid-latitude summer and winter standard atmospheric profiles supplemented the measured data. The climate of Basel is characterized by mild, humid winters (Köppen classification: Cfb). As a result, above-sensor T_{air} and humidity values are likely underestimated by the standard wintertime atmosphere, reducing the modeled at-sensor reflected component of downwelling longwave in winter and the overall modeled at-sensor signal. This results in an increase in derived $T_{hem,\,r}$ and correction magnitudes as measured

irradiances are matched with irradiances modeled at slightly higher T_{surf} to make up for the underestimated at-sensor L_{sky} signal.

2.7.3 The effect of sensor sampling geometry on remote sensed T_{surf}

Results in Figures 2.16 and 2.17 show that sensor sampling regimes can have a significant effect on remote sensed T_{surf}. Both $T_{hem,\,r}$ and T_{plan} overestimate T_{comp} by day and underestimate T_{comp} by night. These results are consistent with findings in Voogt and Oke (2003) and Adderley et al. (2015). However, when analyzed over a time series, over/underestimations from geometric effects are highly dependent on synoptic conditions, particularly for a nadir view of the urban surface. T_{plan} is much greater than T_{comp} under clear sky conditions, with $T_{hem,\,r}$ showing a much smaller positive bias. Over half of the T_{plan} signal from the Sperrstrasse canyon is generated by rooftops that have both a large diurnal T_{surf} amplitude and the highest daytime facet T_{max}. Undersampling of sloped facets and neglect of wall facets by T_{plan} also has a significant effect on the daytime clear-sky warming bias, as walls show much cooler daytime T_{max} than T_{roof} or T_{road} and have a moderating effect on T_{comp} and $T_{hem,\,r}$ by day, particularly on hot clear sky days. Mean daytime overestimations by T_{plan} just after solar noon are approximately 4 K over the IOP, approaching 8 K on the clear sky case day. $T_{hem,\,r}$ shows smaller overestimations of approximately 3 K over the IOP and 5 K on the clear sky case day. Urban T_{surf} and the sUHI are often measured from satellite remote sensors that retrieve T_{plan} exclusively under clear-sky conditions and often sample in the nadir. Thus, overestimation of daytime urban T_{comp} inherent in the satellite T_{surf} record is best represented by T_{plan} on the clear sky case day.

Nighttime underestimations of T_{comp} by nadir and hemispherical views are a result of an undersampling of wall and road facets respectively Roth et al. (1989). $T_{hem,\,r}$ derived from L_z measured at the Sperrstrasse canyon oversamples the nearest roof and underestimates the

canyon floor compared to T_{comp} as its location along the canyon axis is skewed towards the south facing wall (rather than the center of the canyon) and its height is approximately 2.17 times mean building height. Sub-optimal sensor placement in the Sperrstrasse canyon - discussed in section 2.8 results in a large underestimation of nighttime T_{comp} by $T_{hem,\,r}$. However, nighttime underestimation — and to some extent, daytime overestimation — by $T_{hem,\,r}$ is the combined result of a sampling bias inherent in a hemispherical view of the surface and improper sensor placement. Both of these biases can likely be reduced significantly by adjusting sensor placement to best represent surface geometry.

2.8 Sensor placement sensitivity testing

When measured from a near ground downward facing pyrgeometer, upwelling TIR radiation is sensitive to sensor height and position relative to surface geometry (Adderley et al., 2015; Roberts, 2010). Below 3 times mean roof level, measured TIR radiation varies from a ”true”, geometrically representative, TIR signal based on a comparison between facet view factor proportions of the sensor and those of the urban surface. A perfectly geometrically representative remote sensed TIR signal is one measured from a sensor with facet view factor proportions equaling those of the urban surface. I.e. for an urban surface made up of 50% wall, 25% road, and 25% roof, a perfectly geometrically representative remote sensed signal would be one ”seen” by a sensor with the same fractional facet view factor proportions. For an idealized, orthogonal, block-like urban array, Roberts (2010) found that facet view factor proportions — and thus measured TIR radiation — varied significantly with sensor position and height. To investigate the effect of sensor placement on $T_{hem,\,r}$ for a simplified representation of the Sperrstrasse canyon site, we used SUM to vary sensor position over a simplified DBM and calculate normalized view factor proportions for a 160° FOV sensor. For nine sensor positions,

show in Figure 2.19, facet view factor proportions normalized to unity are shown in Figure 2.20 for a sensor height of 2.17 times mean building height and in Figure 2.21 for a sensor height of 3 times mean building height. Approximated actual facet surface area proportions for the Sperrstrasse canyon are included for reference. A fully geometrically representative sensor viewing the urban surface would have facet view factor proportions equal to actual facet surface area proportions.

Normalized facet view factors in Figures 2.22 and 2.23 show large variations based on sensor position at both test heights. At the lower test height, varying sensor position perpendicular to the canyon axis, positions at the canyon center (positions 4, 5, and 6) are most representative of actual facet view factors, with decreasing representivity at the edge of the canyon (positions 1, 2, and 3), and over the rooftops (positions 7, 8, and 9). Moving the sensor parallel to the canyon axis, positions slightly offset from the roof edge (positions 2, 5, and 8) agree most closely with actual canyon surface area proportions, with decreasing representivity in positions further from the roof edge. Roof and road view factor proportions are most strongly affected by sensor placement. Positions directly over buildings show large biases towards roof view factors and positions in the center of the canyon showing slight biases towards road facets. In all positions roof view factor was overestimated (save position 4), and wall view factor was underestimated.

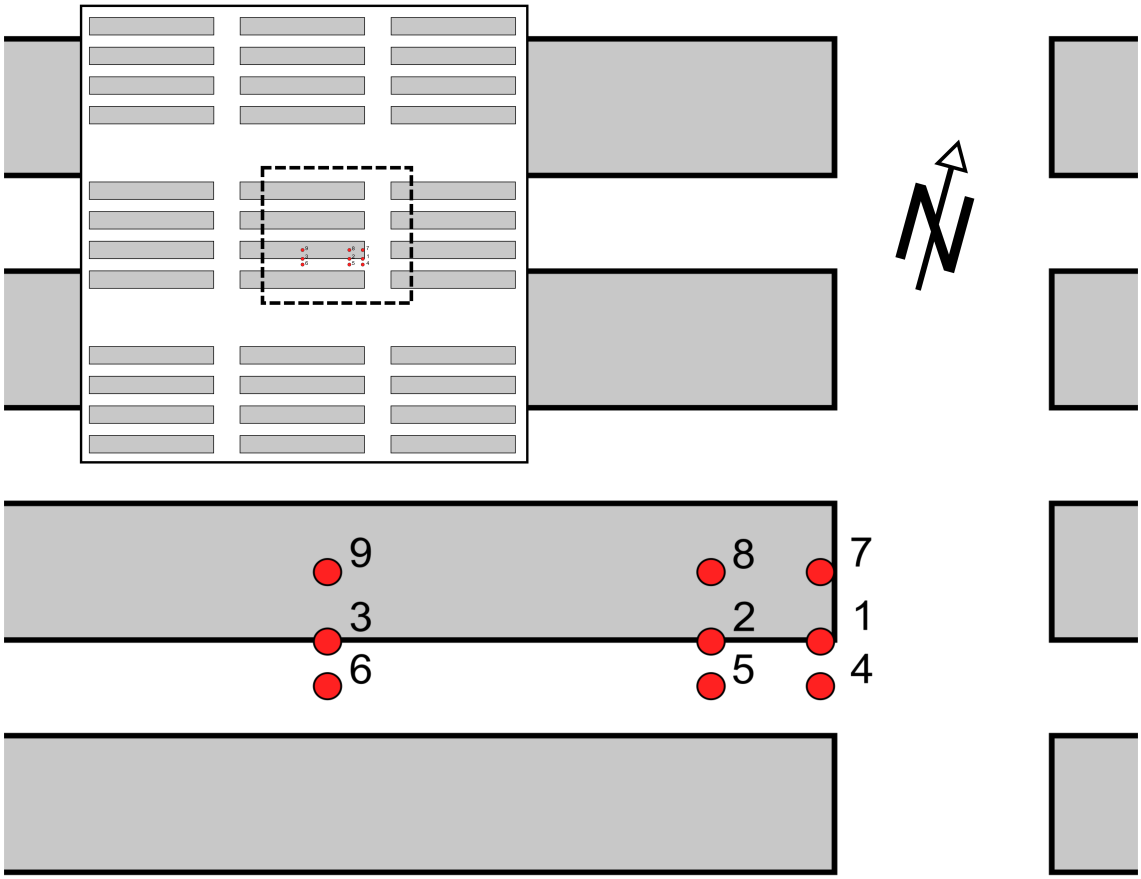

Figure 2.19: A plan view of the simplified DBM showing the nine test sensor placements. Actual sensor placement at the Sperrstrasse canyon is approximated by number 3.

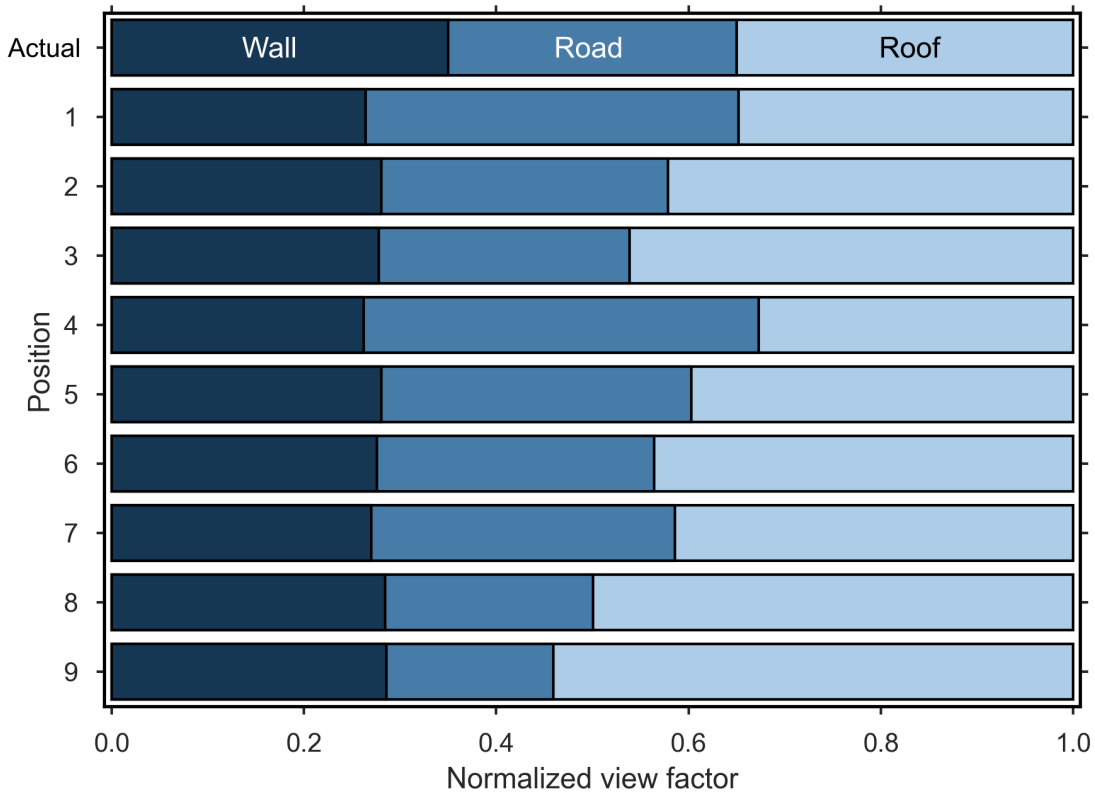

Figure 2.20: Normalized wall, road, and roof view factors for nine sensor positions viewing the simplified street canyon array from 2.17 times mean building height. Actual normalized view factors refer to surface area proportions for the three facet types in the Sperrstrasse street canyon.

Results in Adderley et al. (2015) and Roberts (2010) show that sensitivity to sensor placement decreases as sensor height increases. Depending on surface geometry, sensor view factor proportions and the TIR signal "seen" by a sensor become spatially invariant at heights above approximately 3 to 5 times mean building height. Results from the higher sensor test height support findings in Adderley et al. (2015) and Roberts (2010), with decreased spatial variance in facet view factor proportions across the nine sensor positions. However increased spatial stability in view factor proportions does not necessarily entail increased geometric

representivity. For all sensor placements, road view factor proportion is increased and wall view factor is reduced. This results in large overestimations of road view factor for nearly all positions except positions 3 and 9, which include a large overestimation of roof view factor. Thus, although increasing sensor height does reduce spatial variance, it can lead to decreased representivity for some positions - in this case, positions 1 and 4.

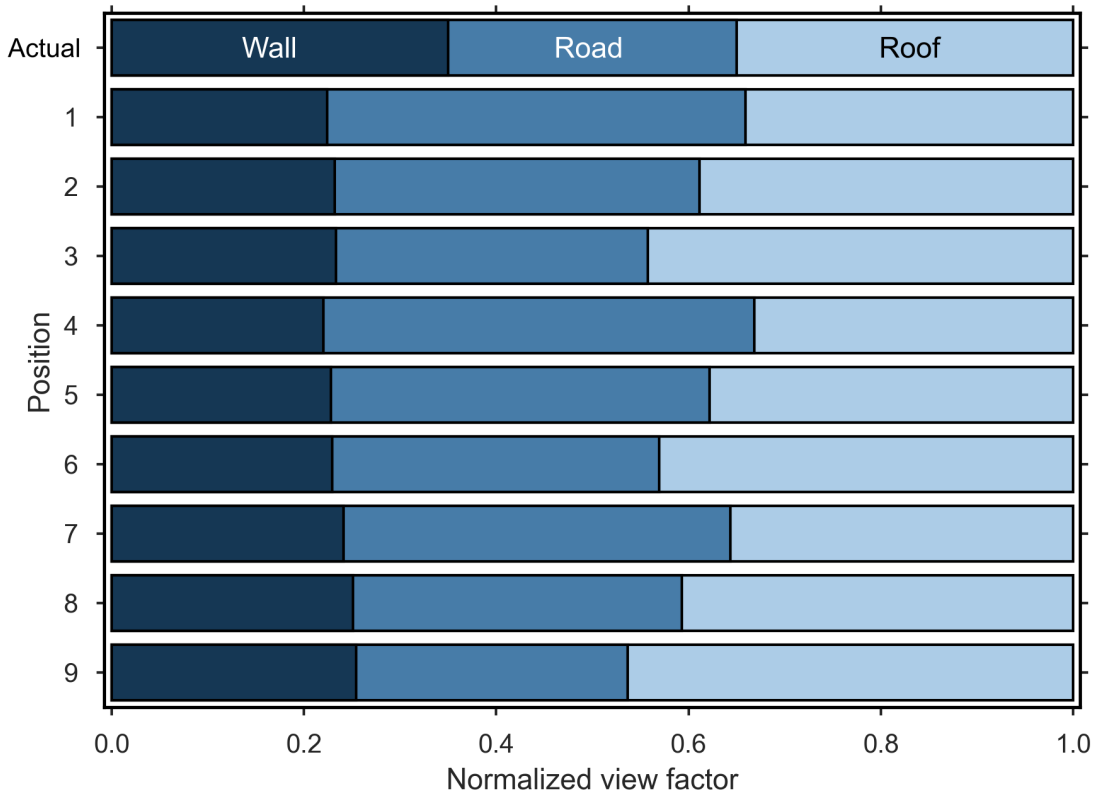

Figure 2.21: Normalized wall, road, and roof view factors for nine sensor positions viewing the simplified street canyon array from 3 times mean building height. Actual normalized view factors refer to surface area proportions for the three facet types in the Sperrstrasse street canyon.

To visualize how sensor placement affects $T_{hem,\,r}$ retrieved via the method detailed in this study, $T_{hem,\,r}$ is inferred using wall, roof, and road view factors calculated in SUM for the two

sensor heights to compute a weighted average of T_{wall}, T_{road}, and T_{roof} for each sensor position at 30 minute intervals over the IOP. Temperatures are normalized by T_{comp} and averaged at each time step over the IOP, the results of which are shown in Figures 2.22 and 2.23. As is the case with view factor proportions, $T_{hem,\,r}$ is highly dependent on sensor placement. For the lower sensor height, as predicted by view factor proportions, positions at the center of the canyon (positions 4, 5, and 6) and edge of the building (positions 1, 4, and 7) follow T_{comp} most closely. By day, all sensor positions overestimate T_{comp}, from a systemic bias towards rooftop facets. The degree of overestimation is largely determined by rooftop view factor, with larger overestimations coming from positions most biased towards hot rooftop surfaces. At night, most sensor positions (save position 4) underestimate T_{comp}, again from a bias towards cool rooftop facets. Position 4 weakly overestimates nighttime T_{comp}, from a slight view factor bias towards road facets with suppressed nocturnal cooling from canyon radiation trapping.

At the higher test height, $T_{hem,\,r}$ is more representative of T_{comp} for positions 2, 3, and 5 - 9. $T_{hem,\,r}$ from positions 1 and 4 display a slight systematic overestimation of T_{comp}. For these positions, although roof view factor proportion is well represented, road view factor is significantly overestimated, oversampling warmer nighttime road temperatures. For all other positions, daytime overestimation and nighttime underestimation of T_{comp} is reduced. Thus, as is the case with view factor proportions, at the higher test height, $T_{hem,\,r}$ is more spatially stable.

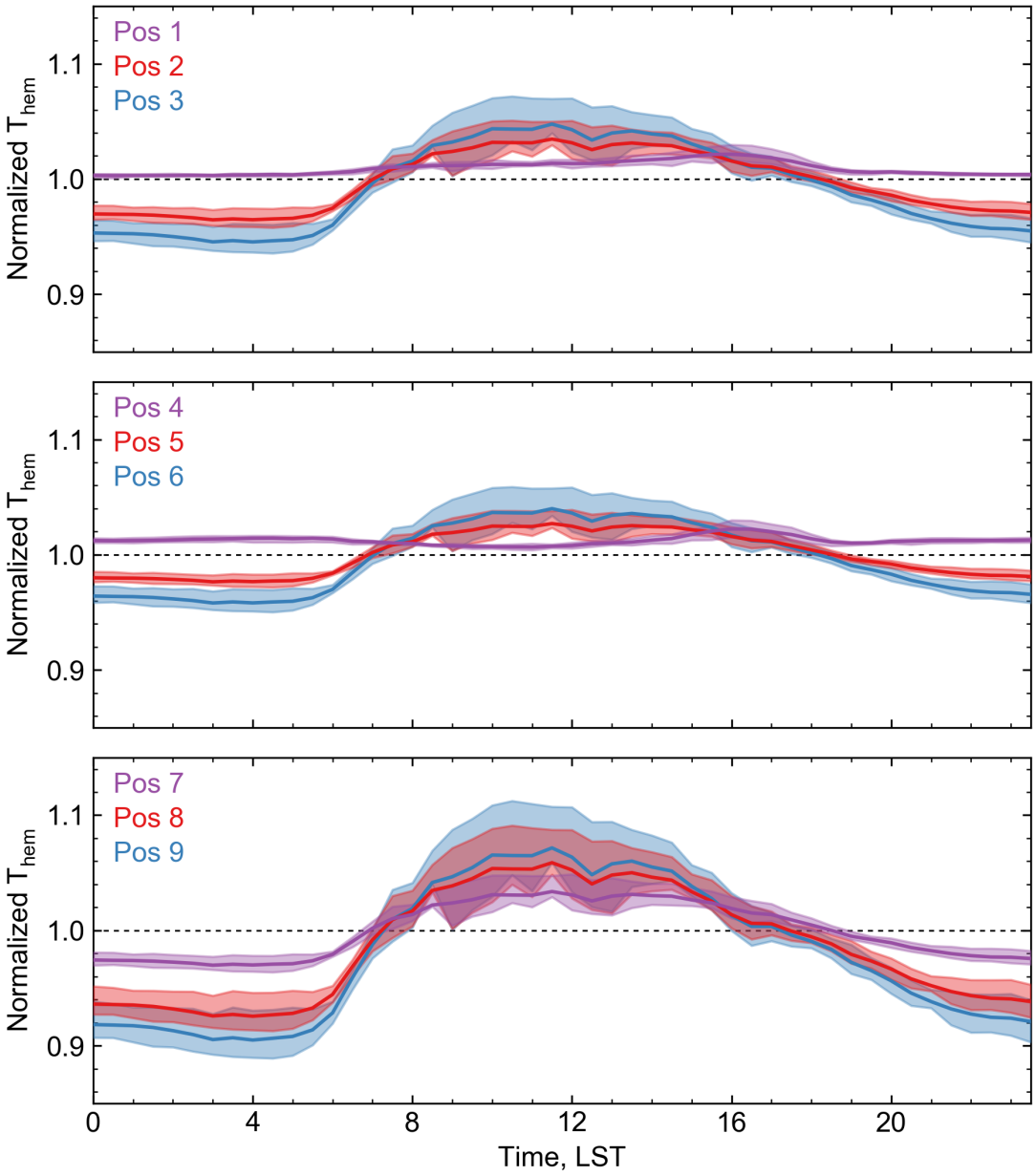

Figure 2.22: Mean $T_{hem,\,r}$ normalized against T_{comp} for each sensor position over the 14-day IOP for a sensor height of 2.17 times mean building height. Shaded area indicates quartiles one through three.

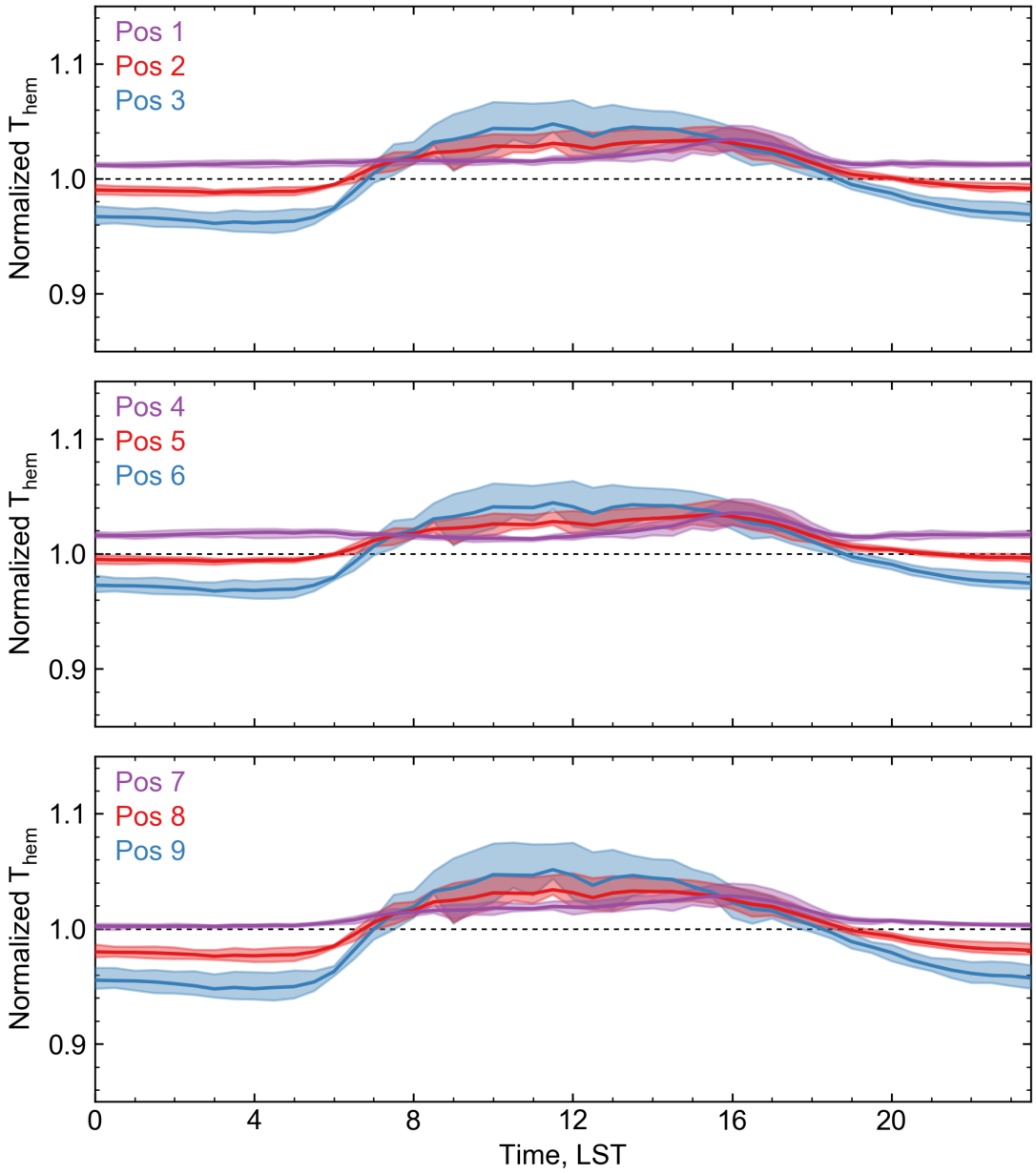

Figure 2.23: Mean $T_{hem,\,r}$ normalized against T_{comp} for each sensor position over the 14-day IOP for a sensor height of 3 times mean building height. Shaded area indicates quartiles one through three.

Both Roberts (2010) and Adderley et al. (2015) did not find a perfectly representative sensor position for typical low- and mid-rise urban street canyons; this is supported by sensitivity testing performed in this study. As such, under conditions with strong microscale spatial contrasts in T_{surf}, $T_{hem,\,r}$ is unlikely to be equal T_{comp} regardless of sensor placement. However, sensor view models, such as SUM, can be used to optimize sensor placement with information about surface geometry to retrieve the most accurate measured irradiances and derived $T_{hem,\,r}$ for a given surface geometry.

2.9 A practical parameterization

To save computational time and facilitate broader use of the method, a parameterization scheme was developed to simplify the correction process. In the parameterization, a suite of radiative transfer simulations is run prior to correction (as opposed to at each time step) to retrieve transmittances (τ) for a range of humidities and path lengths. T_{surf} and T_{air} are held constant in these simulations as they have a relatively small effect on τ. Simulations for path lengths from 1 to 48 m and water vapor mass densities from 0.1 to 23.5 $\mathrm{g\,m^{-3}}$ are included in Appendix A. Sensor-surface geometry is approximated as a single view factor weighted, azimuthally averaged, surface-to-sensor path length calculated using the SUM (Soux et al., 2004) and a simplified DBM. This path length represents the average distance from the sensor to the surface as "seen" by the sensor. For each time step, measured humidity is used to infer a hemispherical transmittance ($\overline{\tau_\Phi}$) for the approximated surface-sensor geometry. A parameterized $T_{hem,\,r}$ can then be calculated by using measured (in this case, profile averaged) T_{air} to decompose measured upwelling longwave into irradiance received by the sensor from the surface $L_{surf}^{at-sensor}$ and from the atmosphere $L_{atm}^{at-sensor}$ via,

$$T_{hem,\,r} = \left(\frac{\left(\frac{L_{surf}^{at-sensor}}{\tau} \right)}{\sigma} \right)^{0.25} \tag{2.11}$$

where τ is calculated using a radiative transfer code and $L_{surf}^{at-sensor}$ is an estimation of the fraction of at sensor measured irradiance emitted by the surface calculated as,

$$L_{surf}^{at-sensor} = L_{total}^{at-sensor} - (1-\tau)\sigma T_{air}^{4} \tag{2.12}$$

Using this parameterization, a climatology of $T_{hem,\,r}$ for a given surface geometry can be retrieved from approximately 100 simulations as opposed to the many thousands needed for full hemispherical radiative transfer simulation. A variety of online and offline, open and closed source resources are available for radiative transfer simulation (Gastellu-Etchegorry et al., 1996; Berk et al., 1987; Buehler et al., 2005), some of which are available for free or at a low cost (e.g. Spectral-Calc, DART), all of which are likely to provide similar transmittances to those included in Appendix A. Figure 2.24 and Table 2.4 summarize parameterization performance relative to $T_{hem,\,r}$ retrieved via the correction method. Errors are largest during the daytime hours, where the profile averaged T_{air} overestimates above canyon T_{air} and underestimates near-surface T_{air}. Neutral stability in the nighttime and early morning hours reduces these errors significantly as the canyon T_{air} profile is approximately isothermal.

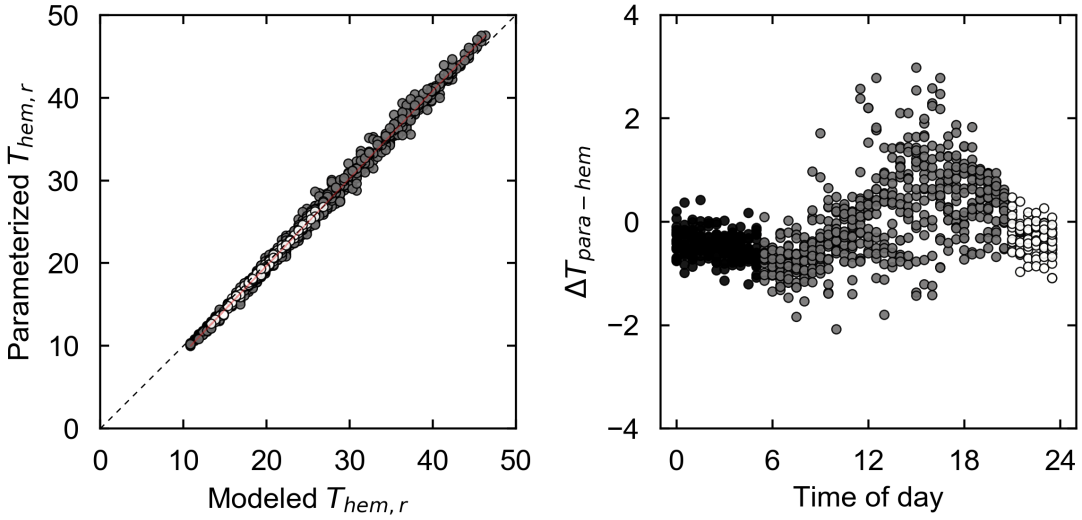

Figure 2.24: Modeled $T_{hem,\,r}$ versus $T_{hem,\,r}$ derived via the parameterization scheme.

Table 2.4: Statistical performance of T_{hem} derived using the parameterization scheme relative to modeled $T_{hem,r}$. $RMSE_s$ and $RMSE_u$ represent the systemic and unsystematic RMSE respectively. The arrangement of statistical tests were selected from Willmott et al. (1985) and Willmott et al. (2012). n = 853

Statistic	Parameterization
Slope	1.058
Intercept, (K)	-1.488
R^2	0.991
MAE, (K)	0.607
RMSE, (K)	0.757
$RMSE_s$, (K)	0.476
$RMSE_u$, (K)	0.588
d, agreement index	0.998

2.10 Conclusions

Accurate, geometrically representative, spatially extensive, and temporally continuous thermal remote sensing of complex terrain (urban or otherwise) is difficult. It is unlikely that a single sensor will satisfy spatial, geometric, and temporal goals. Thus, a combination of satellite, aerial, and in-situ observational methods has been integral in isolating and elucidating the urban effect on surface temperature and its spatial, temporal, and geometric characteristics. However, neither technological advancement nor critical analysis of these methods has provided a satisfactory answer to the questions posed in Roth et al. (1989) viz urban thermal remote sensing. As such, the true spatial, temporal, and geometric nature of the urban effect on surface temperature remains unknown.

This paper details a method for urban T_{surf} retrieval using atmospherically corrected hemispherical radiometric surface temperatures derived from continuous near-ground measurements of thermal infrared radiation. Atmospherically corrected, hemispherical urban T_{surf} is derived using a method which combines a sensor view model (SUM) to represent urban surface geometry and a point-to-point radiative transfer code (MODTRAN 4.1) to model irradiances upwelling from complex surface terrain in 3-dimensions. At each time step, irradiances are modeled using profiles of T_{air} and water vapor content for a range of possible $T_{hem,\,r}$. Irradiance - $T_{hem,\,r}$ pairings are aggregated into a LUT and the measured irradiance is matched with the closest modeled irradiance to retrieve $T_{hem,\,r}$ for a given time step. Repeated at 30-minute intervals, the method is used to derive an 8-month climatology of urban $T_{hem,\,r}$ from urban irradiances measured as a part of the BUBBLE campaign in Basel, Switzerland.

Atmospheric corrections are large and vary significantly based on sensor-surface-sun geometry and synoptic conditions. Thus, T_{hem} derived from irradiances measured at different heights or above different surface geometries may have different atmospheric or dome effects

that can confound results. This fact makes clear the need for robust atmospheric correction of T_{hem} for sUHI analysis or to retrieve radiometric T_{hem}. Correction magnitudes are largest on hot, clear sky summertime days — with large solar input and high T_{surf} and T_{air} — and smallest by night and under overcast conditions, during which solar input is suppressed and T_{surf} and T_{air} are low. Correction magnitudes are most strongly correlated with the T_{surf} to T_{air} differential and incoming solar radiation and weakly correlated with $T_{hem, r}$ and T_{air}. Water vapor content did not appear to exert strong control over correction magnitudes.

Comparison of T_{surf} from nadir, hemispherical, and complete representations of the Basel Sperrstrasse street canyon show that a hemispherical view is more geometrically representative of the complete surface temperature than a sensor viewing in the nadir. However, sensor placement sensitivity tests show that $T_{hem, r}$ varies based on sensor placement and height. Overestimations of T_{comp} by T_{plan} and $T_{hem, r}$ are greatest under clear sky conditions and are much larger for T_{plan}. This is particularly important when one considers that satellite observations of urban T_{surf} are only possible under clear sky conditions (when T_{plan} is least representative of T_{comp}). Significant variability in over/underestimation of T_{comp} by $T_{hem, r}$ and T_{plan} based on time of day and synoptic conditions make these biases difficult to generalize to other urban study sites with different surface geometries and characteristics, canyon orientations, and macro climates. However, the measures used to derive $T_{hem, r}$ are common to most energy balance assessments and constitute an untapped, but promising, resource to improve understanding of how the built environment affects land T_{surf} and to quantify the geometric and temporal biases inherent in satellite remote sensing of TIR radiation emitted from complex terrain.

References

Adderley, C., Christen, A., and Voogt, J. A. (2015). The effect of radiometer placement and view on inferred directional and hemispheric radiometric temperatures of an urban canopy. *Atmospheric Measurement Techniques*, 8(2):1891–1933.

Bastiaanssen W. G. M., M. Meneti, R.A. Feddes, and Holtslag, A. A. M. (1998). A remote sensing surface energy balance algorithm for land (SEBAL): Formulation. *Journal of Hydrology*, 212-213:198–212.

Berk, A., Bernstein, L. S., and Robertson, D. C. (1987). MODTRAN: A Moderate Resolution Model for LOWTRAN7. Technical Report GL-TR-89-0122, United States Air Force.

Buehler, S. A., Eriksson, P., Kuhn, T., von Engeln, A., and Verdes, C. (2005). ARTS, the atmospheric radiative transfer simulator. *Journal of Quantitative Spectroscopy and Radiative Transfer*, 91(1):65–93.

Christen, A. and Vogt, R. (2005). Quality control and corrections of the radiation measurements at the BUBBLE-surface sites. Technical report, University of Basel.

Cooper, D. I. and Asrar, G. (1989). Evaluating atmospheric correction models for retrieving surface temperatures from the AVHRR over a tallgrass prairie. *Remote Sensing of Environment*, 27(1):93–102.

Frey, C. M., Rigo, G., and Parlow, E. (2007). Urban radiation balance of two coastal cities in a hot and dry environment. *International Journal of Remote Sensing*, 28(789273183):2695–2712.

Gastellu-Etchegorry, J. P., Demarez, V., Pinel, V., and Zagolski, F. (1996). Modeling radiative transfer in heterogeneous 3-D vegetation canopies. *Remote Sensing of Environment*, 58(November 1995):131–156.

Hoch, S. (2005). *Radiative flux divergence in the surface boundary layer from observational and model perspectives*. PhD thesis, ETH Zurich.

Hoch, S., Calanca, P., Philipona, R., and Ohmura, A. (2007). Year-round observation of longwave radiative flux divergence in Greenland. *Journal of Applied Meteorology and Climatology*, 46(9):1469–1479.

Kantor, A. J. and Cole, A. E. (1962). Mid-latitude atmospheres, winter and summer. *Geofisica Pura e Applicata*, 53(1):171–188.

Kneizys, F. X., Anderson, G. P., Shettle, E. P., Gallery, W. O., Abreu, L. W., Selby, J. E. A., Chetwynd, J. H., and Clough, S. A. (1988). Users guide to LOWTRAN 7. Technical Report AFGL-TR-88-0177, Air Force Geophys. Lab., Bedford, Mass.

Kotani, A. and Sugita, M. (2009). Concise formulae for the atmospheric correction of hemispherical thermal radiation measured near the ground surface. *Water Resources Research*, 45(7):1–7.

Meier, F., Scherer, D., Richters, J., and Christen, A. (2011). Atmospheric correction of thermal-infrared imagery of the 3-D urban environment acquired in oblique viewing geometry. *Atmospheric Measurement Techniques*, 4(5):909–922.

Miskolczi, F. and Guzzi, R. (1993). Effect of nonuniform spectral dome transmittance on the accuracy of infrared radiation measurements using shielded pyrradiometers and pyrgeometers. *Applied Optics*, 32(18):3257.

Nakamura, Y. and Oke, T. R. (1988). Wind, temperature and stability conditions in an east-west oriented urban canyon. *Atmospheric Environment (1967)*, 22(12):2691–2700.

Norman, J. M. and Becker, F. (1995). Terminology in thermal infrared remote sensing of natural surfaces. *Agricultural and Forest Meteorology*, 77(3-4):153–166.

Oke, T. R. (1987). *Boundary Layer Climates*. Routledge Books.

Peng, S., Piao, S., Ciais, P., Friedlingstein, P., Ottle, C., Bréon, F. M., Nan, H., Zhou, L., and Myneni, R. B. (2012). Surface urban heat island across 419 global big cities. *Environmental Science and Technology*, 46(2):696–703.

Qin, Z., Karnieli, A., and Berliner, P. (2001). A mono-window algorithm for retrieving land surface temperature from Landsat TM data and its application to the Israel-Egypt border region. *International Journal of Remote Sensing*, 22(18):3719–3746.

Roberts, S. (2010). *Three-dimensional radiation flux source areas in urban areas*. PhD thesis, University of British Columbia.

Rotach, M. W., Vogt, R., Bernhofer, C., Batchvarova, E., Christen, A., Clappier, A., Feddersen, B., Gryning, S.-E., Martucci, G., Mayer, H., Mitev, V., Oke, T. R., Parlow, E., Richner, H., Roth, M., Roulet, Y.-A., Ruffieux, D., Salmond, J. A., Schatzmann, M., and Voogt, J. A. (2005). BUBBLE an Urban Boundary Layer Meteorology Project. *Theoretical and Applied Climatology*, 81(3-4):231–261.

Roth, M., Oke, T. R., and Emery, W. (1989). Satellite-derived urban heat islands from three coastal cities and the utilization of such data in urban climatology. *International Journal of Remote Sensing*, 10(11):1699–1720.

Soux, A., Voogt, J. A., and Oke, T. R. (2004). A model to calculate what a remote sensor 'sees' of an urban surface. *Boundary-Layer Meteorology*, 111(1):109–132.

Stewart, I. D. and Oke, T. R. (2012). Local climate zones for urban temperature studies. *Bulletin of the American Meteorological Society*, 93(12):1879–1900.

Stoll, M. J. and Brazel, A. J. (1992). Surface-air temperature relationship in the urban environment of Phoenix, Arizona. *Physical Geography*, 13(2):160–179.

Voogt, J. A. and Oke, T. R. (1997). Complete urban surface temperatures. *Journal of Applied Meteorology*, 36(9):1117–1132.

Voogt, J. A. and Oke, T. R. (1998). Effects of urban surface geometry on remotely-sensed surface temperature. *International Journal of Remote Sensing*, 19(February 2015):895–920.

Voogt, J. A. and Oke, T. R. (2003). Thermal remote sensing of urban climates. *Remote Sensing of Environment*, 86(3):370–384.

Wan, Z. and Dozier, J. (1996). A generalized split-window algorithm for retrieving land-surface temperature from space. *IEEE Transactions of Geoscience and Remote Sensing*, 34(4):892–905.

Willmott, C. J., Ackleson, S. G., Davis, R. E., Feddema, J. J., Klink, K. M., Legates, D. R., O'Donnell, J., and Rowe, C. M. (1985). Statistics for the evaluation and comparison of models. *Journal of Geophysical Research*, 90(C5):8995.

Willmott, C. J., Robeson, S. M., and Matsuura, K. (2012). A refined index of model performance. *International Journal of Climatology*, 32(13):2088–2094.

Yamaguchi, Y. and Kato, S. (2005). Analysis of urban heat-island effect using ASTER and ETM+ Data: Separation of anthropogenic heat discharge and natural heat radiation from sensible heat flux. *Remote Sensing of Environment*, 99:44–54.

Chapter 3

A climatology of sUHI derived from hemispherical radiometric surface temperatures

3.1 Introduction

The temperature of the surface is integral in understanding, predicting, and modeling boundary-layer air temperature patterns, surface energy balances, and, in urban areas, has important implications for human thermal comfort and building energy usage. Urban modification of surface geometry and thermal, radiative, moisture, and aerodynamic properties results in differential surface heating and cooling patterns and strong microscale spatiotemporal variations in urban surface temperature. Integrated up to larger scales, urban areas tend to store more heat relative to non-built surroundings; and traffic, HVAC systems, and industrial processes contribute to an additional anthropogenic heat input. In addition, a reduced pervious

(and vegetative) cover in urban areas shifts convective fluxes towards sensible heat and away from latent heat. These manifest in elevated T_{surf} and T_{air} in cities, a phenomenon termed the urban heat island effect. To foster a more complete understanding of the effect of urban areas on climates across a range of scales, accurate, spatiotemporally continuous and geometrically representative characterization of T_{surf} in cities has long been a goal in urban climatology. The proliferation of satellite and aerial thermal remote sensing has enabled spatially-extensive characterizations of surface climates at ever improving spatial and spectral resolutions. Such campaigns have elucidated urban T_{surf} and surface urban heat island patterns globally at large spatial scales (Peng et al., 2012; Zhao et al., 2014). However, technological improvements in remote sensing of TIR radiation have yet to address three potential sources of error that arise when applied in urban areas:

1. Geometric undersampling of 3-dimensional surface structure (Roth et al., 1989)
2. Satellite overpass cycles and sensor sampling regimes that result in temporal discontinuity of the surface temperature time series (Weng and Fu, 2014; Freitas et al., 2013)
3. Clear-sky bias that contributes to an overestimation of ”all-sky” surface temperatures

These biases present a potentially significant source of error by failing to capture micro-scale temporal and geometric variations in urban T_{surf} and sUHI.

Inter-site comparison is the crux of UHI analysis, thus it is imperative that urban T_{surf} measurements are representative of coherent urban patches and free from confounding influences (e.g. atmospheric and emissivity effects). Meta-analysis of the aUHI literature shows that these goals are rarely satisfied (Stewart, 2011). Given the relative difficulty in retrieving accurate, representative urban T_{surf}, similar conclusions are likely for sUHI analysis. In spite of this fact, and the short period over which large-scale, generalizable methods for measuring

urban T_{surf} have been available, study of sUHI via remote sensing of TIR radiation has expanded significantly in the last twenty years (Peng et al., 2012; Voogt and Oke, 2003). To improve,

3.1.1 Bias in thermal remote sensing

Geometric biases in thermal remote sensing of urban areas are a result of its 3-dimensional, convoluted structure and urban modifications to surface materials. Compared to flat, non-urban terrain, urban areas have altered surface geometry and thermal, radiative, aerodynamic, and moisture properties, these change how the urban surface receives and reflects incoming solar radiation and how it emits longwave radiation. The resulting microscale spatiotemporal contrasts in urban T_{surf} create a directional dependence in observed urban T_{surf} when measured from conventional narrow-FOV remote sensing platforms. Thus, remote sensed urban T_{surf} varies based on sensor FOV, viewing angle and direction, and sun-surface geometry. This directional dependence of urban surface temperature is termed "effective thermal anisotropy" (Voogt and Oke, 1998). Traditional satellite or airborne remote sensing platforms, by viewing the surface in the nadir, sample only a fraction of the complete urban surface, leading to spatiotemporally variant directional biases in remote sensed urban T_{surf} of up to 10 to 12 K (Voogt, 1995; Lagouarde et al., 2012). In general, geometric undersampling by a remote sensor in the nadir manifests as an overestimation of daytime T_{surf} and an underestimation of nighttime T_{surf} (Adderley et al., 2015). However, the magnitude and diurnal and seasonal behaviors of this bias are dependent on sensor viewing geometry and unique site characteristics (canyon height-to-width ratio, canyon orientation and materials, vegetation coverage, etc.). Thus, parameterization schemes to account for urban effective anisotropy are difficult to generalize across urban sites, sensor types, and sensor-surface geometries.

In addition to undersampling the urban surface, most thermal remote sensing platforms

yield an instantaneous snap-shot and cannot characterize time-continuous T_{surf} patterns without sacrificing ground resolution. Temporal discontinuities in thermal remote sensing result in myriad potential sources of bias over a wide range of time scales. Aerial and satellite thermal remote sensing require clear sky conditions (clouds are opaque with respect to thermal infrared radiation). Hence, long term satellite characterizations of sUHI are biased towards conditions that maximize urban-rural contrasts in T_{surf}. This likely results in an overestimation of all-sky sUHI.

At diurnal scales, satellite overpass cycles rarely coincide with sUHI maximums and are not standard across cities or platforms. Thus, analysis of satellite remote sensed sUHI is temporally sparse and comparison across instrument platforms is difficult. Work in Zakšek and Oštir (2012), Weng and Fu (2014), and Freitas et al. (2013) use a time series of downscaled thermal images from geostationary satellites to overcome diurnal and seasonal gaps in the urban T_{surf} record for sUHI analysis. However, this work is still subject to clear sky bias and has a coarse spatial resolution. Similar work in Huang et al. (2016) used an annual temperature cycle to interpolate a climatology of remote sensed sUHI from discontinuous remote sensed thermal images, but is limited to clear-sky ”ideal” conditions. Indeed, studies such as these that seek to address diurnal and seasonal gaps in the remote sensed urban T_{surf} record are not the norm. The vast majority of our understanding of sUHI and urban T_{surf} remains temporally discontinuous.

At shorter time scales still, time-continuous analysis of urban T_{surf} shows significant microscale (second to minute) fluctuations in temperature (Christen et al., 2012). Most thermal remote sensors provide instantaneous T_{surf} (rather than temporally averaged) and are potentially contaminated by high-frequency microscale fluctuations in urban T_{surf}. This is particularly salient in urban environments, where a large variety of fabric materials can produce significant spatial contrasts in thermal admittance (for instance, roof materials tend to have much lower thermal admittances than wall or road materials. Such large spatial contrasts in thermal

admittance are generally absent in non-urban or rural environments). As a result, the magnitude of potential biases in remote sensed urban T_{surf} from microscale fluctuations depends on the facet material types viewed by the sensor and can change with viewing direction and sensor FOV. The effect of this phenomenon on thermal remote sensing has not been extensively studied, however, the magnitude of microscale fluctuations in T_{surf} is significant relative to a typical sUHI signal and thus constitutes a potentially large source of bias.

Both geometric and temporal shortcomings limit the representivity of traditional remote sensed evaluations of urban T_{surf} and sUHI. The magnitude of these biases has not been extensively studied, particularly from a long term, climatological perspective. These biases lead us to the question: What is the nature of the true sUHI? How does it vary temporally and over a full range of weather conditions? To address these questions, this study presents the first time-continuous, climatological analysis of sUHI derived from geometrically representative[1] radiometric hemispherical urban T_{surf} retrieved via the correction method described in Chapter 2. sUHI calculated for the eight month BUBBLE campaign in Basel, Switzerland and a year long subset of the EPiCC campaign in Vancouver, Canada are used to analyze the diurnal and seasonal character of sUHI and to assess the magnitude of and overcome geometric and temporal biases inherent in urban TIR remote sensing.

[1] A hemispherical view is not perfectly geometrically representative of urban surface geometry. This is best illustrated by visualizing an urban area from the perspective of a downward facing fish-eye camera. Geometric sampling biases are a result of lens distortions and the sensor cosine response. However, by sampling the surface 3-dimensionally, $T_{hem,\,r}$ is more representative of urban geometry than conventional 2-dimensional views of the surface. The geometric representivity of urban $T_{hem,\,r}$ is discussed in section 2.8.

3.2 Methods

This section describes the study area and provides a brief overview of the multiple line-of-sight atmospheric correction method used to derive time-continuous urban $T_{hem,\,r}$ for sUHI analysis. A thorough discussion of the method is included in Chapter 2.

3.2.1 A method to retrieve hemispherical radiometric urban T_{surf}

Remote sensing of TIR radiation is subject to atmospheric influence from gaseous and aerosol absorbers between the surface and the sensor. A pyrgeometer's broad waveband and wide FOV increase the potential for significant atmospheric influence on an observed TIR signal. These effects can result in differences of up to 10 K between the 'true' radiometric T_{surf} and brightness T_{surf} derived from remote sensed observations of upwelling TIR radiation. Atmospheric effects are important when comparing irradiances or remote sensed T_{surf} across different study sites and times, as differences in surface geometry, instrument height, and ambient conditions can introduce large spatiotemporal contrasts in the magnitude of atmospheric influence and degrade comparability. This is particularly salient for near-ground, broadband radiometers, as band-by-band spectral atmospheric transmittance can change significantly with path length, shown in Figure 2.2. As inter-site comparison is paramount in understanding the urban effect on T_{surf} and is the basis of sUHI analysis, accurate atmospheric correction of remote sensed T_{surf} is of prime importance. Thus, urban $T_{hem,\,r}$ in this study are derived using a multiple LOS correction routine which accounts for the 3-dimensionality of the urban surface, changing atmospheric conditions, and spectrally non-uniform sensor response. For each time step, the method generates a LUT of modeled at-sensor irradiances for a range of potential $T_{hem,\,r}$ using profiles of measured T_{air} and humidity. A corrected $T_{hem,\,r}$ for the target time step is then retrieved by matching the measured irradiance value to the closed modeled

irradiance - $T_{hem,\,r}$ pairing. The work flow, described in Figure 2.4, is repeated at 30-minute intervals over the eight month study period to retrieve a climatology of urban $T_{hem,\,r}$ for sUHI analysis.

First, surface-to-sensor path length and view factor geometries are calculated with the SUM sensor view model (Soux et al., 2004). Using a digital building model (DBM), SUM calculates path lengths from the surface to the sensor and angular view factors by projecting the pyrgeometer FOV onto a simplified representation of the surface, determining which points in the DBM are 'seen' by the sensor, and calculating the distance from each 'seen' point to the sensor. Path lengths are binned at 5° intervals and averaged over the azimuth angle. Finally, view factors are calculated for each 5° angular as each bin's proportion of the total view factor and normalized to unity.

Second, version 4.1 of the MODTRAN radiative transfer code (Berk et al., 1987) is used to model spectral at-sensor radiances for each angular path length. Runs are initialized using profiles of T_{air} and water vapor content collected concurrently at each time step. Spectral radiances are modeled over a bandpass of 1 to 2300 cm^{-1} at an emissivity of 0.95 and convolved by an extended dome transmittance function to ensure that modeled radiances replicate the actual remote sensed signal. Consultation with radiometer manufacturers made clear the need to extend the modeled bandpass beyond a typical longwave bandpass (approximately 250 - 2300 cm^{-1}), as silicone domed pyrgeometers transmit radiation at much smaller wavenumbers (longer wavelengths) than 250 cm^{-1} (40 $\mu\mathrm{m}$).

Third, radiances for each angular path length are integrated over the waveband and multiplied by their respective normalized view factors. Weighted and corrected angular radiances are integrated over the hemisphere to yield a modeled at-sensor irradiance as seen by the pyrgeometer for the target $T_{hem,\,r}$.

For each time step, these steps are repeated at an interval of 0.5 K for a predefined range of potential $T_{hem,\,r}$, with results aggregated into a lookup table relating modeled irradiances to corrected $T_{hem,\,r}$ for the observed ambient T_{air} and humidities. The measured irradiance is then matched with the closest modeled irradiance to return the associated corrected $T_{hem,\,r}$ for the target time step.

3.2.2 Method evaluation and sensitivity testing

Although MODTRAN has been shown to accurately model radiative transfer of broadband longwave radiation at urban canyon scale path lengths (Hoch, 2005; Hoch et al., 2007), the added complexity inherent in simulating fluxes of radiation hemispherically over complex urban terrain prompted a robust evaluation of the correction method using observations of upwelling longwave radiation (measured from 2 m, 10 m, and 30 m above ground level) over a simple, flat surface for a continuous 14-day period. In the evaluation, a modified version of the correction method uses $T_{hem,\,b}$ inferred from the lowest upwelling longwave measurement along with profiles of T_{air} and humidity to model irradiances at 10 m and 30 m at each time step. Modeled and measured irradiances match well over wide range of day and night mid-latitude atmospheric conditions, with results summarized in Table 2.2.

Sensor placement sensitivity testing in Section 2.4 shows that $T_{hem,\,r}$ is spatially variant when measured over urban areas at typical pyrgeometer heights. This introduces a potential bias in $T_{hem,\,r}$ as changing sensor position relative to canyon features alters view factor proportions of rooftops, roads, and walls. The sensitivity of $T_{hem,\,r}$ to sensor placement decreases as sensor height is increased, and $T_{hem,\,r}$ becomes spatially invariant at approximately 3.5 times mean building height (Roberts, 2010; Adderley et al., 2015). As such, these biases can be significantly reduced by mounting downward facing pyrgeometers slightly higher than typical.

Although pyrgeometers in both studies utilized in this campaign are mounted below the height at which $T_{hem,\,r}$ is spatially invariant, sensitivity tests in Section 2.4 show that the magnitude of this bias is relatively small for sensor placement in the BUBBLE campaign. Similar biases are expected in analysis of Vancouver sUHI as the sensor is mounted offset from surrounding rooftops (which contribute to large diurnal amplitude in $T_{hem,\,r}$ and larger deviation from T_{comp}). In addition, $T_{hem,\,r}$ shows good performance relative to T_{plan} when compared to T_{comp}, particularly under clear sky conditions when microscale spatiotemporal variations in urban T_{surf} and sUHI magnitudes are greatest. As such, the influence of biases in T_{hem} in sUHI analysis for both BUBBLE and EPiCC campaigns is likely small and relatively consistent.

3.2.3 A parameterization scheme

By virtue of requiring nearly 500 radiative transfer simulations per time step and significant post-processing, the method described in Section 3.2.1 is computationally expensive. This prompted the development of a parameterization scheme to facilitate more widespread usage of urban $T_{hem,\,r}$ for climatological and comparative sUHI analysis. In the parametrization, to reduce computational time, radiative transfer simulations are run for a single view factor weighted average path length representing the average distance from the surface to the sensor as ”seen” by the sensor over its FOV. This view factor weighted ”hemispherical” path length can be calculated using a sensor view model (such as SUM) or approximated by hand using a digital building model (although care should be taken to ensure the sensor cosine response is accurately represented). Using the view factor weighted path length, a suite of radiative transfer simulations is run prior to correction to retrieve ”hemispherical” broadband atmospheric transmittances for a range of potential humidities. Humidity-transmittance pairings are aggregated into a LUT, where the measured humidity at each time step can be matched with the

associated hemispherical transmittance. Using the hemispherical transmittance to calculate the fraction of surface emitted L_{up} reaching the sensor, measured L_{up} can then be decomposed into its surface and atmospheric emitted components, from which a parameterized $T_{hem,\,r}$ is calculated. Comparison of $T_{hem,\,r}$ derived from the correction method and the parameterization show good agreement, the results of which are included in Figure 2.24 and Table 2.4.

3.2.4 Study area

This study uses data from two long-term climatological campaigns: the Basel Urban Boundary Layer Experiment (BUBBLE) conducted over December 2001 through July 2002 in Basel, Switzerland (Rotach et al., 2005), and a year long subset of the the Environmental Prediction in Canadian Cities (EPiCC) (Voogt et al., 2007) campaign in Vancouver, Canada. Using the method described in Section 3.2.1, an eight month climatology of $T_{hem,\,r}$ are retrieved from radiation and meteorological data collected as a part of the BUBBLE campaign. Urban data were observed from a tower located in a mid-rise, largely residential neighborhood near city center at the "Basel Sperrstrasse" site. Rural reference data were observed from the "Lange Erlen" site approximately 6 km to the north east in the outskirts of the city of Basel.

During an intensive observation period (IOP) in late June/early July 2002, the Sperrstrasse canyon was instrumented with an array of infrared thermometers (IRT) to view individual canyon facet T_{surf} to sample representative road, roof, and wall surface temperatures (T_{road}, T_{roof}, and T_{wall} respectively). Plan and complete aspect ratios for the Sperrstrasse canyon are used to compute weighting schemes to retrieve complete and plan surface temperatures (T_{comp} and T_{plan} respectively) at 30 minute intervals over the IOP. T_{comp} represents a complete urban T_{surf}, where facet temperatures are weighted and averaged based on their areal proportion of the complete urban surface area. T_{plan} represents the Sperrstrasse site as viewed by a satellite

or aerial remote sensor in the nadir. Weighting schemes for T_{plan} and T_{comp} are included in Table 2.1. Urban T_{surf} derived from complete, plan, and hemispherical representations of the Sperrstrasse site are used to investigate the effect of sensor-surface geometry on remote sensed T_{surf} and sUHI, and to quantify the magnitude of geometric biases over a range of time scales and synoptic conditions. In addition, during the IOP, a second rural reference site ("Village Neuf"), located approximately 5 km SSE of the Sperrstrasse site, was used to investigate the influence of rural site characteristics on sUHI.

In addition to data from the BUBBLE campaign, radiation and meteorological variables observed as a part of the EPiCC project are used to derive a climatology of $T_{hem,\,r}$ for the year long period spanning October 2008 through September 2009 using the parameterization scheme. EPiCC urban and rural data were collected from an urban residential neighborhood site in central Vancouver (Sunset Tower) and from a rural site over a flat, non-irrigated, unmanaged field approximately 25 km to the SSW (Westham Island) near to the coast. These data provide a second, long term, time-continuous climatology of sUHI for comparison of seasonal and diurnal patterns, to understand the influence of urban and rural site selection and characteristics on sUHI, and to aid in developing a generalized model for sUHI development over multiple time scales.

The locations of urban and rural sites for BUBBLE and EPiCC campaigns are included in Figures 2.5 and 3.1 respectively. Site morphologies and observed variables for BUBBLE and EPiCC sites are described in Tables 3.1 and 3.2.

Figure 3.1: The EPiCC study site in Vancouver, Canada with urban and rural site locations indicated. An image showing the approximate surface coverage at the urban Sunset Tower site is shown in the inset (viewing towards the WSW from the top of the tower).

Table 3.1: A description of morphological parameters and measured variables for BUBBLE urban and rural sites. Modified from Rotach et al. (2005) to include only relevant parameters.

Site	Location Height	Morphological Characteristics[2]	Meteorological Variables[3]	Radiation [No of levels][4]
Basel Sperrstrasse *Urban street canyon* LCZ: 2	47.57° N 7.60° E 255 m a.s.l.	z_H = 14.6 m σ_H = 6.9 m H/W = 1.0 λ_C = 1.92 λ_P = 0.54 α = 11.0%	T_{air} [7] H [7] WV [12] WD [1] P [1]	L_{up} [3] L_{down} [5] K_{up} [2] K_{down} [3]
Lange Erlen *Rural parkland* LCZ: B/D	47.59° N 7.65° E 275 m a.s.l.	α = 21.4%	T_{air} [4] H [4] WV [3] WD [1]	L_{up} [1] L_{down} [1] K_{up} [1] K_{down} [1]
Village Neuf *Rural farmland* LCZ: D/F	47.57° N 7.56° E 240 m a.s.l.	α = 19.2%	T_{air} [3] H [3] WV [2] WD [1]	L_{up} [1] L_{down} [1] K_{up} [2] K_{down} [2]

[2] Morphological parameters for the Sperrstrasse site were calculated for a 250 m circular area surrounding the study sites using the method described in Grimmond and Oke (1999). z_H: average building height, σ_H: standard deviation of building height, λ_P: plan aspect ratio, λ_C: complete aspect ratio, H/W: local canyon height to width ratio, α: surface albedo.
[3] H: humidity, WV: wind velocity, WD: wind direction, P: pressure.
[4] L_{up}: upwelling longwave radiation, L_{down}: downwelling longwave radiation, K_{up}: upwelling shortwave radiation, K_{down}: downwelling shortwave radiation.

Table 3.2: A description of morphological parameters and measured variables for EPiCC urban and rural sites.

Site	Location Height	Morphological Characteristics[5]	Meteorological Variables	Radiation [No of levels]
Sunset Tower *Urban/Suburban neighborhood* LCZ: 6	49.23° N 123.07° W 2.0 m a.s.l.	z_H = 5.3 m λ_B = 0.29 λ_T = 0.15 λ_V = 0.22 λ_I = 0.37 α = 14.7%	T_{air} [1] H [1] WV [1] WD [1] P [1]	L_{up} [1] L_{down} [1] K_{up} [1] K_{down} [1]
Westham Island *Rural, unmanaged* LCZ: D	49.09° N 123.18° W 91.4 m a.s.l.	α = 20.6%	T_{air} [2] H [2] WV [2] WD [2]	L_{up} [1] L_{down} [1] K_{up} [1] K_{down} [1]

[5] λ_B: Plan area of buildings, λ_T: Plan area of trees, λ_V: Plan area of ground vegetation, λ_I: Plan area of impervious ground.

3.2.5 sUHI analysis

sUHI and clUHI magnitudes were calculated from $T_{hem,\,r}$ and T_{air} (measured from 2 m above ground level) as $\Delta T_{(urban\text{-}rural)}$ at 30 min intervals. Rural $T_{hem,\,b}$ was calculated an expanded version of equation 2.5 to remove emissivity effects,

$$T_{hem,\,b} = \sqrt[4]{\frac{\epsilon L_o^{\uparrow} + (1-\epsilon) L_{sky}^{\downarrow}}{\sigma}} \tag{3.1}$$

where $L_o^{\uparrow}$ is upwelling longwave radiation from the surface, $L_{sky}^{\downarrow}$ is reflected downwelling longwave radiation, and rural emissivity (ϵ) = 0.94. Sensitivity tests included in Section 2.4 of the companion paper show that screen level irradiances (z = 2 m) are not subject to significant

effects from the intervening atmosphere and do not require atmospheric correction. Rural irradiances in this study were measured from approximately 2 m above ground, thus rural $T_{hem,\,b}$ is approximately equal to $T_{hem,\,r}$.

To compare seasonal and diurnal patterns of sUHI and clUHI development over the BUBBLE campaign, mean monthly UHI magnitudes were normalized via,

$$UHI_{norm} = \frac{(UHI - UHI_{min})}{(UHI_{max} - UHI_{min})} \tag{3.2}$$

with UHI_{min} and UHI_{max} referring to minimum and maximum mean monthly sUHI and clUHI values over the climatology. This normalization restricts mean monthly UHI magnitudes to a range of values between zero (mean monthly UHI_{min} over the climatology) and one (mean monthly UHI_{max} over the climatology).

To investigate the influence of rural site characteristics on Basel's sUHI, sUHI magnitudes are calculated using $T_{hem,\,b}$ from a different rural site ("Village Neuf") over the summertime IOP. Observations at Village Neuf were intermittent and often discontinuous As such, a subset of nine partially-complete days was selected to represent $T_{hem,\,b}$ and sUHI over a range of cloud coverages, to investigate the influence of rural site characteristics and T_{surf} regimes on sUHI. As sUHI development is most variable in the late afternoon and evening hours, preference was given to days with continuous observations from early afternoon through the night. For each of the nine days $sUHI_{max}$ was used to calculate a normalized sUHI magnitude for both Lange Erlen and Village Neuf sites at 30 min intervals to compare patterns of sUHI development for the two sites. Mean normalized sUHI was then calculated at each time step over the nine day period. A normalized $T_{hem,\,b}$ was also calculated (using maximum $T_{hem,\,b}$ for each day) to compare T_{surf} regimes between the two sites.

3.3 Results

3.3.1 Diurnal and seasonal variability in sUHI magnitudes

Figure 3.2 shows seasonal variations in diurnal patterns of mean monthly hemispherical sUHI magnitudes at 30 minute intervals for the BUBBLE campaign. Contour plots are interpolated between months to smooth and reduce noise in the day-to-day signal. The sUHI in Basel displays significant seasonal variation, largest in the daytime hours, and is strongly controlled by day length and solar angle. Compared to daytime sUHI, nighttime sUHI does not vary significantly across seasons.

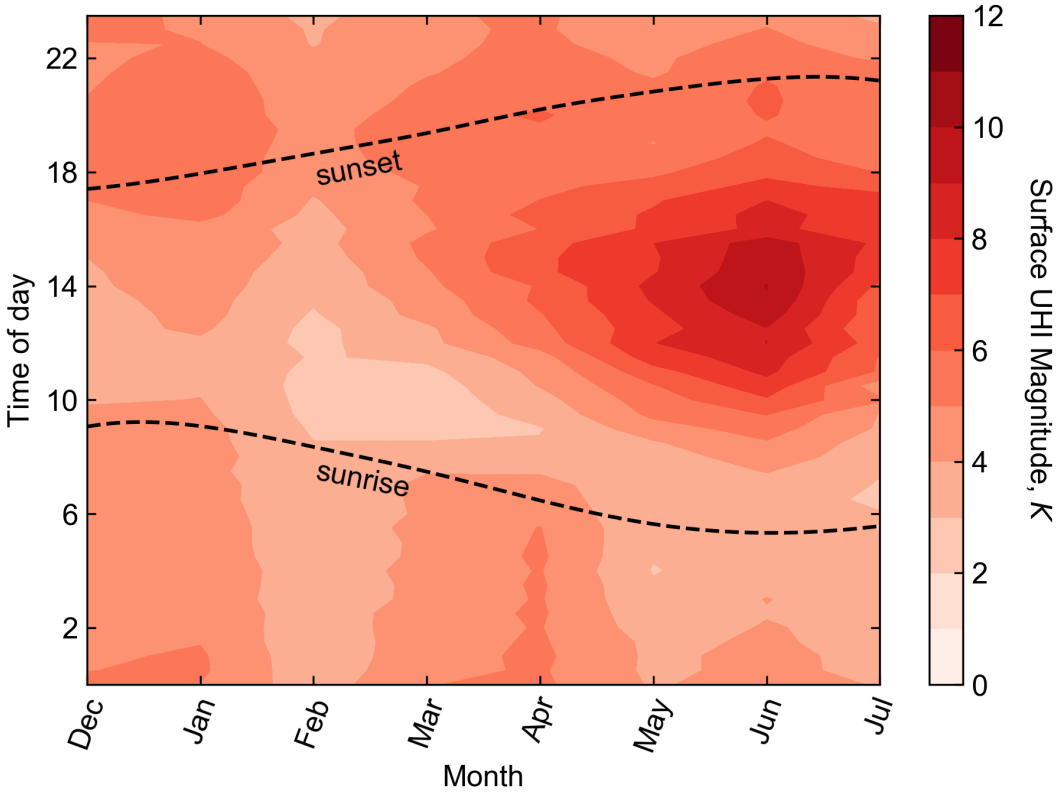

Figure 3.2: A heatmap of mean half hourly hemispherical sUHI for each month calculated at 30 min intervals for the BUBBLE campaign. Results are interpolated between months.

Figure 3.3 shows seasonal variation in diurnal patterns of mean monthly clUHI calculated for the same study period as Figure 3.2. clUHI development is strongly controlled by the timing of sunset/sunrise cycles and displays the largest seasonal variance in the hours immediately after sunset. Daytime clUHI does not vary significantly across seasons.

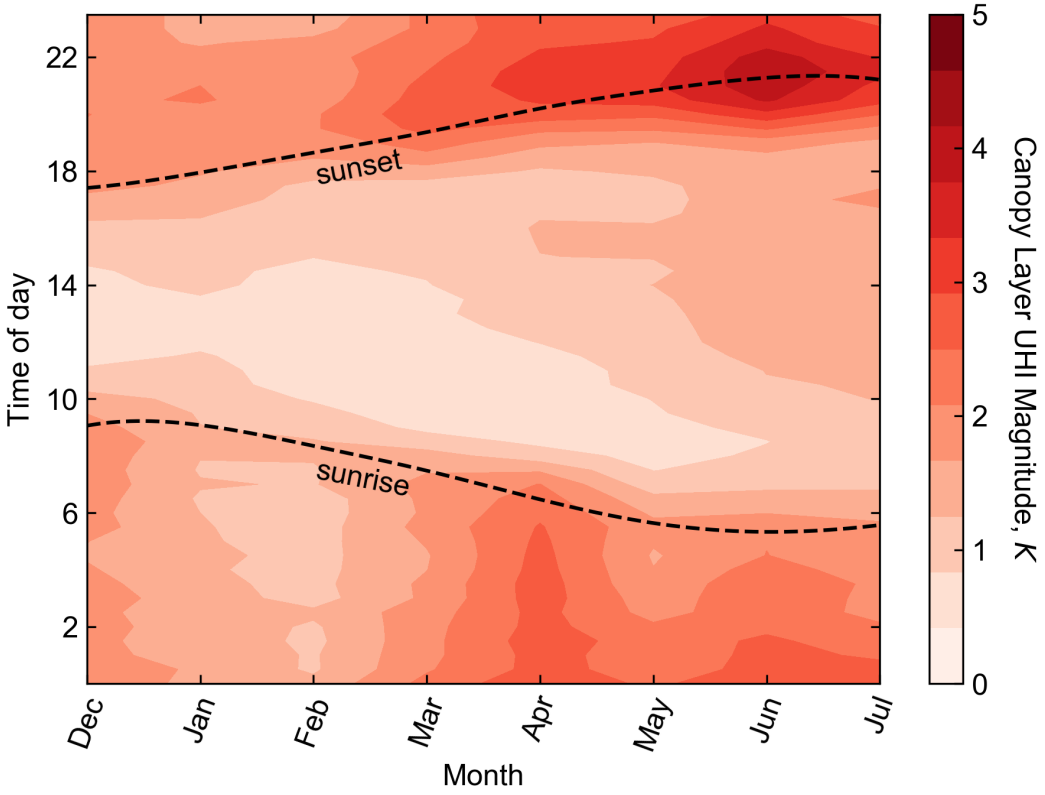

Figure 3.3: A heatmap of mean half hourly canopy layer UHI for each month calculated at 30 min intervals for the BUBBLE campaign. Results are interpolated between months.

Figure 3.4 shows seasonal variation in the difference between mean monthly hemispherical $\text{sUHI}_{\text{norm}}$ and $\text{clUHI}_{\text{norm}}$ for the BUBBLE campaign. By restricting UHI values to a range between zero and one, diurnal patterns of sUHI and clUHI can be compared directly. Comparison of the two in summer shows a peak sUHI approximately two hours after solar noon (when clUHI is small) and peak clUHI approximately two hours after sunset (when sUHI is small). Values near zero in the winder months indicate little variation in both sUHI and clUHI.

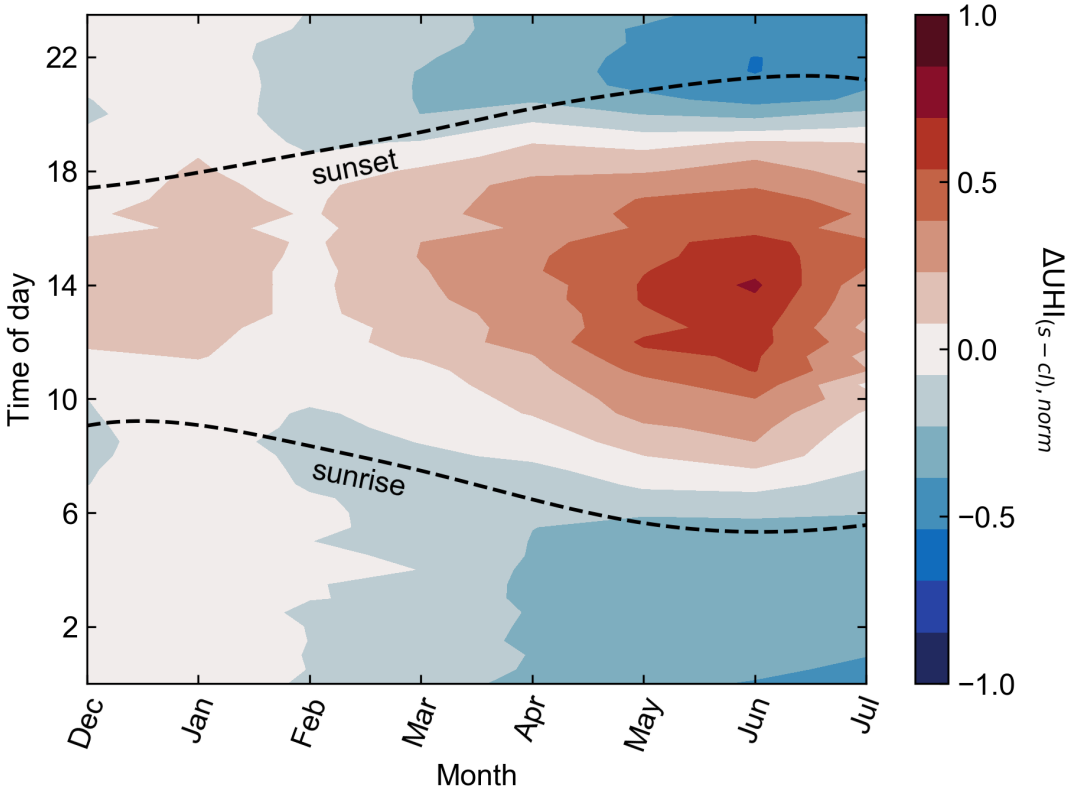

Figure 3.4: A heatmap of the difference between mean half hourly hemispherical normalized sUHI and canopy layer UHI for each month calculated at 30 min intervals over the BUBBLE campaign. Results are interpolated between months.

Figure 3.5 shows seasonal variations in diurnal patterns of mean monthly hemispherical sUHI magnitudes at 30 minute intervals for the EPiCC campaign. The sUHI in Vancouver shows similar seasonal and diurnal patterns to the sUHI in Basel, but degrades more quickly in the late evening hours.

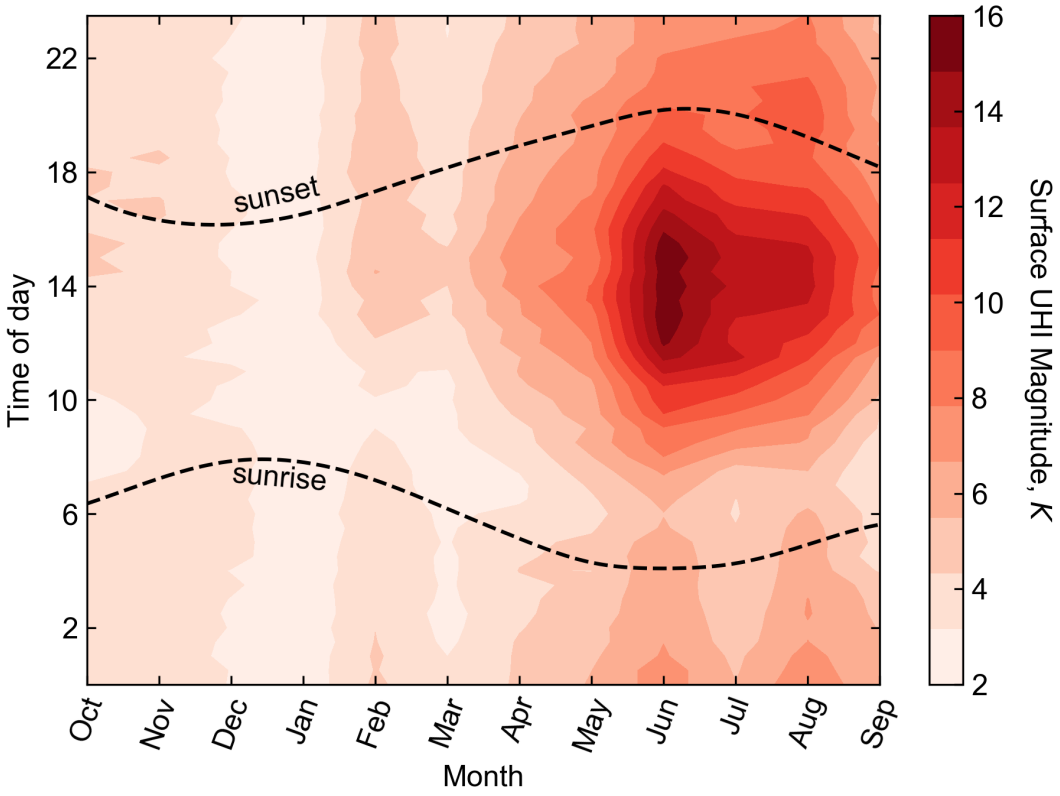

Figure 3.5: A heatmap of mean half hourly hemispherical sUHI for each month calculated at 30 min intervals for a year-long subset of the EPiCC campaign. Results are interpolated between months.

Figure 3.6 shows hemispherical sUHI magnitudes for the eight month BUBBLE campaign and binned for December through February and April through July, roughly representing cold and warm seasons. Diurnal variability in sUHI magnitudes and seasonal $sUHI_{max}$ is concentrated during the warm summer months.

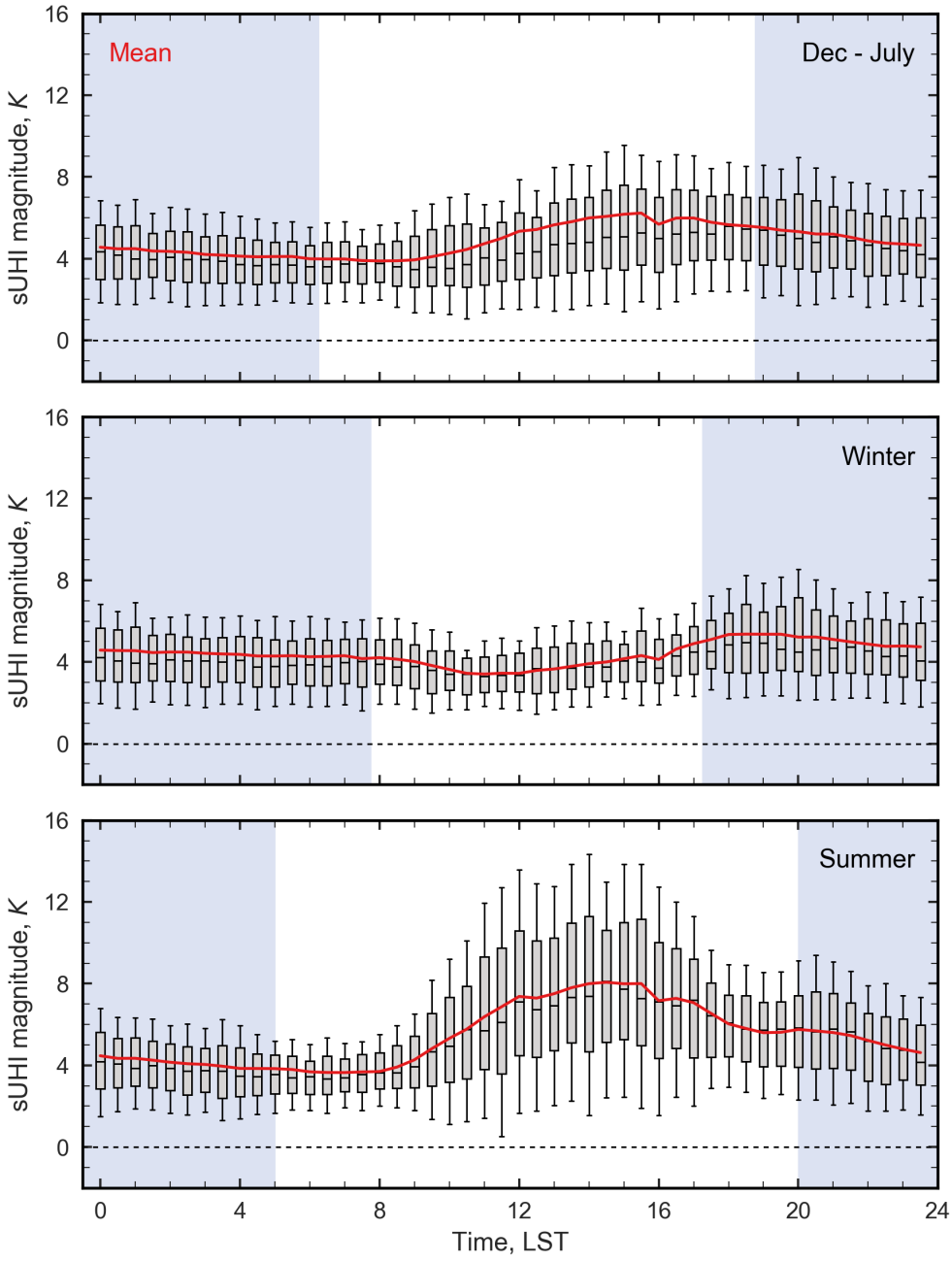

Figure 3.6: Hemispherical sUHI magnitudes for the eight month BUBBLE climatology (top) and binned for December through February (middle) and April through July (bottom) months. Grey shading indicates nighttime hours averaged over the bin interval.

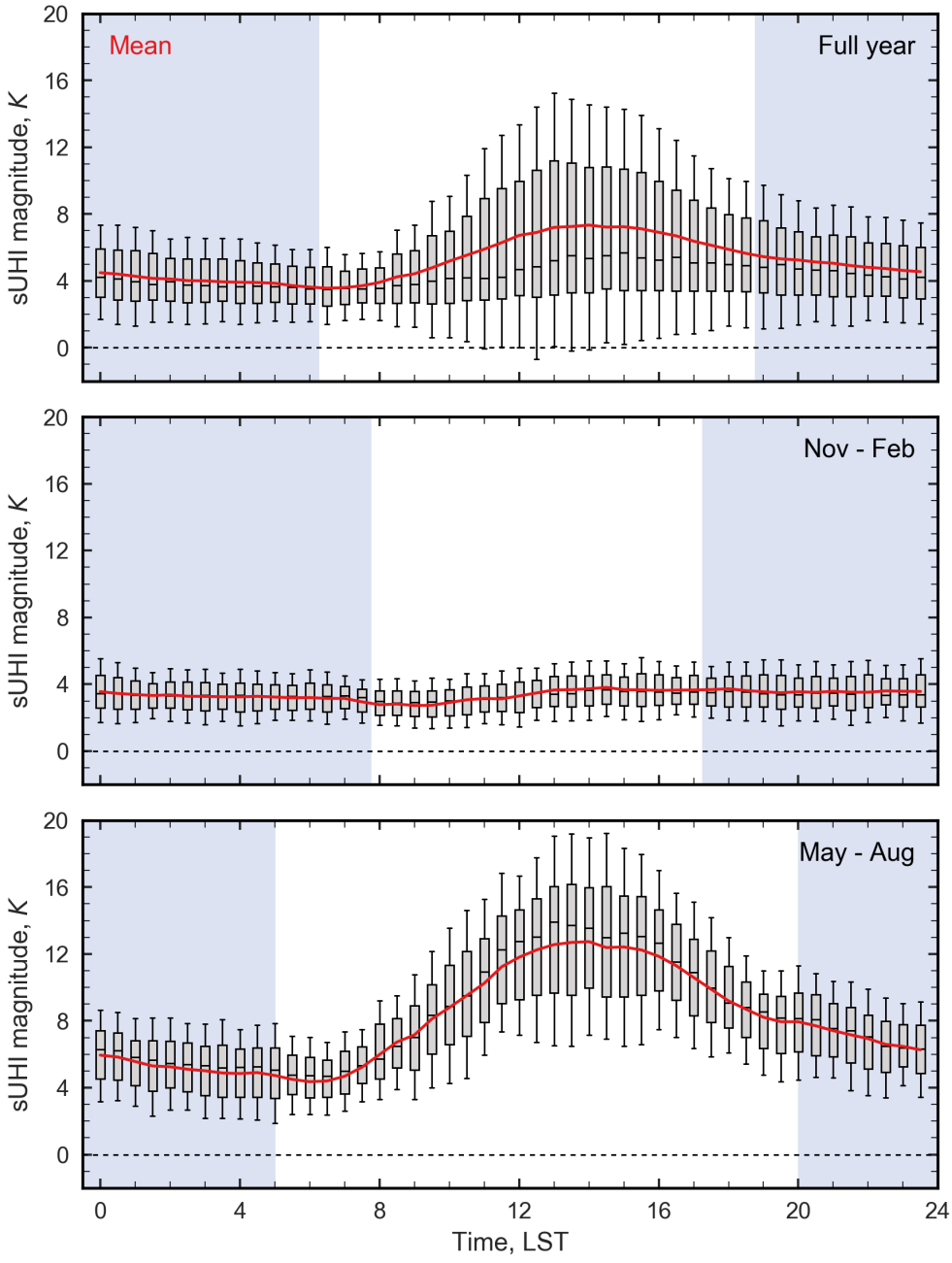

Figure 3.7: Hemispherical sUHI magnitudes for the year-long EPiCC climatology (top) and binned for December through February (middle) and April through July (bottom) seasons. Grey shading indicates nighttime hours averaged over the bin interval.

3.3.2 The effect of sensor-surface geometry on sUHI

Figure 3.8 shows sUHI magnitudes calculated from urban T_{comp}, T_{plan}, and T_{hem}. Compared to sUHI viewed from a complete representation of the urban surface ($sUHI_{comp}$); nadir ($sUHI_{nadir}$) and hemispherical ($sUHI_{hem}$) views of the surface overestimate $sUHI_{comp}$ by day and underestimate $sUHI_{comp}$ by night. $sUHI_{nadir}$ shows the greatest diurnal range of magnitudes, particularly under clear sky 'satellite friendly' conditions.

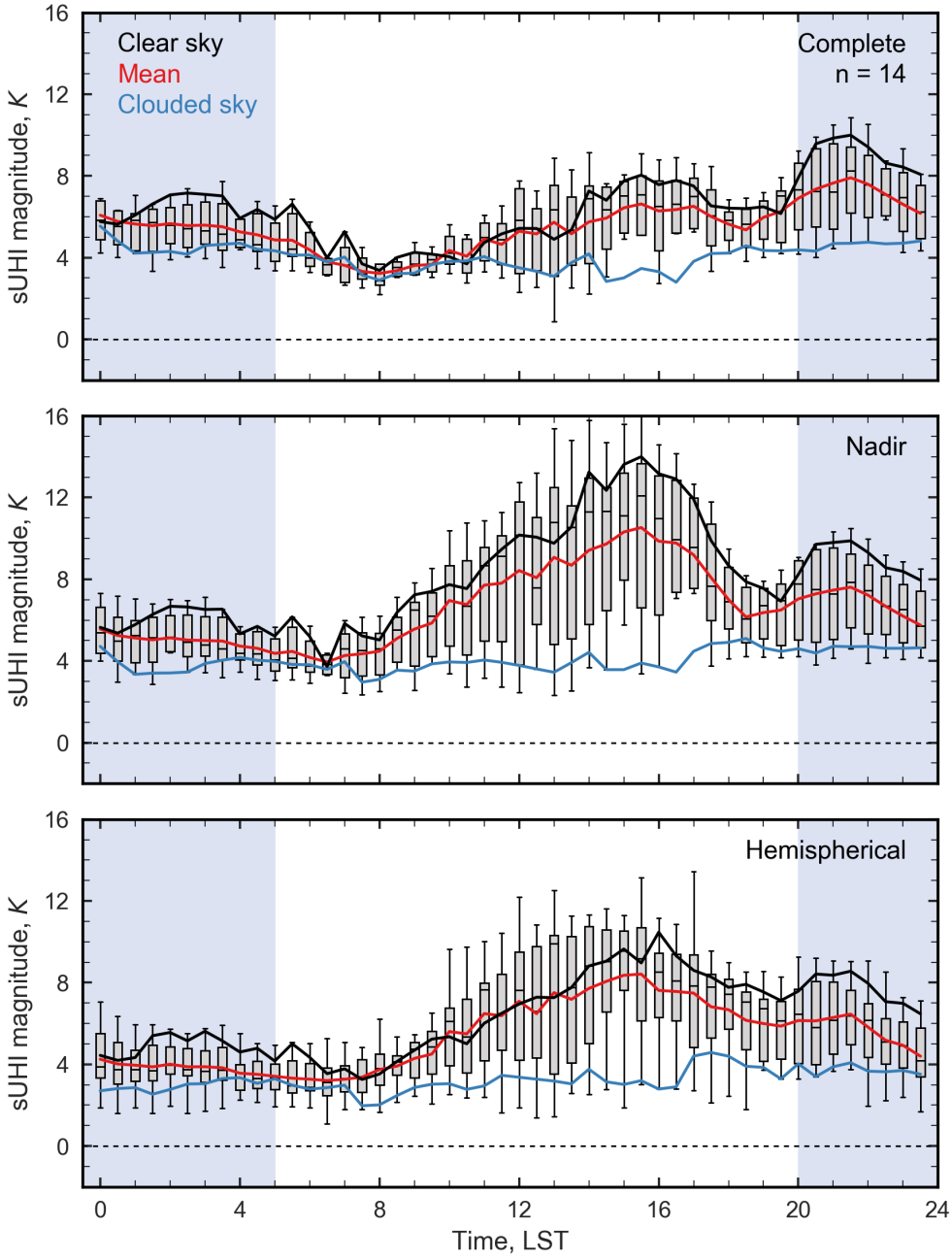

Figure 3.8: A comparison of sUHI magnitudes from complete ($sUHI_{comp}$), hemispherical ($sUHI_{hem}$), and nadir ($sUHI_{nadir}$) remote sensed representations of the Sperrstrasse canyon over the BUBBLE IOP. Each plot includes mean sUHI, as well as case days representing sUHI under clear sky and clouded sky conditions.

3.3.3 The effect of meteorological conditions on sUHI

BUBBLE

Figure 3.9 shows mean and maximum hemispherical sUHI magnitudes ($sUHI_{mean}$ and $sUHI_{max}$) as a function of solar radiant exposure for each day of the BUBBLE campaign. Point shading indicates the season, where black is winter (Nov - Feb), white is spring (Mar - Apr), and red is summer (May - Aug). A clear positive relationship is observed between accumulated solar radiation and both $sUHI_{max}$ and $sUHI_{mean}$.

Figure 3.10 shows hemispherical $sUHI_{mean}$ and $sUHI_{max}$ magnitudes as a function of mean wind velocity for each day of the BUBBLE climatology. A weak negative relationship is observed between mean wind velocity and $sUHI_{max}$, where larger $sUHI_{max}$ occurs under low wind conditions. $sUHI_{mean}$ yields a slightly more muted relationship. Similar results are observed when rural winds are substituted. Figure 3.11 shows hemispherical $sUHI_{mean}$ and $sUHI_{max}$ magnitudes as a function of mean atmospheric water vapor content for each day over the BUBBLE campaign. No discernible relationship is observed between atmospheric water vapor content and $sUHI_{mean}$ or $sUHI_{max}$. In both figures, colors indicate solar radiant exposure accumulated over each day (yellow is large accumulated insolation, brown is small).

Figured 3.12 shows hemispherical sUHI magnitudes as a function clUHI measured over the summer months of the BUBBLE campaign (May through July 2002). Winter hours are omitted as both sUHI and clUHI are small and display minimal variation in winter. The relationship between sUHI and clUHI is complex and highly dependent on time of day - owing largely to similar, but slightly offset patterns of sUHI and clUHI development. Coloring in the daytime plot indicates time of day: Red is morning (5:00 - 9:00 LST), gray is midday hours (9:30 - 17:00 LST), and yellow is evening hours (17:30 - 20:00 LST).

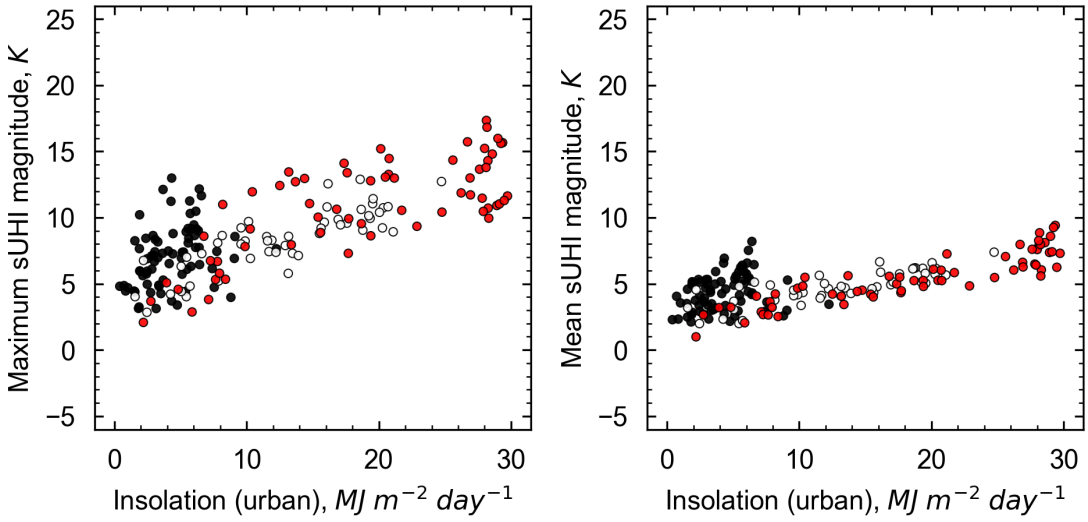

Figure 3.9: Maximum and mean 24 h hemispherical sUHI magnitude for each day of April through July during the BUBBLE campaign versus integrated solar radiant exposure measured at the Sperrstrasse site over the same 24 h period. Color indicates season: black is winter (Nov - Feb), white is spring (Mar - Apr), and red is summer (May - Aug).

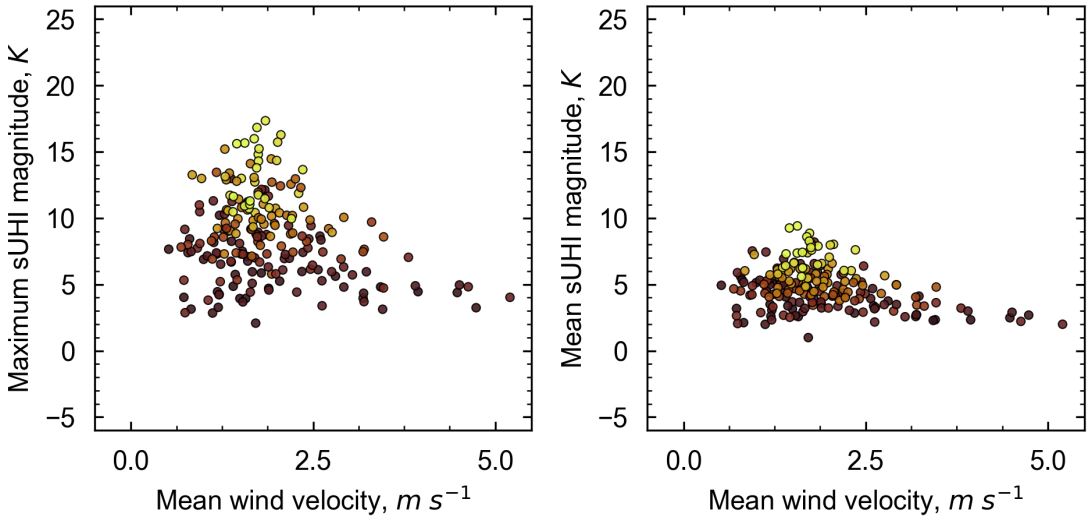

Figure 3.10: Maximum and mean 24 h hemispherical sUHI magnitude for each day of the BUBBLE campaign versus mean wind velocity measured at approximately 2 m above ground at the Sperrstrasse site. Coloring indicates integrated solar radiant exposure over each day.

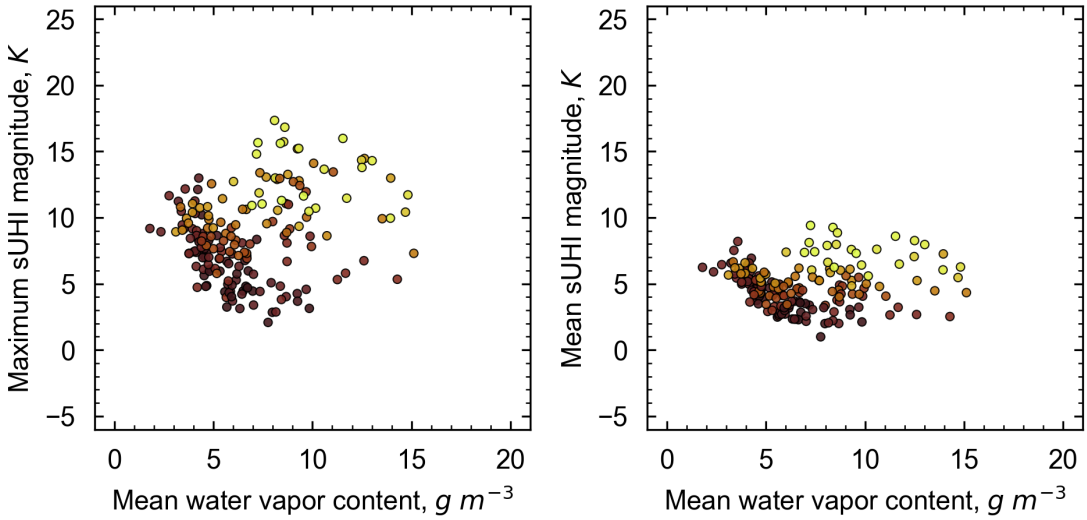

Figure 3.11: Maximum and mean 24 h sUHI magnitude for each day of the BUBBLE campaign versus atmospheric water vapor content measured at 2 m at the Sperrstrasse site. Similar patterns are observed when rural water vapor content is substituted. Coloring indicates integrated solar radiant exposure over each day.

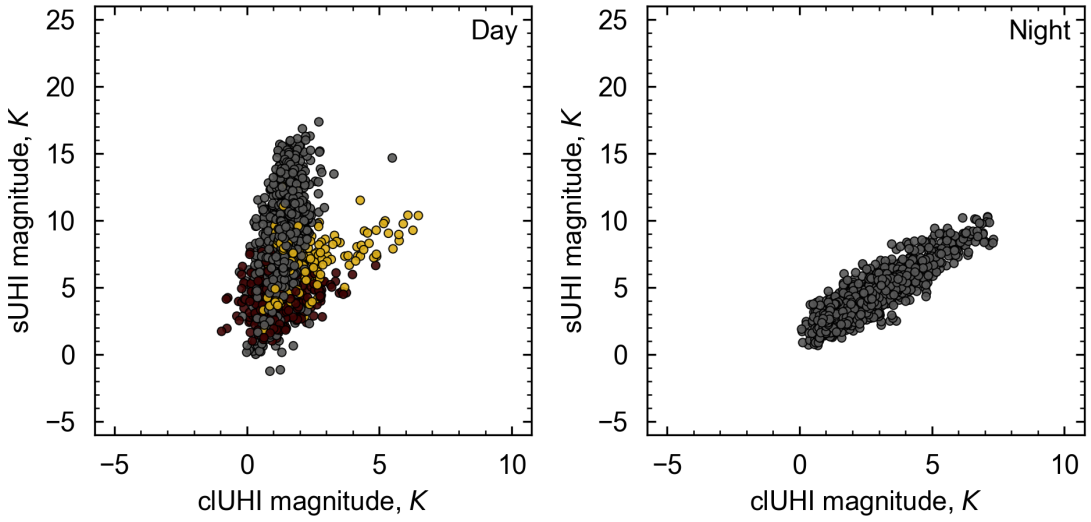

Figure 3.12: sUHI magnitude versus clUHI magnitude binned for day and night calculated over the summer months of the BUBBLE campaign calculated for the Sperrstrasse and Lange Erlen sites. Coloring in the daytime plot indicates time of day: Red is morning (5:00 - 9:00 LST), gray is midday hours (9:30 - 17:00 LST), and yellow is evening hours (17:30 - 20:00 LST).

EPiCC

Figure 3.13 shows hemispherical $sUHI_{mean}$ and $sUHI_{max}$ as a function of solar radiant exposure over each day of the year long EPiCC Vancouver campaign. Point shading indicates the season, where black is winter (Nov - Feb), white is spring (Mar - Apr), red is summer (May - Aug), and blue is fall (Sept - Oct). A clear positive relationship is observed between accumulated solar radiation and both $sUHI_{max}$ and $sUHI_{mean}$, with significant seasonal variation.

Figure 3.14 shows hemispherical $sUHI_{mean}$ and $sUHI_{max}$ magnitudes as a function of mean wind velocity for each day of the EPiCC Vancouver campaign. A weak negative relationship is observed between mean wind velocity and both $sUHI_{mean}$ and $sUHI_{max}$, where larger sUHI magnitudes tend to occur under low wind conditions. Higher overall sUHI

magnitudes and mean wind velocities in Vancouver make the relationship between sUHI and mean wind velocity slightly more evident. Similar results are observed when rural winds are substituted. Figure 3.15 shows hemispherical $sUHI_{mean}$ and $sUHI_{max}$ magnitudes as a function of mean atmospheric water vapor content for each day of the EPiCC Vancouver campaign. In contrast to findings in the BUBBLE campaign, a weak relationship between sUHI and humidity is observed. However, the apparent relationship may be a product of Vancouvers proximity to the coast and distinct wet and dry seasons, as there is significant seasonal variation in both sUHI and atmospheric water vapor content. In both, colors indicate solar radiant exposure accumulated over each day (yellow is large accumulated insolation, brown is low).

Figured 3.16 shows hemispherical sUHI magnitudes as a function of soil water vapor content measured over May 2009 of the EPiCC Vancouver campaign. May was selected to show a wide range of soil water contents and sUHI magnitudes. A negative relationship is observed between sUHI and soil water vapor content by day where larger sUHI magnitudes often occur on days with lower soil water vapor content. No discernible relationship between sUHI and soil water vapor content is observed at night.

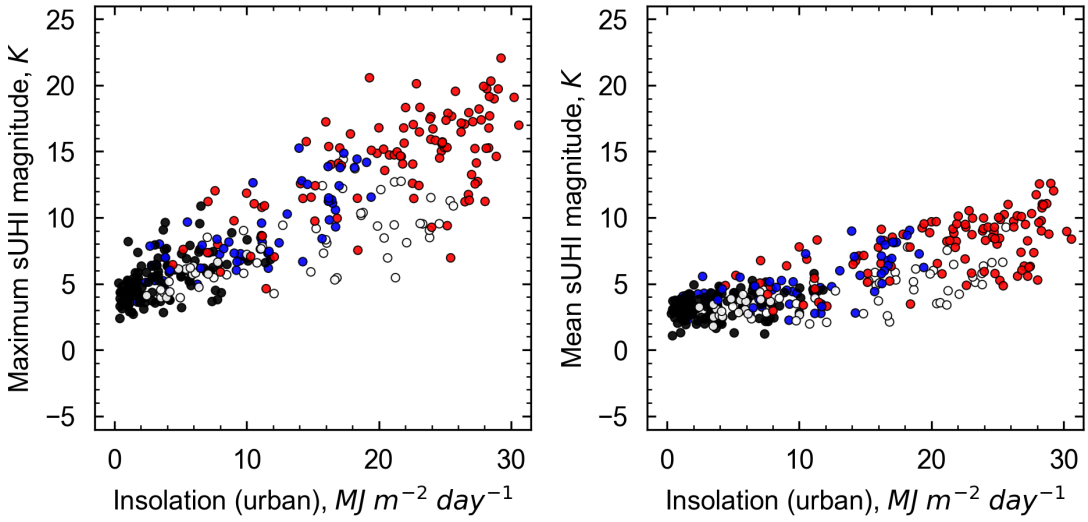

Figure 3.13: Maximum and mean 24 h hemispherical sUHI magnitude for each day of the EPiCC climatology versus integrated solar radiant exposure measured at the Sunset tower site over the same 24 h period. Color indicates season: black is winter (Nov - Feb), white is spring (Mar - Apr), red is summer (May - Aug), and blue is fall (Sept - Oct).

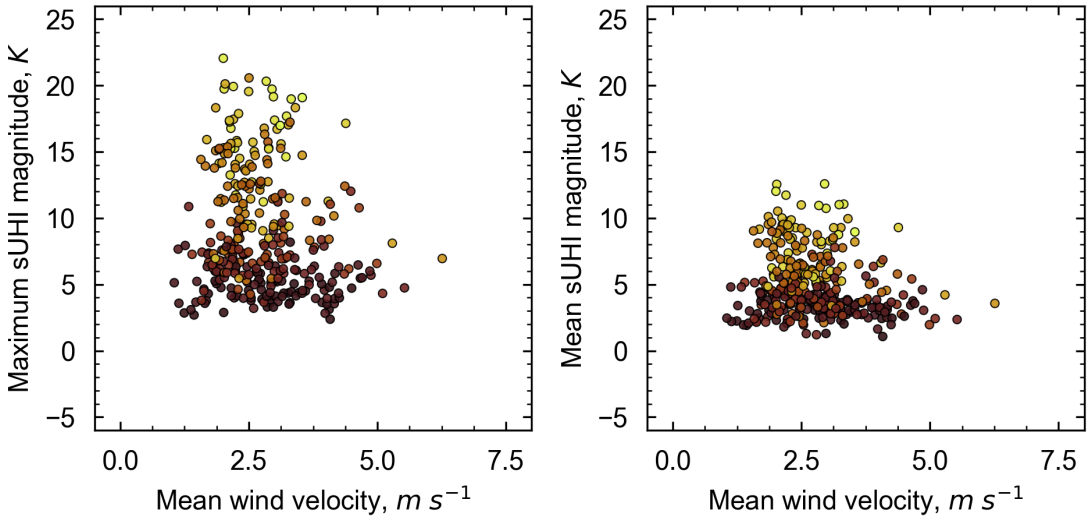

Figure 3.14: Maximum and mean 24 h hemispherical sUHI magnitude for each day over the EPiCC climatology versus mean wind velocity measured at approximately 10 m above ground at the Sunset tower site. Similar patterns are observed when rural mean wind velocity is substituted. Coloring indicates integrated solar radiant exposure over each day.

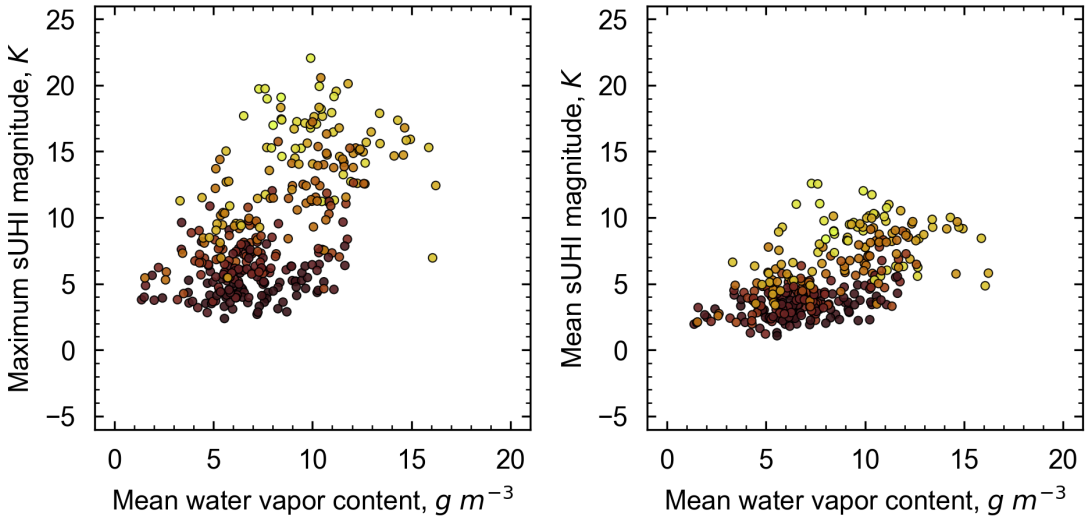

Figure 3.15: Maximum and mean 24 h $\text{sUHI}_{\text{hemi}}$ magnitude versus mean atmospheric water vapor content measured at 2 m at the Sunset tower urban site in Vancouver, Canada. Similar patterns are observed when rural water vapor content is substituted. Coloring indicates integrated solar radiant exposure over each day.

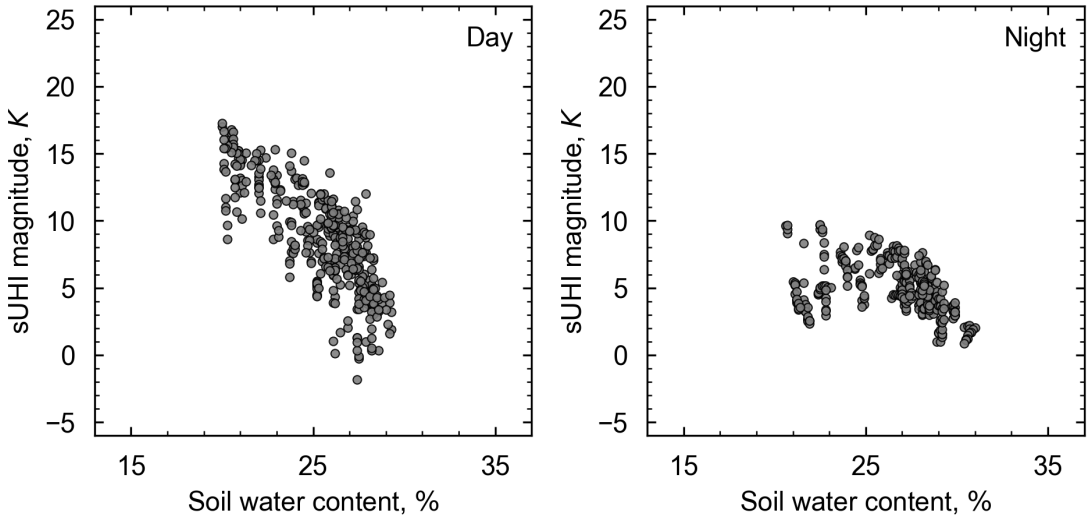

Figure 3.16: $sUHI_{hemi}$ magnitude versus volumetric soil water content measured from 0.05 m below the surface at the Westham island site in Vancouver, Canada for May 2009 binned for day (11:00 - 17:00 LST) and night (22:00 - 5:00 LST) hours.

3.3.4 The effect of rural/non-urban characteristics on sUHI

Figure 3.17 shows urban $T_{hem,\,r}$ from the Sperrstrasse site and rural $T_{hem,\,b}$ for the Lange Erlen and Village Neuf sites as well as their associated hemispherical sUHI magnitudes for a representative, summertime clear sky day. In addition, the figure shows mean normalized hemispherical sUHI and $T_{hem,\,b}$ (calculated from maximum sUHI and $T_{hem,\,b}$ values for each day) for the Lange Erlen and Village Neuf stations. Days were chosen to represent a wide range of summertime conditions and cloud coverages, however, observations at the Village Neuf site were intermittent and n = 9 only applies to hours after 12:00 LST when data could be continuously sampled. These analyses were not performed for the EPiCC campaign because only one rural site was available.

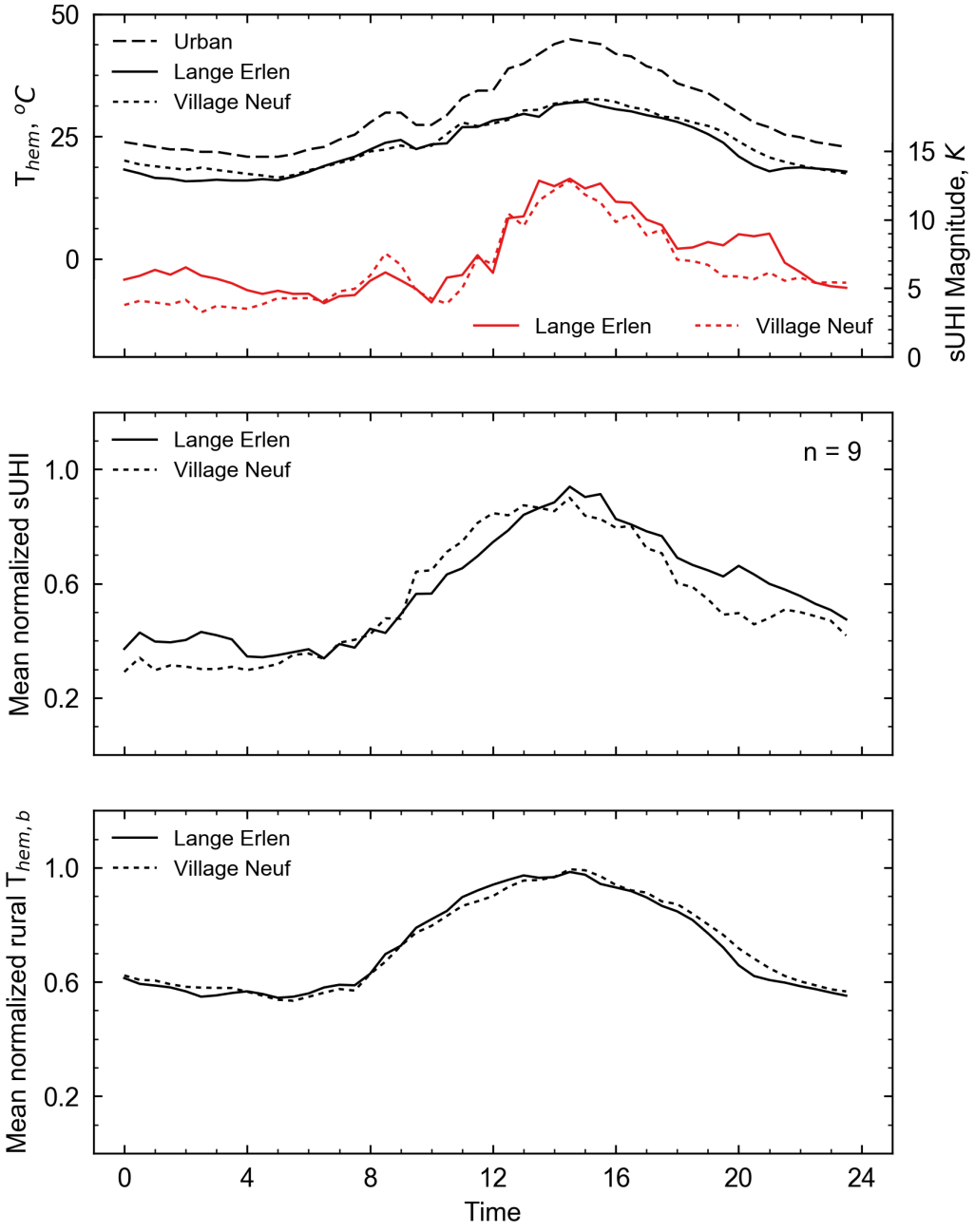

Figure 3.17: Top: T_{hem} from the Sperrstrasse urban and Lange Erlen and Village Neuf sites and sUHI magnitudes calculated from the two rural stations for a representative summer clear sky day. Middle and bottom: Mean normalized hemispherical sUHI and $T_{hem, b}$ calculated for the Lange Erlen and Village Neuf sites. Data at Village Neuf before noon were intermittent, thus n = 9 only applies to values after 12:00 LST. Both sites are sampled over the same truncated period on days with incomplete data.

3.4 Discussion

Oke et al. (2017) presents a generalized conceptual model for sUHI development for multiple representations of the surface. However, the results in Oke et al. (2017) are based on simulations of an idealized urban area without trees, complex non-orthogonal surface geometry, or sloped facets and have not been supported observationally. The results in this chapter provide an ideal platform to test conceptual understanding of sUHI development, to understand and characterize the diurnal and seasonal nature of sUHI, and to elucidate meteorological and climatological factors that drive its development.

3.4.1 Diurnal patterns of sUHI

sUHI development is the result of urban modification to surface geometry and thermal and radiative properties, most notably sky-view-factor, impervious surface fraction, and thermal admittance (and by relation, urban-rural soil moisture contrasts). These differences alter urban heating/cooling rates relative to non-urban spaces and provide the genesis for diurnal sUHI development. In the early morning hours, rural surfaces respond quickly to insolation at low solar angles, and rural T_{surf} rapidly increases. In contrast, shading by urban features causes urban T_{surf} to respond more slowly, resulting in a small $sUHI_{min}$ in the hours just after sunrise. This is observed in Basel across all representations of urban T_{surf} in Figure 3.8 and in the generalizable case presented for Vancouver sUHI in section 3.4.1 and Figure 3.18. Through the late morning hours, urban heating rates increase relative to rural rates as the solar zenith angle decreases and low thermal admittance facets (particularly rooftops) experience more direct insolation and quickly heat up. Increases in urban T_{surf} are amplified by the abundance of impervious surfaces, which result in a smaller fraction of insolation partitioned to latent heat relative to vegetated non urban spaces. After the initial spike in rural heating in the early

morning hours, urban heating rates overtake rural approximately three to four hours after sunrise and the sUHI slowly grows through midday to a peak at approximately two hours hours after solar noon. In the hours after $sUHI_{max}$, the solar zenith angle increases and both urban and rural heating rates decline and begin to converge, as shading by canyon geometry causes some facets to begin to cool.

In the afternoon hours, both urban and rural surfaces transition to cooling; this can lead to several different patterns in evening sUHI development and is strongly controlled by urban surface structure. Relative to non-urban spaces, cooling rates for wall and road facets lag slightly as a result of canyon radiation trapping, this is offset by increased cooling rates for low thermal admittance rooftop facets. These two factors control whether sUHI grows or shrinks in the hours after $sUHI_{max}$. In urban areas with relatively unobstructed sky-view-factors or large rooftop plan area fractions, strong radiative cooling can lead to a sharp reduction in sUHI. The opposite is true of urban areas with restricted sky view factors and tall street canyons with large wall surface area fractions, where canyon radiative trapping reduces radiative cooling and sUHI is maintained through the evening. For the Sperrstrasse canyon, the combination of a narrow but relatively low street canyon results in a slight reduction in Basel's sUHI as strong radiative cooling of rooftops is slightly offset by canyon radiation trapping. In Vancouver, urban cooling rates quickly overtake rural rates - owing to strong radiative cooling - and sUHI declines precipitously after $sUHI_{max}$. The dependence of sUHI development on canyon geometry is illustrated well by comparing nadir and complete representations of sUHI observed in Basel. A nadir view, by virtue of oversampling rapidly cooling rooftops, observes a strong evening decline in sUHI. In contrast, by sampling vertical facets that cool more gradually, this decline is less evident in sUHI calculated from a complete view of Basel T_{surf}. Thus, as expected, remote sensed sUHI analysis is also directionally dependent and subject to anisotropic effects when viewed from a narrow-FOV sensor. These effects not only affect the magnitude of remote

sensed sUHI, but may also alter perceived diurnal patterns of sUHI.

After sunset, the unobstructed rural sky-view-factor allows for strong radiative cooling of the surface and rural cooling rates spike relative to urban, leading to a slight jump in sUHI. This is observed in Vancouver sUHI as a slight reduction in the rate of sUHI decline near 20:00 LST. However, variations in rural thermal admittance, surface geometry, land cover and use, and/or influence from surrounding terrain can result in large contrasts in rural cooling rates. All of these factors show strong spatiotemporal variation, resulting in large differences in sUHI development depending on rural site characteristics, similar to observations of variation in clUHI based on rural siting in (Runnalls and Oke, 2000). This is illustrated by two different patterns of post-sunset sUHI development observed for the two rural sites in Basel. Although similar in terms of surface coverage and site geometry, hilly terrain surrounding the Lange Erlen site results in suspected cold air drainage and an increased rural cooling rate, particularly following hot, clear sky days. This effect is not present at the Village Neuf site, where nocturnal cooling rates are likely driven primarily driven by radiative losses. The ”extra”, largely non-radiative cooling at the Lange Erlen site results in a strong second peak in sUHI that is not present in sUHI calculated using the Village Neuf site. In the context of the Lowry method discussed in Chapter 1, $V_{M,\,R}$ measured from the Lange Erlen site and $V_{M,\,U}$ are not subject to the same V_L. Thus, equation 1.3 does not yield a perfectly isolated V_H in the hours just after sunset.

Following site dependent effects on sUHI in the hours after sunset, sUHI in Basel is relatively constant over the nighttime hours, with slight growth observed on clear nights where canyon radiation trapping retards urban nocturnal cooling rates relative to rural. In contrast, mean sUHI in Vancouver decreases through the night as the urban area experiences slight cooling. Both of these cases demonstrate the dependence of observed sUHI on urban and rural site characteristics and sensor-surface geometry illustrating the need for proper critical analysis

of the ensemble of climactic forcings present at a given urban-rural pairing and the potential for influence from sensor or instrument bias.

The general temporal evolution of sUHI

Oke (1982) presents a generalizable model for diurnal clUHI development. A similar schematic is presented in Oke et al. (2017) for sUHI based on simulations in Stewart et al. (2014), this study provides the first observational support of modeled assessments of typical diurnal sUHI development. To provide for sUHI what Oke (1982) did for clUHI, Figure 3.18 presents the diurnal evolution of urban and rural $T_{hem,\,r}$, heating and cooling rates, and the resulting sUHI development constructed from mean urban and rural T_{hem} observed over the summer months of the EPiCC Vancouver. Mean aUHI calculated for the same time period is also included for reference. However, it should be noted that rural and urban T_{air} were measured from 2 m and 26 m respectively, so do not constitute a true clUHI.

Development regimes are similar to those found for simulations of diurnal sUHI in Oke et al. (2017), both in terms of the diurnal evolution of sUHI and its dependence on urban to rural differentials in heating/cooling rates. sUHI shows clear diurnal dependence on differential heating/cooling rates at the urban and rural sites, with greater urban heating rates observed from sunrise to approximately solar noon forcing the development of sUHI and greater urban cooling rates in the afternoon and evening hours forcing the destruction of daytime sUHI. These results are generalizable to other mid-latitude cities for sUHI measured over low- to mid-rise neighborhoods under summertime conditions.

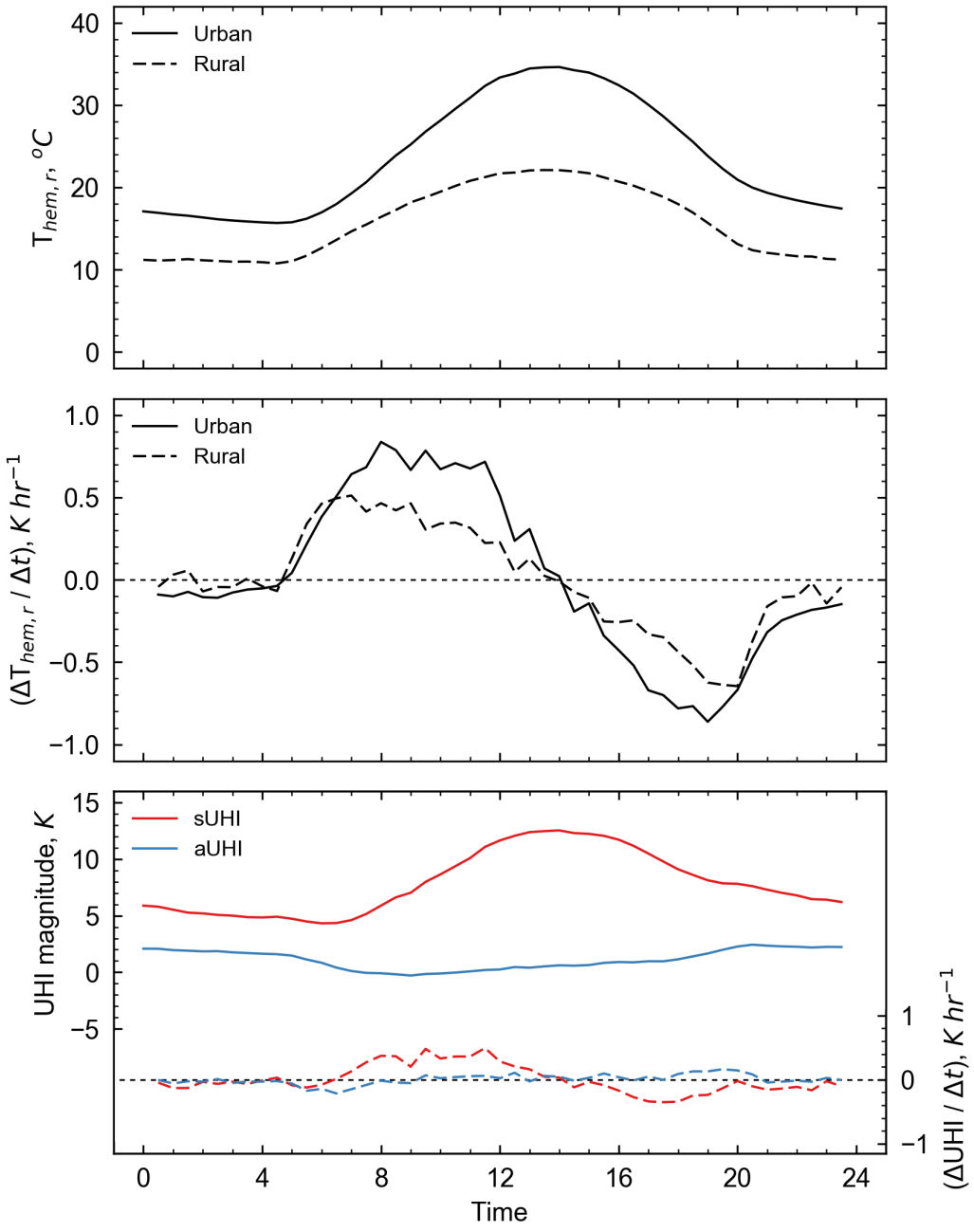

Figure 3.18: Top: Mean $T_{hem,\,r}$ for the Sunset tower (urban) and Westham island (rural) sites in Vancouver, Canada over May - Aug 2009. Middle: Mean heading/cooling rates for urban and rural sites. Bottom: Mean $sUHI_{hemi}$ and aUHI and the hourly rate of change in $sUHI_{hemi}$ and aUHI. n = 5905

3.4.2 Seasonal patterns of sUHI

Results in Figures 3.2 through 3.7 show that hemispherical sUHI in both Basel and Vancouver displays large seasonality, both in terms of its diurnal pattern and overall magnitude. Seasonal variations in sUHI are most evident during the daytime hours, where large seasonal contrasts in cloud cover frequency and solar angle exert strong control on daytime heating rates and sUHI development. Mean monthly $sUHI_{max}$ is observed near the summer solstice in both study areas, when days are longest and insolation on clear sky days is most intense, forcing large contrasts in urban-rural heating/cooling rates and the development of a strong sUHI. In winter, lower overall solar input and frequent cloud cover suppress the potential for urban-rural contrasts in heating/cooling rates and weakens wintertime sUHI development. In Basel, wintertime sUHI has a small peak shortly after sunset, when cold air drainage anomalously amplifies rural cooling rates, increasing the sUHI. This small, after-sunset peak in sUHI observed in both summer and winter observations is specific to the Lange Erlen site and is not generalizable. Cooling rates at the Vancouver Westham island rural site are not affected by cold air drainage and, as a result, sUHI does not display two diurnal peaks in summer nor a coherent peak after sunset in winter months. Thus, observations of seasonal variations in hemispherical sUHI in Vancouver are highly generalizable to other mid-latitude cities.

The contrast between sUHI and clUHI shown in Figures 3.2, 3.3, and 3.4 show that although sUHI and the clUHI have similar micro-meteorological genesis, climatic controls, and display similar seasonal variability, the two have different development regimes. This is evident when comparing normalized mean monthly hemispherical sUHI and clUHI - where the range of both types of UHI are restricted to values between zero and one. In winter, low solar input and frequent cloud cover inhibit variability in sUHI and clUHI and both are of similar normalized magnitudes. In summer, larger solar input fosters contrasts in urban-rural heating and cooling

rates and both clUHI and sUHI are most variable, with peak sUHI in the early afternoon when clUHI is smallest, and peak clUHI in the hours after sunset when sUHI is relatively low. These results suggest the following generalization: when conditions that foster the formation of strong urban-rural contrasts in T_{air} and T_{surf} are present (most notably a large solar input), sUHI peaks approximately two hours after solar noon and clUHI peaks approximately three to four hours after sunset. *Thus, a surface urban heat island is not simply a stronger, more pronounced, canopy layer urban heat island.*

3.4.3 Sensor-surface-sun geometries and sUHI

Sensor-surface geometry exerts significant influence on observed sUHI magnitudes. Two-dimensional, complete, and hemispherical observations of sUHI shown in Figure 3.8 over the BUBBLE IOP not only yield different magnitudes but also different diurnal sUHI regimes and peak timings. Variations in observed sUHI across different sensor sampling regimes are largest under clear sky, hot conditions, coinciding with typical seasonal and diurnal $sUHI_{max}$. In general, as urban T_{surf} is most often viewed from the top down, remote sensors preferentially sample horizontally oriented facets with unobstructed sky view factors and undersample or ignore vertical and sloped facets with more obstructed sky view factors. Over/undersampling of the urban surface changes both the magnitude and character of remote sensed urban T_{surf} and sUHI.

In an analysis of Basel sUHI from complete, nadir, and hemispherical representations of the surface, significant variation in remote sensed sUHI was observed across sensor sampling regimes at all times of the day. Variations in observed sUHI are most evident on clear sky, hot days in the hours after solar noon, when microscale spatiotemporal contrasts in urban T_{surf} are largest. Cloud cover suppresses the influence of sensor-surface geometry on remote sensed

sUHI by reducing microscale geometric and spatiotemporal contrasts in urban T_{surf}, resulting in less facet-scale heterogeneity in urban T_{surf} and reducing the overall magnitude of sUHI for all definitions.

By undersampling vertical and sloped urban surfaces and oversampling low thermal admittance materials, $sUHI_{nadir}$ overestimates mean afternoon $sUHI_{comp}$ by approximately 3.5 K and up to 6.0 K under clear sky satellite friendly conditions. This constitutes a significant bias in remote sensed $sUHI_{max}$ as $sUHI_{nadir}$ overestimates the 'true' $sUHI_{comp}$ by nearly double under clear sky conditions. As clear sky conditions are the only conditions under which satellite TIR remote sensors can operate, and make up a large fraction of the urban T_{surf} literature, these biases are pervasive and cannot be ignored. In contrast to $sUHI_{nadir}$, $sUHI_{hem}$ samples the urban surface in 3-dimensions ("seeing" a wider range of facet types and orientations) and yields a much smaller mean daytime overestimation (0.5 K), particularly under clear sky conditions (1.0 K), providing a significantly more representative depiction of urban T_{comp} and $sUHI_{comp}$, in addition to allowing for time-continuous analysis.

Results of sensor placement sensitivity testing in Section 2.4 show that $T_{hem,\,r}$ is dependent on sensor position and height relative to canyon features for pyrgeometers mounted below 3 to 5 times mean building height. As pyrgeometers in both EPiCC and BUBBLE campaigns were mounted below these heights, derived $T_{hem,\,r}$ include some bias towards facets that make up a majority of their FOV, these effects are translated into $sUHI_{hem}$. This bias results in a small overestimation of daytime T_{comp}, and an underestimation of nighttime T_{comp}, manifesting as a small increase (decrease) in daytime (nighttime) $sUHI_{hem}$. However, as these sensors are positioned offset from rooftops (the main source of positional bias), these biases are likely relatively small and consistent and do not exert a large influence on diurnal or seasonal patterns of $sUHI_{hem}$.

3.4.4 Meteorological controls on sUHI

sUHI is highly dependent on meteorological conditions, which account for much of the day to day variation sUHI magnitudes. Conditions that foster the largest microscale spatiotemporal contrasts in urban T_{surf} also entail the largest sUHI magnitudes. Contra, conditions that suppress microscale contrasts in T_{surf} show reduced sUHI magnitudes. As such, sUHI development is strongly tied to integrated solar radiant exposure accumulated over a day (Figures 3.9 and 3.13) and wind velocity (Figures 3.10, 3.14), which display positive and negative relationships with sUHI magnitudes respectively. Other variables also show weak (mean atmospheric water vapor content, shown in Figures 3.11 and 3.15) and weakly negative (soil water content, shown in Figure 3.16) relationships with sUHI, however, for these variables, conclusions about causality are more difficult to make. Meteorological controls on sUHI are summarized in Table 3.3.

The relationship between solar radiation and sUHI is relatively simple but easily misinterpreted. Surfaces (both urban and otherwise) change in temperature based on *accumulated* radiative or convective gains or losses - as such, instantaneous changes in insolation have little effect on sUHI magnitudes. Thus, to say that sUHI is a function of measured incoming solar radiation (in $\mathrm{W\,m^{-2}}$) does not accurately characterize the relationship and produces a significant amount of unrepresentative scatter. Strong accumulated solar heating of the surface combined with differences in urban and rural thermal properties and sunlit shading geometries fosters the development of large daytime urban-rural contrasts in T_{surf} and T_{air} and the development of strong sUHI by day and clUHI by night. Thus, $sUHI_{max}$ often coincides with $insolation_{max}$. Under cloudy conditions, reduced accumulated solar heating of the surface suppresses the development of urban-rural thermal contrasts, resulting in reduced sUHI magnitudes.

Wind velocity has a similarly nuanced relationship with sUHI. Winds affect surface heating and cooling rates by facilitating convective cooling (or, under less common circumstances, convective heating). In general, as wind velocity increases, convective heat losses increase and both T_{surf} and its spatial variability decreases. This suppresses microscale spatiotemporal variations in T_{surf} as hot sunlit surfaces experience greater rates of convective cooling under high wind conditions than cooler shaded surfaces. Thus, high wind velocities reduce overall urban and rural T_{surf} and inhibit sUHI development. Nighttime sUHI is also affected by wind velocity as the formation of a near surface thermal inversion, which increases radiative cooling in non-urban areas, requires calm winds. As such, increased nighttime wind velocity decreases nocturnal sUHI.

sUHI magnitudes in the BUBBLE and EPiCC campaigns yield slightly different relationships with atmospheric water vapor content, with no relationship observed in Basel and a weakly positive one observed in Vancouver. It is unlikely that these are a result of any significant physical or causal connection between the two variables as, in the absence of fog, humidity near the surface does not strongly influence surface heating or cooling rates in and of itself. Atmospheric transmittance of longwave radiation decreases sharply with small increases in water vapor when the atmosphere is very dry, with only marginal subsequent decreases - shown in Figure 2.15. As water vapor content increases from zero, variation in spectral atmospheric transmittance decreases. Therefore, typical variations in urban and rural humidities have little effect on the fraction of outgoing longwave radiation available for heating the canopy layer air volume through absorption and for heating of the surface by atmospheric emission. As a result, the relationship between humidity and sUHI is expected to be similar that found between humidity and correction magnitudes in Chapter 2. A weak positive correlation between the two is therefore likely a result of coincident seasonality in both variables as both mean daytime sUHI and mean water vapor mass densities are large in summer and small in winter. As

this seasonality is evident in both Basel and Vancouver, it is likely that a full climatology of sUHI and humidity would yield similar correlation (but not causation) in Basel as is observed in Vancouver.

Results in Runnalls and Oke (2000) indicate that rural thermal admittance (which is largely a product of rural soil moisture) exerts strong negative control over clUHI. A similar relationship is observed for sUHI in Vancouver when analyzed over long time scales. However, examining the diurnal character reveals a more complex relationship between the two. A higher rural soil moisture content increases rural thermal admittance, suppressing rural heating and cooling rates and reducing the overall T_{surf} amplitude at the rural site. Much of the urban surface is impervious and does not respond strongly to changes in soil moisture. Thus, Oke et al. (2017) suggests that with a higher rural soil moisture content, reduced nocturnal rural cooling rates could result in decreased nighttime sUHI. Conversely, by day, reduced rural heating rates may result in higher sUHI magnitudes. Results in Vancouver do not support these suggestions when viewed in aggregate. Over the daytime hours, in Vancouver, a negative relationship is observed between sUHI and rural soil moisture where sUHI is largest with low rural soil moisture. At night, no clear relationship between the two emerges. However, this relationship should be viewed with caution as both variables respond strongly to incoming solar radiation. Soil moisture content in Vancouver is greatest just before morning (when sUHI is small) and lowest in late afternoon (when sUHI is large). This results in a negative correlation when the two are compared over a time series, but may not indicate causality. In addition, Vancouver has distinct wet and dry seasons and little variability in soil moisture during the summer months (when sUHI is highly variable), study of the effect in cities with wet summers may yield a more complete picture of the relationship between sUHI and rural soil moisture.

Table 3.3: A summary of the relationship between sUHI, meteorological variables, and clUHI. These relationships are generalizable and represent the character of mean diurnal sUHI in response to changing conditions.

An increase in x, has a/an...	y effect on sUHI magnitude.
$\Delta T_{surf\ -\ air}$, K	*increasing*
T_{surf}, $^{\circ}\mathrm{C}$	*increasing*
T_{air}, $^{\circ}\mathrm{C}$	*increasing*
Insolation, $\mathrm{MJ\,m^{-2}\,d^{-1}}$	*increasing*
Atmospheric water vapor content, $\mathrm{g\,m^{-3}}$	*negligible*
Volumetric soil moisture content, $\%$	*decreasing*
Wind velocity, $\mathrm{m\,s^{-1}}$	*decreasing*
clUHI, K	*increasing*

clUHI and sUHI develop at different times of day and, thus, have a complex diurnal relationship. By day, variation in clUHI is minimal and shows weak positive correlation with sUHI. Occasionally, under clear sky conditions following hot days, strong evening radiative cooling forces clUHI development slightly before sunset. This causes a slight bifurcation in clUHI versus sUHI. By night, clUHI shows greater variation and a stronger, more positive relationship with sUHI, most evident on clear sky nights when urban-rural contrasts in air and surface cooling rates are strongest.

3.5 Conclusions

This chapter presents the results of an analysis of two time-continuous long-term climatologies of the surface urban heat island effect in Basel, Switzerland and Vancouver, Canada derived using the method presented in Chapter 2. Hemispherical sUHI magnitudes display significant seasonal and diurnal variation and are largest in summer months during the late afternoon during which solar heating of the surface is most intense, forcing the development of strong urban-rural contrasts in T_{surf}. Seasonality in late afternoon sUHI is largely dependent on accumulated radiative exposure over the day, which displays a strong positive relationship with sUHI magnitudes. In the winter months, a reduced overall solar input and increased cloud cover frequency suppresses daytime sUHI development resulting in less variability in sUHI, and lower overall sUHI magnitudes. Other meteorological controls have complex relationships with sUHI that often vary with time of day. Thus, sUHI development on any given day is the result of complex interplay between myriad meteorological controls.

Remote sensed sUHI is highly dependent on sensor-surface-sun geometry. This results in significant variation in the character of sUHI observed from sensors with different spatial, geometric, and temporal sampling regimes. Thus, traditional methods for thermal remote sensing of urban areas do not capture the true temporal and geometric nature of the urban effect on land T_{surf}. Urban effective anisotropy results in large geometric biases in remote sensing of urban areas as traditional satellite and aerial remote sensors sample only a fraction of the urban surface. These geometric biases manifest not only in deviation between observed sUHI magnitudes and the 'true' complete sUHI, but also impact characterizations of diurnal and seasonal patterns of sUHI and urban T_{surf}. Geometric biases in thermal remote sensing of urban areas are compounded by myriad temporal biases across a range of temporal scales, as traditional methods for urban thermal remote sensing are not time-continuous and only operable

under clear sky conditions. Both geometric and temporal biases affect the vast majority of sUHI study, most of which is performed using only a small number of satellite remote sensors, to which these biases are inherent.

This study provides the first, long-term, temporally continuous, geometrically representative analysis of sUHI. By sampling the urban surface in 3-dimensions and time-continuously, the method utilized in this chapter overcomes and quantifies spatial and temporal biases in the satellite thermal remote sensing record to better understand the geometric and temporal effects of a city on the surface climate. Further application of the method in other urban areas can help to facilitate a better understanding of the true nature of sUHI across myriad time scales and help to quantify the magnitude of geometric and temporal biases inherent in the satellite sUHI record.

References

Adderley, C., Christen, A., and Voogt, J. A. (2015). The effect of radiometer placement and view on inferred directional and hemispheric radiometric temperatures of an urban canopy. *Atmospheric Measurement Techniques*, 8(2):1891–1933.

Berk, A., Bernstein, L. S., and Robertson, D. C. (1987). MODTRAN: A Moderate Resolution Model for LOWTRAN7. Technical Report GL-TR-89-0122, United States Air Force.

Christen, A., Meier, F., and Scherer, D. (2012). High-frequency fluctuations of surface temperatures in an urban environment. *Theoretical and Applied Climatology*, 108(1-2):301–324.

Freitas, S. C., Trigo, I. F., Macedo, J., Barroso, C., Silva, R., and Perdigão, R. (2013). Land surface temperature from multiple geostationary satellites. *International Journal of Remote Sensing*, 34(9-10):3051–3068.

Grimmond, S. and Oke, T. R. (1999). Aerodynamic Properties of Urban Areas Derived from Analysis of Surface Form. *Journal of Applied Meteorology*, 38:1262–1292.

Hoch, S. (2005). *Radiative flux divergence in the surface boundary layer from observational and model perspectives*. PhD thesis, ETH Zurich.

Hoch, S., Calanca, P., Philipona, R., and Ohmura, A. (2007). Year-round observation of longwave radiative flux divergence in Greenland. *Journal of Applied Meteorology and Climatology*, 46(9):1469–1479.

Huang, F., Zhan, W., Voogt, J., Hu, L., Wang, Z., Quan, J., Ju, W., and Guo, Z. (2016). Temporal upscaling of surface urban heat island by incorporating an annual temperature cycle model: A tale of two cities. *Remote Sensing of Environment*, 186:1–12.

Lagouarde, J. P., Hénon, A., Irvine, M., Voogt, J., Pigeon, G., Moreau, P., Masson, V., and Mestayer, P. (2012). Experimental characterization and modelling of the nighttime directional anisotropy of thermal infrared measurements over an urban area: Case study of Toulouse (France). *Remote Sensing of Environment*, 117:19–33.

Oke, T. R. (1982). The energetic basis of the urban heat island. *Quarterly Journal of the Royal Meteorological Society*, 108:1–30.

Oke, T. R., Mills, G., Christen, A., and Voogt, J. A. (2017). *Urban Climates*. Cambridge University Press.

Peng, S., Piao, S., Ciais, P., Friedlingstein, P., Ottle, C., Bréon, F. M., Nan, H., Zhou, L., and Myneni, R. B. (2012). Surface urban heat island across 419 global big cities. *Environmental Science and Technology*, 46(2):696–703.

Roberts, S. (2010). *Three-dimensional radiation flux source areas in urban areas*. PhD thesis, University of British Columbia.

Rotach, M. W., Vogt, R., Bernhofer, C., Batchvarova, E., Christen, A., Clappier, A., Feddersen, B., Gryning, S.-E., Martucci, G., Mayer, H., Mitev, V., Oke, T. R., Parlow, E., Richner, H., Roth, M., Roulet, Y.-A., Ruffieux, D., Salmond, J. A., Schatzmann, M., and Voogt, J. A.

(2005). BUBBLE an Urban Boundary Layer Meteorology Project. *Theoretical and Applied Climatology*, 81(3-4):231–261.

Roth, M., Oke, T. R., and Emery, W. (1989). Satellite-derived urban heat islands from three coastal cities and the utilization of such data in urban climatology. *International Journal of Remote Sensing*, 10(11):1699–1720.

Runnalls, K. E. and Oke, T. R. (2000). Dynamics and controls of the near-surface heat island of Vancouver, British Columbia. *Physical Geography*, 21(4):283–304.

Soux, A., Voogt, J. A., and Oke, T. R. (2004). A model to calculate what a remote sensor 'sees' of an urban surface. *Boundary-Layer Meteorology*, 111(1):109–132.

Stewart, I. D. (2011). A systematic review and scientific critique of methodology in modern urban heat island literature. *International Journal of Climatology*, 31(2):200–217.

Stewart, I. D., Oke, T. R., and Krayenhoff, E. S. (2014). Evaluation of the local climate zone' scheme using temperature observations and model simulations. *International Journal of Climatology*, 34(4):1062–1080.

Voogt, J. A. (1995). *Thermal Remote Sensing of Urban Surface Temperatures*. PhD thesis, University of British Columbia.

Voogt, J. A. and Oke, T. R. (1998). Effects of urban surface geometry on remotely-sensed surface temperature. *International Journal of Remote Sensing*, 19(February 2015):895–920.

Voogt, J. A. and Oke, T. R. (2003). Thermal remote sensing of urban climates. *Remote Sensing of Environment*, 86(3):370–384.

Voogt, J. A., Oke, T. R., Bélair, S., Benjamin, M., Christen, A., Coops, N. C., Grimmond, C. S. B., Lemonsu, A., Mailhot, J., Masson, V., Mckendry, I., Strachan, I., and Wang, J. (2007).

The Environmental Prediction in Canadian Cities (EPiCC) Network. In *8th Symposium of the Urban Environment, American Meteorological Society*, Phoenix, AZ.

Weng, Q. and Fu, P. (2014). Modeling diurnal land temperature cycles over Los Angeles using downscaled GOES imagery. *ISPRS Journal of Photogrammetry and Remote Sensing*, 97:78–88.

Zakšek, K. and Oštir, K. (2012). Downscaling land surface temperature for urban heat island diurnal cycle analysis. *Remote Sensing of Environment*, 117:114–124.

Zhao, L., Lee, X., Smith, R. B., and Oleson, K. (2014). Strong contributions of local background climate to urban heat islands. *Nature*, 511(7508):216–219.

Chapter 4

Conclusion

This study presents the first long-term, time-continuous analysis of urban T_{surf} and sUHI that incorporates representative sampling of the three-dimensional urban surface. It is based on hemispheric upwelling longwave radiation measurements that are commonly made as a part of urban energy balance assessment and constitute a hitherto untapped resource for urban T_{surf} and sUHI analysis. The analysis contributes to a more complete understanding of the temporal and geometric nature of the urban effect on land T_{surf} and sUHI.

4.1 Summary of results

Chapter 2 details a hemispherical atmospheric correction method that uses version 4.1 of the MODTRAN radiative transfer code (Berk et al., 1987) in conjunction with the Surface-Sensor-Sun Urban Model (Soux et al., 2004) to derive hemispherical radiometric surface temperatures from longwave radiation upwelling from the urban surface measured from a downward facing pyrgeometer. The correction method is necessary for two reasons:

1. To retrieve T_{surf} that is representative of the temperature at which the surface is radiating (known as radiometric T_{surf}) by removing effects from absorption and emission by the atmosphere in between the surface and the sensor.

2. To facilitate intersite analysis of T_{surf}, where different ambient conditions, surface-sensor-sun geometries, and instrument types can have differential effects remote sensed TIR radiation.

The correction method was developed to be readily adaptable to other sensor types and study sites by accounting for complex three-dimensional surface geometry and non uniform spectral sensor response.

Analysis of an eight months of corrected $T_{hem, r}$ shows that atmospheric effects on inferred T_{hem} are large relative to typical sUHI magnitudes and show significant diurnal and seasonal variation. Relationships between correction magnitude and meteorological variables are complex. Correction magnitudes show strong positive relationships with $\Delta T_{surf\text{-}air}$ and incoming solar radiation. Conversely, although water vapor is the main absorber of broadband TIR radiation, it does not exert significant influence on correction magnitudes, as atmospheric transmittance shows little variation at typical humidities. To facilitate application of the method, a parameterization was developed incorporating a small number of generalizable radiative transfer simulations (included in Appendix A) and information about site geometry to retrieve radiometric hemispherical T_{surf} en masse using measurements of upwelling longwave, humidity, and T_{air}.

In addition, Chapter 2 explores the effect of surface geometry on remote sensed urban T_{surf} for three representations of the urban surface (complete, plan, and hemispherical). Analysis shows significant overestimation of T_{comp} by T_{plan} during the day and underestimation at night, particularly under clear sky conditions. By day, T_{hem} overestimates T_{comp}, but to a

lesser degree than T_{plan}. Daytime overestimation of T_{comp} by T_{hem} is more consistent under a wide variety of synoptic conditions, whereas overestimation by T_{plan} fluctuates significantly, resulting in poor performance under clear-sky ”satellite friendly” conditions. As measurements from narrow-FOV sensors in the nadir make up the bulk of the satellite urban T_{surf} record, our understanding of urban T_{surf} likely includes a significant warm bias. These biases are reflected in analysis of the effect of sensor-surface geometry on sUHI in Chapter 3.

Chapter 3 includes an analysis of two long term, time-continuous climatologies of hemispherical sUHI, one in Basel, Switzerland and another in Vancouver, Canada. sUHI for both study sites shows significant diurnal, day-to-day, and seasonal variability. sUHI is highly dependent on meteorological conditions, particularly accumulated solar radiation over a day and wind velocity. However, as sUHI is the result of differences in heating and cooling rates between the city and its non urban surroundings, its relationship to meteorological controls is complex. Analysis of sUHI development under a range of mid-latitude synoptic conditions lead to the development of the first observationally-supported, generalizable model for sUHI development presented in Section 3.4.1.

Analysis of the effect of sensor-surface geometry on sUHI is also included in Chapter 3. Results are similar to those found in Chapter 2, with significant daytime overestimation of $sUHI_{comp}$ by $sUHI_{plan}$, particularly during hot clear sky conditions. Directional biases in remote sensed assessment of sUHI change observed magnitudes and the diurnal character of sUHI by modifying patterns of observed sUHI in the hours near sunset. Thus, satellite based assessments of the diurnal pattern of sUHI may lead to misrepresentations of its ’true’ diurnal character.

4.2 Limitations and future work

The complex nature of the urban surface introduces myriad shortcomings and biases into conventional remote sensing of urban thermal climates - this method is no exception. Sensor placement sensitivity tests in Section 2.19 corroborate findings in Roberts (2010) and Adderley et al. (2015). They indicate that longwave radiation upwelling from the urban surface as measured from a downward-facing radiometer is spatially variant when measured from heights below approximately three to five times mean building height. Most pyrgeometers (including those used in this study) are mounted below this height and are subject to a bias towards facets that make up a disproportionately large fraction of the sensor FOV. For sensors mounted at less than optimal heights, the effect of this bias on derived $T_{hem,\,r}$ is largely dependent on sensor placement relative to rooftop facets, with better performance when mounted offset from roof areas. Pyrgeometers at the Sperrstrasse and Sunset tower sites are placed far enough from rooftops to render this bias relatively small. However, future studies should strive for pyrgeometer heights that are more optimal not only to yield more geometrically representative $T_{hem,\,r}$, but also to ensure irradiances are representative of the complete urban longwave emission in energy balance assessments.

As the method developed in this study uses upwelling longwave measurements from fixed tower sites, it is not practical for large scale spatially-continuous and spatially extensive analysis of sUHI. This limits the method to mid- and low-rise neighborhoods. However, by combining concepts from other work, the method can be adapted to retrieve spatiotemporally continuous urban $T_{hem,\,r}$ from mobile measurements of upwelling longwave irradiances. Sugawara and Takamura (2006) used helicopter-mounted pyrgeometers and narrow-FOV infrared thermometers in aerial traverses to successfully quantify effects from urban effective anisotropy on upwelling longwave radiation, but did not incorporate a robust atmospheric

correction routine to account for spatially variant surface geometry to remove atmospheric effects or retrieve $T_{hem,\,r}$. Determining the distance to the surface for a moving hemispherical sensor viewing a complex, three-dimensional surface is difficult. Ray-tracing methods similar to those used in Ceamanos et al. (2016) could provide a solution, but must be modified to return path lengths in addition to seen and unseen points for a mobile aerial sensor. In addition, sensitivity to ambient conditions (particularly the T_{air} profile) will make accurate atmospheric correction computationally expensive in mobile applications of the method. Notwithstanding evaluations of method performance in such applications. If these problems are solved, application of the method in aerial traverses may be useful in quantifying the spatiotemporal character of urban effective anisotropy on remote sensed urban T_{surf} as hemispherical instrumentation can be run simultaneously with near-ground and satellite based narrow-FOV sensors. Such analysis could be used to develop parameterizations to modify satellite retrieved urban T_{surf} to better represent the complete urban T_{surf}.

While satellite assessment of sUHI and urban T_{surf} has been essential in elucidating the spatial character of urban effects on T_{surf}, several of the questions posed nearly 30 years ago in Roth et al. (1989) remain unanswered. This should prompt not only critical assessment of the urban T_{surf} record, but also the development and use of novel methods to fill knowledge gaps, quantify biases, and uncover methodological shortcomings. This method, and in particular its parameterization, is intended to aid in such an endeavor as it is readily adapted to other study sites and requires few meteorological inputs. According to the Urban Flux Network (Urbanflux) currently there are 26 operational flux towers in urban areas instrumented for assessment of the net radiation budget. In addition, many other datasets of urban energy balances from inactive and decommissioned towers and from campaigns not indexed by Urbanflux are available for analysis via this method. These datasets span several continents and climatic zones, and characterize energy balances for cities over a range of developing and developed nations, with

many operational over very long (5+ year) time scales. Thus, the application of this method over existing untapped datasets, and as a component of future energy balance assessments, can not only could provide a wealth of novel urban T_{surf} and sUHI analyses for urban climatology and could also can provide for analysis outside the traditional purview of urban climatology. The character of the urban effect on land T_{surf} (and climate at large) has complex, multifaceted relationships with the layout, size, population density, and development regimes of a given city as well as factors that are more difficult to observe, including social structure and culture. Long term, time continuous analysis of urban T_{surf} and sUHI can help to better understand these links.

4.3 Final remarks

Broadly, the method, its parameterization, and the analysis presented in this study were conducted to provide for novel analyses of the urban effect on T_{surf} and to prompt further critical assessment of the urban T_{surf} and sUHI record. In addition, this method was developed in order to contribute to addressing methodological and conceptual questions outlined in Roth et al. (1989) by filling knowledge gaps in the urban T_{surf} and sUHI record. These analyses help to understand the temporal and geometric character of urban T_{surf} and to facilitate more effective and representative study of the urban effect on T_{surf}. Indeed, if similar conceptual flaws and shortcomings to those found for the aUHI in Stewart (2011) are likely in sUHI analysis, quantification of instrument and methodological biases and shortcomings in remote sensing of urban T_{surf} and the introduction of new methods to overcome these shortcomings may bring us closer to uncovering the true geometric, temporal, and spatial effects of cities on land surface temperature and on the climate at large.

References

Adderley, C., Christen, A., and Voogt, J. A. (2015). The effect of radiometer placement and view on inferred directional and hemispheric radiometric temperatures of an urban canopy. *Atmospheric Measurement Techniques*, 8(2):1891–1933.

Berk, A., Bernstein, L. S., and Robertson, D. C. (1987). MODTRAN: A Moderate Resolution Model for LOWTRAN7. Technical Report GL-TR-89-0122, United States Air Force.

Ceamanos, X., Briottet, X., Roussel, G., Gilardy, H., and Adeline, K. (2016). Using 3D information for atmospheric correction of airborne hyperspectral images of urban areas. In *Remote Sensing Technologies and Applications in Urban Environments*, volume 10008, pages 1–4.

Roberts, S. (2010). *Three-dimensional radiation flux source areas in urban areas*. PhD thesis, University of British Columbia.

Roth, M., Oke, T. R., and Emery, W. (1989). Satellite-derived urban heat islands from three coastal cities and the utilization of such data in urban climatology. *International Journal of Remote Sensing*, 10(11):1699–1720.

Soux, A., Voogt, J. A., and Oke, T. R. (2004). A model to calculate what a remote sensor 'sees' of an urban surface. *Boundary-Layer Meteorology*, 111(1):109–132.

Stewart, I. D. (2011). A systematic review and scientific critique of methodology in modern urban heat island literature. *International Journal of Climatology*, 31(2):200–217.

Sugawara, H. and Takamura, T. (2006). Longwave radiation flux from an urban canopy: Evaluation via measurements of directional radiometric temperature. *Remote Sensing of Environment*, 104(2):226–237.

Appendix A

Transmittances for a range of water vapor mass densities and path lengths.

Table A.1: A look-up table of bulk, point to point atmospheric transmittances as a function of path length (m) and water vapor mass density ($\mathrm{g\,m^{-3}}$). Assembled from simulations in MODTRAN 4.1 with $T_{air} = T_{surf} = 300\ \mathrm{K}$, $CO_2 = 400\ \mathrm{ppm}$, and trace absorber and O_3 concentrations supplied by the mid-latitude summer standard atmospheric profile (Kantor and Cole, 1962)

Water vapor $\mathrm{g\,m^{-3}}$	1 m	2 m	3 m	4 m	5 m	6 m	7 m	8 m	9 m	10 m
0.1	98.78	97.915	97.196	96.568	96.007	95.497	95.029	94.595	94.189	93.809
0.5	97.497	95.987	94.791	93.778	92.891	92.099	91.379	90.72	90.11	89.542
1	96.449	94.502	93.005	91.762	90.688	89.738	88.883	88.105	87.389	86.726
1.5	95.639	93.39	91.695	90.304	89.113	88.066	87.129	86.28	85.503	84.785
2	94.962	92.48	90.637	89.137	87.861	86.745	85.751	84.854	84.034	83.28
2.5	94.372	91.701	89.74	88.155	86.813	85.645	84.607	83.674	82.824	82.043
3	93.846	91.016	88.956	87.301	85.906	84.696	83.625	82.663	81.789	80.988
3.5	93.369	90.401	88.257	86.543	85.104	83.86	82.762	81.777	80.884	80.066
4	92.932	89.841	87.624	85.86	84.384	83.111	81.99	80.986	80.077	79.246
4.5	92.526	89.326	87.045	85.237	83.729	82.432	81.291	80.271	79.348	78.505
5	92.147	88.848	86.509	84.663	83.128	81.809	80.65	79.616	78.682	77.828
5.5	91.791	88.402	86.012	84.131	82.571	81.233	80.059	79.013	78.067	77.205
6	91.455	87.983	85.546	83.635	82.052	80.697	79.51	78.452	77.497	76.626
6.5	91.136	87.588	85.108	83.169	81.566	80.195	78.995	77.927	76.964	76.086
7	90.832	87.213	84.694	82.729	81.108	79.723	78.511	77.434	76.463	75.579
7.5	90.542	86.856	84.301	82.313	80.674	79.276	78.054	76.968	75.99	75.1
8	90.264	86.516	83.927	81.917	80.263	78.852	77.621	76.527	75.542	74.646
8.5	89.997	86.191	83.57	81.539	79.87	78.449	77.208	76.107	75.116	74.215
9	89.74	85.879	83.229	81.179	79.496	78.064	76.815	75.706	74.709	73.803
9.5	89.492	85.578	82.901	80.833	79.137	77.695	76.438	75.323	74.32	73.409
10	89.253	85.29	82.586	80.5	78.792	77.34	76.076	74.955	73.947	73.032
10.5	89.021	85.011	82.282	80.181	78.46	76.999	75.728	74.601	73.588	72.669
11	88.796	84.741	81.989	79.872	78.14	76.671	75.392	74.26	73.242	72.319
11.5	88.578	84.48	81.705	79.573	77.831	76.354	75.068	73.93	72.909	71.981
12	88.366	84.227	81.43	79.285	77.532	76.047	74.755	73.612	72.586	71.655
12.5	88.16	83.981	81.164	79.005	77.242	75.749	74.451	73.303	72.273	71.338
13	87.959	83.743	80.905	78.733	76.961	75.461	74.157	73.004	71.969	71.031
13.5	87.763	83.51	80.654	78.469	76.687	75.18	73.871	72.713	71.675	70.733
14	87.572	83.284	80.409	78.212	76.421	74.907	73.592	72.43	71.388	70.442
14.5	87.385	83.063	80.171	77.961	76.162	74.641	73.321	72.154	71.108	70.159
15	87.202	82.848	79.938	77.717	75.91	74.382	73.057	71.886	70.835	69.883
15.5	87.024	82.638	79.71	77.478	75.663	74.129	72.799	71.623	70.569	69.614
16	86.849	82.432	79.488	77.245	75.422	73.882	72.547	71.367	70.309	69.35
16.5	86.678	82.231	79.271	77.018	75.187	73.64	72.3	71.116	70.055	69.092
17	86.51	82.034	79.058	76.795	74.956	73.404	72.059	70.87	69.805	68.84
17.5	86.345	81.84	78.85	76.576	74.73	73.172	71.822	70.63	69.561	68.592
18	86.183	81.651	78.646	76.362	74.509	72.945	71.59	70.394	69.321	68.349
18.5	86.024	81.465	78.446	76.152	74.292	72.722	71.363	70.162	69.086	68.111
19	85.868	81.283	78.249	75.946	74.079	72.504	71.139	69.934	68.855	67.876
19.5	85.715	81.104	78.056	75.744	73.869	72.289	70.92	69.711	68.628	67.646
20	85.564	80.928	77.867	75.545	73.664	72.078	70.704	69.491	68.404	67.419
20.5	85.416	80.755	77.68	75.35	73.461	71.87	70.492	69.275	68.184	67.195
21	85.27	80.585	77.497	75.157	73.263	71.666	70.283	69.062	67.968	66.975
21.5	85.126	80.417	77.316	74.968	73.067	71.465	70.077	68.852	67.754	66.758
22	84.984	80.252	77.139	74.782	72.874	71.266	69.874	68.645	67.544	66.544
22.5	84.844	80.09	76.963	74.598	72.684	71.071	69.675	68.441	67.336	66.333
23	84.707	79.929	76.791	74.417	72.497	70.879	69.477	68.24	67.131	66.124
23.5	84.57	79.771	76.621	74.239	72.312	70.688	69.283	68.042	66.928	65.918

Table A.2: Continued from Table A.1

Water vapor $g\,m^{-3}$	11 m	12 m	13 m	14 m	15 m	16 m	17 m	18 m	19 m	20 m
0.1	93.45	93.11	92.786	92.478	92.183	91.9	91.628	91.367	91.114	90.871
0.5	89.009	88.508	88.035	87.586	87.158	86.75	86.36	85.987	85.627	85.282
1	86.108	85.529	84.984	84.469	83.98	83.516	83.073	82.65	82.244	81.855
1.5	84.119	83.496	82.911	82.36	81.839	81.345	80.875	80.426	79.997	79.587
2	82.582	81.93	81.32	80.746	80.204	79.691	79.203	78.739	78.295	77.871
2.5	81.321	80.649	80.021	79.431	78.874	78.347	77.847	77.371	76.917	76.483
3	80.248	79.561	78.919	78.316	77.748	77.211	76.701	76.217	75.755	75.314
3.5	79.312	78.612	77.958	77.345	76.768	76.223	75.706	75.215	74.747	74.3
4	78.479	77.769	77.106	76.485	75.9	75.348	74.825	74.329	73.856	73.404
4.5	77.728	77.009	76.338	75.71	75.119	74.561	74.033	73.532	73.055	72.6
5	77.043	76.316	75.638	75.004	74.408	73.845	73.313	72.808	72.327	71.869
5.5	76.412	75.678	74.994	74.355	73.754	73.187	72.651	72.143	71.659	71.198
6	75.827	75.086	74.398	73.753	73.148	72.578	72.039	71.527	71.041	70.577
6.5	75.28	74.534	73.841	73.192	72.584	72.01	71.468	70.954	70.465	69.999
7	74.767	74.016	73.318	72.666	72.054	71.478	70.933	70.416	69.925	69.457
7.5	74.283	73.528	72.826	72.17	71.555	70.976	70.428	69.909	69.416	68.946
8	73.824	73.065	72.359	71.7	71.083	70.501	69.951	69.43	68.934	68.462
8.5	73.388	72.625	71.916	71.254	70.634	70.049	69.497	68.974	68.477	68.003
9	72.973	72.206	71.494	70.829	70.205	69.619	69.064	68.539	68.04	67.564
9.5	72.575	71.805	71.089	70.422	69.796	69.207	68.65	68.123	67.622	67.145
10	72.193	71.42	70.702	70.031	69.403	68.812	68.253	67.724	67.221	66.742
10.5	71.827	71.05	70.329	69.656	69.025	68.432	67.871	67.34	66.835	66.355
11	71.474	70.694	69.97	69.294	68.661	68.066	67.503	66.97	66.463	65.981
11.5	71.133	70.349	69.623	68.945	68.31	67.712	67.147	66.612	66.103	65.619
12	70.803	70.017	69.287	68.607	67.969	67.369	66.802	66.265	65.755	65.269
12.5	70.483	69.694	68.962	68.279	67.639	67.037	66.468	65.929	65.416	64.928
13	70.172	69.381	68.646	67.961	67.319	66.714	66.143	65.602	65.088	64.598
13.5	69.871	69.076	68.339	67.651	67.007	66.4	65.827	65.284	64.767	64.275
14	69.577	68.78	68.04	67.35	66.703	66.094	65.518	64.973	64.455	63.961
14.5	69.291	68.491	67.749	67.056	66.406	65.795	65.218	64.67	64.15	63.654
15	69.012	68.209	67.464	66.769	66.117	65.503	64.924	64.374	63.852	63.354
15.5	68.74	67.934	67.186	66.488	65.834	65.218	64.636	64.084	63.56	63.06
16	68.473	67.664	66.914	66.213	65.557	64.939	64.354	63.8	63.274	62.772
16.5	68.212	67.4	66.647	65.944	65.285	64.665	64.078	63.522	62.993	62.489
17	67.956	67.142	66.386	65.68	65.019	64.396	63.807	63.249	62.718	62.212
17.5	67.706	66.888	66.129	65.421	64.757	64.132	63.541	62.98	62.447	61.939
18	67.459	66.639	65.878	65.167	64.5	63.872	63.279	62.716	62.181	61.671
18.5	67.218	66.394	65.63	64.917	64.247	63.617	63.021	62.456	61.919	61.406
19	66.98	66.154	65.387	64.671	63.999	63.366	62.768	62.2	61.661	61.146
19.5	66.746	65.917	65.147	64.428	63.754	63.119	62.518	61.948	61.407	60.89
20	66.516	65.684	64.911	64.19	63.513	62.875	62.272	61.7	61.156	60.637
20.5	66.29	65.454	64.679	63.954	63.275	62.635	62.029	61.455	60.908	60.387
21	66.066	65.228	64.45	63.722	63.04	62.397	61.789	61.213	60.664	60.141
21.5	65.846	65.005	64.223	63.493	62.808	62.163	61.553	60.974	60.423	59.898
22	65.629	64.785	64	63.267	62.58	61.932	61.319	60.737	60.184	59.657
22.5	65.414	64.567	63.779	63.044	62.354	61.703	61.088	60.504	59.949	59.419
23	65.203	64.352	63.562	62.823	62.13	61.477	60.859	60.273	59.716	59.184
23.5	64.993	64.14	63.346	62.605	61.909	61.253	60.633	60.045	59.485	58.951

Table A.3: Continued from Table A.2

Water vapor $g\,m^{-3}$	21 m	22 m	23 m	24 m	25 m	26 m	27 m	28 m	29 m	30 m
0.1	90.635	90.406	90.185	89.97	89.76	89.557	89.359	89.166	88.978	88.794
0.5	84.949	84.627	84.317	84.016	83.725	83.442	83.168	82.902	82.643	82.39
1	81.481	81.122	80.775	80.44	80.116	79.803	79.499	79.205	78.919	78.641
1.5	79.192	78.813	78.449	78.097	77.757	77.429	77.111	76.804	76.505	76.216
2	77.464	77.073	76.697	76.335	75.986	75.648	75.322	75.006	74.7	74.403
2.5	76.067	75.668	75.284	74.915	74.559	74.215	73.883	73.561	73.25	72.948
3	74.891	74.486	74.096	73.721	73.36	73.012	72.676	72.35	72.035	71.73
3.5	73.872	73.462	73.068	72.69	72.325	71.973	71.633	71.305	70.987	70.679
4	72.972	72.558	72.161	71.779	71.411	71.056	70.714	70.383	70.063	69.753
4.5	72.164	71.747	71.347	70.962	70.592	70.235	69.891	69.558	69.236	68.925
5	71.43	71.011	70.608	70.221	69.849	69.49	69.144	68.81	68.486	68.173
5.5	70.757	70.335	69.93	69.541	69.167	68.807	68.459	68.123	67.799	67.484
6	70.134	69.71	69.303	68.913	68.537	68.175	67.826	67.489	67.162	66.847
6.5	69.554	69.128	68.719	68.327	67.95	67.586	67.236	66.897	66.57	66.253
7	69.01	68.582	68.172	67.778	67.399	67.034	66.683	66.343	66.014	65.696
7.5	68.497	68.068	67.656	67.261	66.881	66.514	66.161	65.82	65.49	65.171
8	68.012	67.581	67.168	66.771	66.389	66.021	65.667	65.324	64.994	64.673
8.5	67.551	67.118	66.703	66.305	65.922	65.553	65.197	64.853	64.521	64.199
9	67.111	66.676	66.26	65.86	65.476	65.105	64.748	64.403	64.069	63.746
9.5	66.689	66.253	65.835	65.434	65.048	64.676	64.318	63.971	63.636	63.312
10	66.285	65.847	65.428	65.025	64.637	64.264	63.904	63.556	63.22	62.895
10.5	65.895	65.456	65.035	64.631	64.242	63.867	63.506	63.156	62.819	62.492
11	65.52	65.079	64.656	64.25	63.86	63.483	63.12	62.77	62.431	62.102
11.5	65.156	64.714	64.289	63.882	63.49	63.112	62.747	62.395	62.055	61.725
12	64.804	64.36	63.934	63.524	63.131	62.751	62.385	62.032	61.69	61.358
12.5	64.462	64.016	63.588	63.177	62.782	62.401	62.033	61.678	61.335	61.002
13	64.13	63.682	63.252	62.839	62.442	62.06	61.691	61.334	60.989	60.655
13.5	63.805	63.356	62.924	62.51	62.111	61.727	61.356	60.998	60.651	60.316
14	63.489	63.038	62.605	62.189	61.788	61.402	61.03	60.67	60.322	59.985
14.5	63.18	62.727	62.292	61.874	61.472	61.084	60.71	60.349	59.999	59.661
15	62.878	62.423	61.986	61.566	61.163	60.773	60.398	60.035	59.683	59.343
15.5	62.582	62.125	61.687	61.265	60.859	60.468	60.091	59.726	59.374	59.032
16	62.292	61.833	61.393	60.969	60.562	60.169	59.79	59.424	59.07	58.726
16.5	62.008	61.546	61.104	60.679	60.27	59.875	59.495	59.127	58.771	58.426
17	61.728	61.265	60.821	60.394	59.983	59.587	59.204	58.835	58.477	58.131
17.5	61.453	60.988	60.542	60.113	59.7	59.303	58.919	58.547	58.188	57.841
18	61.183	60.716	60.268	59.837	59.423	59.023	58.637	58.265	57.904	57.555
18.5	60.917	60.448	59.998	59.565	59.149	58.748	58.36	57.986	57.624	57.273
19	60.654	60.183	59.732	59.297	58.879	58.476	58.087	57.711	57.347	56.995
19.5	60.396	59.923	59.469	59.033	58.613	58.208	57.818	57.44	57.075	56.721
20	60.141	59.666	59.21	58.772	58.35	57.944	57.552	57.172	56.805	56.45
20.5	59.889	59.412	58.955	58.515	58.091	57.683	57.289	56.908	56.54	56.183
21	59.641	59.162	58.702	58.26	57.835	57.425	57.03	56.647	56.277	55.919
21.5	59.395	58.914	58.453	58.009	57.582	57.17	56.773	56.389	56.018	55.658
22	59.153	58.67	58.206	57.761	57.332	56.919	56.52	56.134	55.761	55.4
22.5	58.913	58.428	57.962	57.515	57.085	56.669	56.269	55.882	55.508	55.145
23	58.675	58.188	57.721	57.272	56.84	56.423	56.021	55.632	55.256	54.892
23.5	58.44	57.951	57.482	57.031	56.597	56.179	55.775	55.385	55.008	54.642

Table A.4: Continued from Table A.3

Water vapor $g\,m^{-3}$	31 m	32 m	33 m	34 m	35 m	36 m	37 m	38 m	39 m	40 m
0.1	88.615	88.439	88.75	88.59	88.434	88.28	88.129	87.981	87.835	87.692
0.5	82.145	81.905	82.382	82.159	81.942	81.729	81.521	81.316	81.115	80.918
1	78.371	78.109	78.565	78.316	78.073	77.836	77.604	77.377	77.154	76.936
1.5	75.934	75.661	76.048	75.786	75.531	75.281	75.037	74.799	74.566	74.337
2	74.115	73.835	74.147	73.877	73.613	73.357	73.106	72.861	72.621	72.387
2.5	72.655	72.371	72.612	72.336	72.068	71.806	71.551	71.302	71.058	70.82
3	71.434	71.146	71.321	71.042	70.77	70.505	70.247	69.996	69.75	69.509
3.5	70.38	70.091	70.207	69.925	69.65	69.383	69.123	68.87	68.622	68.381
4	69.453	69.162	69.224	68.94	68.664	68.396	68.135	67.88	67.631	67.388
4.5	68.623	68.33	68.345	68.06	67.782	67.513	67.25	66.995	66.745	66.502
5	67.87	67.575	67.548	67.262	66.984	66.713	66.45	66.194	65.944	65.699
5.5	67.179	66.884	66.819	66.532	66.253	65.981	65.718	65.461	65.21	64.966
6	66.541	66.244	66.146	65.858	65.578	65.306	65.042	64.784	64.533	64.288
6.5	65.946	65.648	65.519	65.231	64.95	64.678	64.413	64.155	63.904	63.658
7	65.388	65.089	64.934	64.644	64.363	64.09	63.824	63.566	63.314	63.069
7.5	64.862	64.562	64.382	64.092	63.81	63.537	63.271	63.012	62.76	62.513
8	64.363	64.062	63.861	63.57	63.287	63.013	62.747	62.487	62.234	61.988
8.5	63.888	63.585	63.365	63.074	62.791	62.516	62.249	61.989	61.736	61.489
9	63.434	63.13	62.893	62.601	62.318	62.042	61.775	61.514	61.26	61.013
9.5	62.998	62.693	62.442	62.149	61.865	61.589	61.32	61.059	60.805	60.557
10	62.579	62.273	62.009	61.715	61.43	61.153	60.884	60.623	60.368	60.119
10.5	62.175	61.868	61.592	61.298	61.012	60.734	60.465	60.202	59.947	59.698
11	61.784	61.475	61.19	60.895	60.608	60.33	60.06	59.797	59.541	59.291
11.5	61.405	61.095	60.801	60.506	60.218	59.939	59.668	59.405	59.148	58.898
12	61.037	60.726	60.425	60.128	59.84	59.561	59.289	59.025	58.767	58.516
12.5	60.679	60.367	60.06	59.763	59.474	59.193	58.921	58.656	58.398	58.146
13	60.331	60.017	59.705	59.407	59.117	58.836	58.563	58.297	58.038	57.786
13.5	59.99	59.675	59.359	59.06	58.77	58.488	58.214	57.948	57.688	57.435
14	59.658	59.341	59.022	58.723	58.431	58.148	57.874	57.607	57.347	57.093
14.5	59.332	59.014	58.693	58.393	58.101	57.817	57.542	57.274	57.013	56.759
15	59.013	58.693	58.372	58.071	57.778	57.493	57.217	56.948	56.687	56.432
15.5	58.701	58.379	58.058	57.755	57.461	57.176	56.899	56.63	56.368	56.112
16	58.394	58.071	57.75	57.446	57.152	56.866	56.588	56.318	56.055	55.799
16.5	58.092	57.768	57.447	57.143	56.848	56.561	56.283	56.012	55.749	55.492
17	57.795	57.47	57.151	56.846	56.55	56.262	55.983	55.712	55.448	55.19
17.5	57.503	57.176	56.86	56.554	56.257	55.969	55.689	55.417	55.152	54.894
18	57.216	56.887	56.574	56.268	55.97	55.681	55.4	55.127	54.862	54.603
18.5	56.933	56.603	56.293	55.985	55.687	55.397	55.116	54.842	54.576	54.316
19	56.653	56.322	56.016	55.708	55.409	55.118	54.836	54.561	54.294	54.034
19.5	56.378	56.045	55.744	55.435	55.134	54.843	54.56	54.285	54.017	53.757
20	56.106	55.772	55.476	55.165	54.864	54.572	54.288	54.013	53.744	53.483
20.5	55.837	55.502	55.211	54.9	54.598	54.305	54.021	53.744	53.475	53.214
21	55.572	55.235	54.95	54.638	54.335	54.042	53.756	53.479	53.21	52.948
21.5	55.309	54.971	54.693	54.38	54.076	53.782	53.496	53.218	52.948	52.685
22	55.05	54.71	54.438	54.125	53.821	53.525	53.239	52.96	52.689	52.426
22.5	54.793	54.453	54.188	53.873	53.568	53.272	52.985	52.706	52.434	52.17
23	54.54	54.197	53.94	53.624	53.318	53.022	52.734	52.454	52.182	51.917
23.5	54.288	53.945	53.694	53.379	53.072	52.774	52.486	52.205	51.933	51.667

Table A.5: Continued from Table A.4

Water vapor $g\,m^{-3}$	41 m	42 m	43 m	44 m	45 m	46 m	47 m	48 m
0.1	87.55	87.411	87.273	87.137	87.004	86.872	86.742	86.613
0.5	80.724	80.534	80.346	80.162	79.981	79.802	79.626	79.453
1	76.722	76.512	76.305	76.103	75.904	75.708	75.516	75.327
1.5	74.113	73.894	73.678	73.467	73.26	73.057	72.857	72.66
2	72.157	71.933	71.712	71.497	71.285	71.078	70.874	70.674
2.5	70.587	70.36	70.137	69.918	69.704	69.494	69.289	69.087
3	69.274	69.045	68.82	68.6	68.385	68.174	67.967	67.764
3.5	68.144	67.914	67.688	67.467	67.251	67.039	66.831	66.628
4	67.151	66.92	66.693	66.472	66.255	66.043	65.835	65.631
4.5	66.264	66.032	65.805	65.583	65.366	65.154	64.946	64.742
5	65.461	65.229	65.002	64.78	64.562	64.35	64.141	63.938
5.5	64.727	64.494	64.267	64.044	63.827	63.614	63.406	63.202
6	64.049	63.816	63.589	63.366	63.148	62.935	62.727	62.523
6.5	63.419	63.186	62.958	62.735	62.517	62.304	62.095	61.891
7	62.829	62.595	62.367	62.144	61.926	61.712	61.503	61.299
7.5	62.273	62.039	61.811	61.587	61.369	61.155	60.946	60.741
8	61.748	61.513	61.284	61.06	60.842	60.628	60.418	60.213
8.5	61.248	61.013	60.784	60.56	60.34	60.126	59.916	59.711
9	60.771	60.536	60.306	60.082	59.862	59.647	59.437	59.232
9.5	60.315	60.079	59.849	59.624	59.404	59.189	58.979	58.773
10	59.877	59.641	59.41	59.184	58.964	58.749	58.538	58.331
10.5	59.455	59.218	58.987	58.761	58.54	58.324	58.113	57.906
11	59.048	58.811	58.579	58.352	58.131	57.915	57.703	57.496
11.5	58.654	58.416	58.184	57.957	57.735	57.518	57.306	57.099
12	58.272	58.033	57.8	57.573	57.351	57.134	56.921	56.713
12.5	57.901	57.662	57.429	57.2	56.978	56.76	56.547	56.339
13	57.54	57.301	57.067	56.838	56.615	56.397	56.183	55.975
13.5	57.189	56.949	56.714	56.485	56.262	56.043	55.829	55.62
14	56.846	56.605	56.371	56.141	55.917	55.697	55.483	55.273
14.5	56.511	56.27	56.034	55.804	55.58	55.36	55.145	54.935
15	56.184	55.942	55.706	55.475	55.25	55.03	54.815	54.604
15.5	55.864	55.621	55.384	55.153	54.927	54.707	54.491	54.28
16	55.55	55.306	55.069	54.837	54.611	54.39	54.174	53.962
16.5	55.242	54.998	54.76	54.528	54.301	54.08	53.863	53.651
17	54.94	54.695	54.457	54.224	53.997	53.775	53.558	53.345
17.5	54.643	54.398	54.159	53.925	53.698	53.475	53.258	53.045
18	54.351	54.105	53.866	53.632	53.404	53.181	52.962	52.749
18.5	54.064	53.818	53.578	53.343	53.114	52.891	52.672	52.459
19	53.781	53.535	53.294	53.059	52.83	52.606	52.387	52.173
19.5	53.503	53.256	53.015	52.779	52.55	52.325	52.106	51.891
20	53.229	52.981	52.739	52.503	52.273	52.048	51.829	51.614
20.5	52.959	52.71	52.468	52.232	52.001	51.776	51.555	51.34
21	52.692	52.443	52.2	51.963	51.732	51.506	51.286	51.07
21.5	52.429	52.179	51.936	51.699	51.467	51.241	51.02	50.804
22	52.169	51.919	51.675	51.438	51.205	50.979	50.757	50.541
22.5	51.913	51.662	51.418	51.18	50.947	50.72	50.498	50.281
23	51.659	51.408	51.163	50.925	50.692	50.464	50.242	50.024
23.5	51.409	51.158	50.912	50.673	50.439	50.211	49.988	49.771

Michael Allen

Education

University of Western Ontario
MSc, Geography, 2017

University of Portland
BA, Environmental Studies, 2015

Honors and awards

2017
Excellent Student Oral Presentation Award
Board on the Urban Environment, American Meteorological Society
Student Travel Award
Joint Urban Remote Sensing Event, IEEE
E.G. Pleva Award for Teaching Excellence
Department of Geography, University of Western Ontario

2016
Dr. Edmond M. Dewan Young Scientist Scholarship
Atmospheric Science & Space Physics Sections, American Geophysical Union
E.G. Pleva Award for Teaching Excellence
Department of Geography, University of Western Ontario
Student Travel Award, Annual Meeting
American Meteorological Society

2015
1st Place, Peer Judging Panel
Undergraduate Virtual Poster Session, American Geophysical Union Fall Meeting
2nd Place, Expert Judging Panel
Undergraduate Virtual Poster Session, American Geophysical Union Fall Meeting

Relevant work experience

Department of Geography,
University of Western Ontario
Research Assistant, Summer 2015, 16, 17
Teaching Assistant, Physical Geography, Winter 2016, 17
Teaching Assistant, Weather and Climate, Fall 2015, 16

Department of Environmental Studies
University of Portland
Research Assistant, Spring 2014 - Spring 2015

Vigor Industrial, LLC
Environmental Intern, Winter 2014 - Spring 2015

Peer reviewed conference proceedings

2017
Allen, Michael A., J. Voogt, A. Christen. "Towards a Continuous Climatological Assessment of Urban Surface Heat Islands", *Proceedings of the Joint Urban Remote Sensing Event*, (2017): 1-4.

2015
Allen, Michael A., and T. Eckmann. "Quantifying Seasonal Variations in the Atmospheric Boundary Layer in Portland, Oregon to Characterize Local Air Pollution Events", *Proceedings of the National Conference on Undergraduate Research*, Vol. 5. (2015): 430-438.

Conference abstracts

2017
Allen, Michael A., J. Voogt, A. Christen. "Towards a Continuous Climatological Assessment of Urban Surface Heat Islands." Joint Urban Remote Sensing Event: Dubai, UAE, *oral*.
Allen, Michael A., J. Voogt, A. Christen. "A Climatology of Urban Surface Heat Islands Derived from Hemispherical Radiometric Surface Temperatures." American Meteorological Society Annual Meeting: Seattle, WA, *oral*.

2016
Allen, Michael A., J. Voogt, A. Christen. "A Method to Assess Urban Surface Heat Islands using Hemispherical Radiometric Temperatures." American Geophysical Union Fall Meeting: San Francisco, CA, *oral*.

2015

Allen, Michael A., and T. Eckmann. "Quantifying Seasonal Variations in the Atmospheric Boundary Layer in Portland, Oregon to Characterize Local Air Pollution Events", National Conference on Undergraduate Research: Cheney, WA, *oral*.

Holmes, Brooke A., **M. Allen**, and T. Eckmann. "Comparing Growth Rates of Succulent Species and Water Retention of Novel Substrates to Optimize Urban Green Roof Efficiencies in the Pacific Northwest", National Conference on Undergraduate Research: Cheney, WA, *oral*.

Wright, Samantha G, **M. Allen**, and T. Eckmann. "Spatial Interpolation with GIS to Map Industrial Air Pollution in North Portland", Proceedings of the Oregon Academy of Science Annual Meeting: Portland, OR, *poster*.

2014

Holmes, Brooke A., **M. Allen**, and T. Eckmann. (2014, December) "Quantifying Performance of Succulents and Novel Substrates for Extensive Green Roof Applications in the US Pacific Northwest", American Geophysical Union Fall Meeting: San Francisco, CA, *poster*.

Allen, Michael A., B. Holmes, and T. Eckmann. (2014, December) "Measuring Urban Microclimates and Vertical Temperature Profiles in Portland, Oregon for Analyzing Energy Budgets and Air Pollution Sources", American Geophysical Union Fall Meeting: San Francisco, CA, *poster*.